NANOTECHNOLOGY SCIENCE AND TECHNOLOGY

NANOSTRUCTURES AND FILMS BASED ON CLASSICAL WIDE GAP SEMICONDUCTORS FOR PHOTOVOLTAIC APPLICATIONS

No part of this digital document may be reproduced, stored in a retrieval system or transmitted commercially in any form or by any means. The publisher has taken reasonable care in the preparation of this digital document, but makes no expressed or implied warranty of any kind and assumes no responsibility for any errors or omissions. No liability is assumed for incidental or consequential damages in connection with or arising out of information contained herein. This digital document is sold with the clear understanding that the publisher is not engaged in rendering legal, medical or any other professional services.

NANOTECHNOLOGY SCIENCE AND TECHNOLOGY

Additional E-books in this series can be found on Nova's website
under the E-book tab.

NANOTECHNOLOGY SCIENCE AND TECHNOLOGY

NANOSTRUCTURES AND FILMS BASED ON CLASSICAL WIDE GAP SEMICONDUCTORS FOR PHOTOVOLTAIC APPLICATIONS

ANATOLIY OPANASYUK
DENYS KURBATOV
HALYNA KHLYAP
AND
VIKTOR LAPTEV

New York

Copyright © 2014 by Nova Science Publishers, Inc.

All rights reserved. No part of this book may be reproduced, stored in a retrieval system or transmitted in any form or by any means: electronic, electrostatic, magnetic, tape, mechanical photocopying, recording or otherwise without the written permission of the Publisher.

For permission to use material from this book please contact us:
Telephone 631-231-7269; Fax 631-231-8175
Web Site: http://www.novapublishers.com

NOTICE TO THE READER

The Publisher has taken reasonable care in the preparation of this book, but makes no expressed or implied warranty of any kind and assumes no responsibility for any errors or omissions. No liability is assumed for incidental or consequential damages in connection with or arising out of information contained in this book. The Publisher shall not be liable for any special, consequential, or exemplary damages resulting, in whole or in part, from the readers' use of, or reliance upon, this material. Any parts of this book based on government reports are so indicated and copyright is claimed for those parts to the extent applicable to compilations of such works.

Independent verification should be sought for any data, advice or recommendations contained in this book. In addition, no responsibility is assumed by the publisher for any injury and/or damage to persons or property arising from any methods, products, instructions, ideas or otherwise contained in this publication.

This publication is designed to provide accurate and authoritative information with regard to the subject matter covered herein. It is sold with the clear understanding that the Publisher is not engaged in rendering legal or any other professional services. If legal or any other expert assistance is required, the services of a competent person should be sought. FROM A DECLARATION OF PARTICIPANTS JOINTLY ADOPTED BY A COMMITTEE OF THE AMERICAN BAR ASSOCIATION AND A COMMITTEE OF PUBLISHERS.

Additional color graphics may be available in the e-book version of this book.

LIBRARY OF CONGRESS CATALOGING-IN-PUBLICATION DATA

ISBN: 978-1-62948-763-2

Published by Nova Science Publishers, Inc. † New York

CONTENTS

Preface		**vii**
Chapter 1	Introduction	**1**
Chapter 2	Optical and Structural Properties of A^2B^6-Based Structures	**3**
Chapter 3	Led Sulfide and Mercury-Cadmium-Zink-Telluride Thin Film-Based Heterostructures	**33**
Chapter 4	Improving Contacts for High-Effective Solar Cells	**97**
References		**129**
Index		**133**

PREFACE

Design of high-effective photovoltaic devices needs not only nanoscaled materials and structures but also classical semiconductors with various widths of the gap and microscaled heterojunctions. Our review describes the principal physical chemical properties of wide gap semiconductors making it possible to use these materials for practical applications. The authors consider methods of fabricating films and nanostructures with controllable characteristics. The structural properties are presented. The optical and electrical characteristics and effects of different defects (structural and point defects, one- and two-dimensional defects) are also shown. Further we present the current mechanisms and influence of the material interface perfectness as well as examples of the band diagrams of these heterostructures. The properties of A^2B^6-heterosystems are classified from the point of view of their applications in solar energy, optoelectronics and sensorics. The next part highlights electrical characteristics of heterostructures based on thin films of PbS and solid solution ZnCdHgTe. In conclusion we show unique properties of nanostructured metallic cluster contacts obtained by chemical technology for high effective solar cells.

Chapter 1

INTRODUCTION

Classical semiconductors with various gap widths (ZnTe, CdTe, PbS, etc.) and ZnCdHgTe solid solutions (bulk material and thin films) are attractive components for modern photovoltaic applications. Regardless some technological challenges in fabricating high-quality materials, these compounds remain basic ones for design of solar cells, led-emitting diodes and other electronic and optical devices. Usually, CdTe and ZnTe films have some specific structural peculiarities, namely the electrically active point and extended defects [1]. Therefore they have strong effect on the optical and photoelectrical properties of thin films and thus considerably determine solar cells efficiency [1]. Further increase in the efficiency of CdTe-based solar cells can be reached only by obtaining structurally perfect CdTe films as a result of the optimization of their defect structure.

Now we consider important aspects of using materials mentioned above for photovoltaic and microelectronic applications.

Chapter 2

Optical and Structural Properties of A^2B^6-Based Structures

Low-Temperature Photoluminescence of II-VI Films Obtained by Close-Spaced Vacuum Sublimation [1]

The low temperature photoluminescence (PL) measurements are very effective method to investigate the defect structure in the various semiconductor materials including the polycrystalline thin films [1 and refs. therein]. It makes it possible to determine the nature and energy levels of the defects as well as the relative concentration of dislocations in the films. Besides that, the excitonic PL lines are also very sensitive to the point defects in the semiconductors. At present, the PL properties of bulk crystals of II-VI group semiconductors are studied well enough [1and refs. therein], but at the same time thin films of these materials have not been thoroughly investigated.

The main objective of the paper is the study of the PL properties of CdTe and ZnTe polycrystalline films deposited by closed space vacuum sublimation (CSVS) under different condensation conditions in order to determine the optimal growth conditions of these films with good optical quality.

Thin films were deposited on previously cleaned glass substrates by CSVS method [1]. The powder of the stoichiometric compounds was used as a source material. During the deposition of these thin films the

evaporator temperature was as follows: CdTe (T_e = 873 K) and ZnTe (T_e = 973 K). The substrate temperature T_s for CdTe and ZnTe films varied from 473 K to 823 K and from 573 K to 873 K, respectively. The thickness (l) of the as-deposited films was measured to be between 6–8 μm using the cross-section microphotography. The undoped CdTe and ZnTe thin films have *p*-type conductivity.

The PL spectra were measured using an SDL-1 grating spectrometer [1]. An LGN-404 argon laser was used for excitation by the 488.8 nm line, together with an FEU-62 photomultiplier in the photon-counting mode. The excitation intensity was kept below 1.0 W/cm^2 to avoid sample heating. The samples were mounted on the cold finger of a variable temperature liquid-helium cryostat. The accuracy of the measurements and temperature stabilization by the UTREKS system was 0.01 K. The exciting beam was modulated by a mechanical chopper and the luminescence signal was measured using a phase-sensitive lock-in detection system. The spectral resolution of the system was of the order of 1-2 cm^{-1} (0.1 – 0.2 meV).

The low temperature photoluminescence (PL) measurements are very effective method to investigate the defect structure in the various semiconductor materials including the polycrystalline thin films [1]. It makes it possible to determine the nature and energy levels of the defects as well as the relative concentration of dislocations in the films. Besides, the excitonic PL lines are also very sensitive to the point defects in the semiconductors. At present, the PL properties of bulk crystals of II-VI group semiconductors are studied well enough [1 and refs. therein], but at the same time thin films of these materials have not been thoroughly investigated.

The main objective of the paper is the study of the PL properties of CdTe and ZnTe polycrystalline films deposited by closed space vacuum sublimation (CSVS) under different condensation conditions in order to determine the optimal growth conditions of these films with good optical quality.

Thin films were deposited on previously cleaned glass substrates by CSVS method [1]. The powder of the stoichiometric compounds was used as a source material. During the deposition of these thin films the evaporator temperature was as follows: CdTe (T_e = 873 K) and ZnTe (T_e = 973 K). The substrate temperature T_s for CdTe and ZnTe films varied from 473 K to 823 K and from 573 K to 873 K, respectively. The

thickness (l) of the as-deposited films was measured to be between 6–8 μm using the cross-section microphotography. The undoped CdTe and ZnTe thin films have p-type conductivity.

The PL spectra were measured using an SDL-1 grating spectrometer [1]. An LGN-404 argon laser was used for excitation by the 488.8 nm line, together with an FEU-62 photomultiplier in the photon-counting mode. The excitation intensity was kept below 1.0 W/cm^2 to avoid sample heating. The samples were mounted on the cold finger of a variable temperature liquid-helium cryostat. The accuracy of the measurements and temperature stabilization by the UTREKS system was 0.01 K. The exciting beam was modulated by a mechanical chopper and the luminescence signal was measured using a phase-sensitive lock-in detection system. The spectral resolution of the system was of the order of 1-2 cm^{-1} (0.1 – 0.2 meV).

The growth process, structural and substuctural characteristics of the chalcogenide thin films were investigated in our works earlier [1and refs. therein]. It was found out that the films obtained at the growth conditions near the thermodynamic equilibrium by CSVS method have a columnar-like structure with the clear growth texture characterized by the low concentration of stacking fault defects and dislocations density. Both CdTe and ZnTe films have zinc-blende structure [1 and refs. therein].

The optical quality is an important property of the CdTe polycrystalline films since that determines the efficiency of their various applications. The PL measurements are a powerful tool to obtain this information. It makes it possible to determine the nature and energy levels of both the intrinsic defects and the residual impurities in the semiconductor materials [1 and refs. therein].

Figure 1 shows PL spectra of the CdTe polycrystalline films at 4.5 K for the samples obtained at the different substrate temperatures. Curves 1-4 correspond to the CdTe films obtained at T_s equals to 473, 523, 623 and 823 K, respectively. The highest intensity I_1-line in the PL spectra of CdTe films is observed at 1.545 eV. Since the band gap energy of CdTe at 4.5 K is 1.606 eV, this line can be caused by the emission with the participation of free electrons and the shallow acceptor level with the energy about 60 meV. In this case, the recombination of free electrons with the acceptor holes occurs. The acceptor level [1] may be caused by the presence of Na or Li residual impurities in CdTe films. This impurity atoms are the typical residual impurities in II-YI compounds [1 and refs.

therein]. The low intensity lines observed on the long-wavelength wing of the I_1-line correspond to the 1LO- and 2LO-phonon replicas of the observed line. At the same time, these lines may be caused by the recombination of the donor electrons with the energy E_c – 0.010 eV and the acceptor holes with E_v + 0.050 eV. In this case, the acceptor level corresponds to the single charged cadmium vacancies [1].

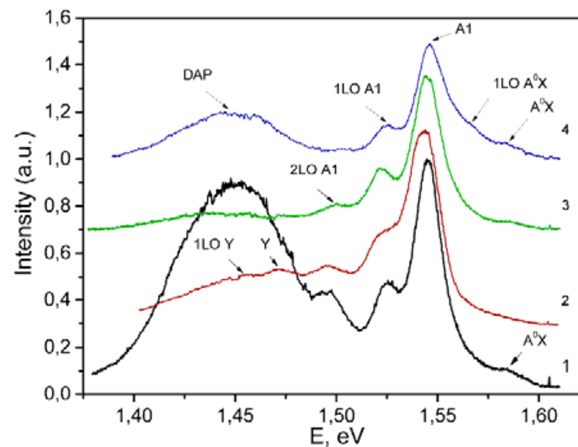

Figure 1. 4.5 K PL spectra of a CdTe polycrystalline film grown by CSVS under different condensation conditions, T_e = 873 K; T_s, K: 473 (1), 573 (2), 623 (3), 823 (4).

Additional information about the nature of intrinsic defects and residual impurities may be obtained as a result of the analysis of the PL spectra in the excitonic region. As can be seen from Figure 1, the low intensity line at 1.586 eV is observed on the short-wavelength wing of the I_1-line. The energy position of this line indicates the appearance of the recombination of acceptor bound excitons, i.e. the A^0X-line [1]. The fact that we are able to observe the excitonic line in the PL spectra indicates that the CdTe films are of good optical quality. Furthermore, the presence of the A^0X-line indicates that these films are p-type. Thus, it leads us to expect that the concentration of the donor centers in the CdTe films is insignificant. The appearance of the A^0X-line in the PL spectra may be provided only by the presence in these films of the acceptor level with the energy E_v + 0.060 eV caused by the Na (Li) residual impurity. It should be noted that the acceptor level with this energy was observed in

CdTe crystals using the time-resolved photoelectric spectroscopy technique [1].

Analysis of the observed PL spectra also reveals a broad band in the energy region 1.38-1.50 eV. On the one hand, this band is caused by the recombination of the donor-acceptor pairs (DAP) with the participation of the acceptor complexes. On the other hand, the presence of the 1.47 eV emission band is caused by extended defects like dislocations [1]. Therefore, the PL intensity in this spectral range can be used as a measure to evaluate the relative dislocation density. It should be noted that the acceptor complex includes a doubly charged cadmium vacancy (V_{Cd}^{2-}) and a singly ionized donor (D^+). The ionized donors can be the residual impurities of group III atoms positioned on cationic sites [1 and refs. therein], which also are present in pure CdTe.

As can be seen from Fig 1, the most intensity of the broad band corresponds to the films obtained at T_s = 473 K. In the case of the films obtained at T_s = 623 K the intensity of broad band is insignificant. It indicates that for CdTe films obtained under such growth condition the dislocation density is small. This result is in accordance with the data obtained in [1], where the minimum of the total dislocations density in CdTe films corresponds to the substrate temperature T_s = 623 K. It was shown [10] that the dislocations are situated, in main, on the coherent scattering domain (CSD) boundaries. It can be seen from Figure 1 that the intensity of broad PL band of the CdTe films with T_s = 823 K is considerable. Therefore, the dislocation density for these films is larger than in the case of films with T_s = 623 K. In addition, the concentrations of stacking faults (SF) in thin films obtained at T_s = 823 K is four times more than for the CdTe films with T_s = 623 K [1 and refs. therein].

Figure 2 shows the PL spectra of ZnTe films grown at different substrate temperature. The very narrow I_X-line at 2.3837 eV, which available in all spectra of the samples grown at different T_s, is attributed to the recombination of free excitons [1 and refs. therein]. The I_{A1}-line at 2.3753 eV observed for the sample obtained at T_s = 573 K is associated with the radiative recombination of an excitonic emission bound to neutral shallow acceptor (namely Cu, Li or Na] [1 and refs. therein]. In this case the exciton binding energy on the impurities is 8.4 meV. The emission in the spectral range 2.25 – 2.33 eV is due to the DAP recombination [1 and refs. therein].

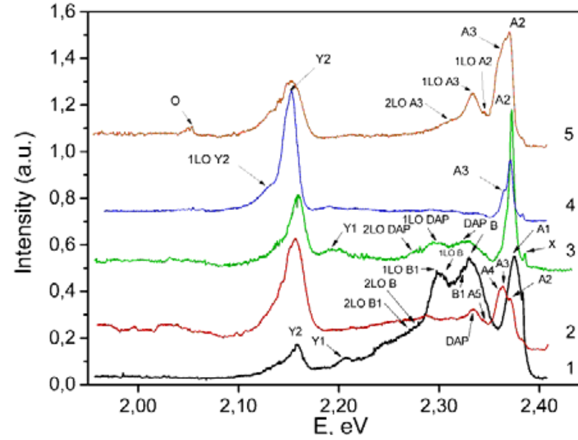

Figure 2. 4.5 K PL spectrums of a ZnTe polycrystalline film grown by CSVS under different condensation conditions, T_e = 973 K; T_s, K: 573 (1), 623 (2), 673 (3), 723 (4) 873 (5).

The I_B-line at 2.3300 eV corresponds to zero-phonon transition followed at lower energy by its longitudinal-optical (LO) phonon replicas at 2.3038 (1LO) and 2.2776 (2LO). It was shown [29] that in this case the donor and acceptor ionization energies are 22 and 51 meV, respectively. It is considered that the former level is due to Cl_{Te} donor [1 and refs. therein], while the acceptor level can be ascribed to the presence of vacancy zinc V_{Zn}. Another faint I_{Cu}-band at 2.245 eV is ascribed to free-to-band transitions with the participation of an Cu_{Zn} acceptor level with binding energy E_A = 149 meV [1 and refs. therein] assuming the band gap energy of ZnTe at low temperature of 2.394 eV [1 and refs. therein].

The weak intensity I_{Y2}-band at 2.1588 eV is also detected in the PL spectrum of the sample grown at T_s = 573 K. The energy position of this band is close to Y_2-band observed earlier in the heteroepitaxial ZnTe layer at 2.147 eV [1 and refs. therein]. This band is related to structural defects like dislocations, which may influence the electronic properties of the ZnTe-based materials [1 and refs. therein]. As a result of the presence of these defects, the electric and elastic strain fields are produced in ZnTe. Such fields can shift the already existing energy levels caused by the intrinsic defects and residual impurity atoms. Usually, the PL spectra of ZnTe show Y_1- and Y_2-bands, where the first is related to

the structural defects created at the grain boundary or zones of high dislocation density [1 and refs. therein]. For the film grown at T_s = 573 K the Y_2-band was not observed and, therefore, such structural defects in this sample are absent. It should be noted that the presence of dislocations and stacking defects into bulk crystallites of ZnTe and CdTe films was earlier observed by us using X-ray methods [1 and refs. therein].

The ZnTe films grown at T_s = 623 K exhibits a strong intensive Y_2-band emission at 2.1557 eV and relatively weak exciton-relative lines at 2.3811 eV (I_X), 2.3697 eV (I_{A2}), and 2.3625 (eV) I_{A3}. The I_{A2}-peak is attributed to an emission from excitons bound to neutral acceptor due to the residual impurities such as Li, Na or P [1 and refs. therein]. The exciton binding energy on the impurity turns out to be 11.4 meV, and 18.6 meV for I_{A2}- and I_{A3}-lines, respectively. According to [1 and refs. therein], the appearance of I_{A3}-lines is attributed to an acceptor complex, namely, a donor associated to a substitution IV-group atom (C or Si) on a Te site or a Zn vacancy. Since this line was also observed in the samples group under Zn-rich ZnTe conditions, the first notation is more likely [1 and refs. therein]. Thus, this line is due to the emission of excitons bound to a carbon atom on a Te site, i.e. C_{Te} acceptor. As could be seen on Figure 2, in the excitonic region of the PL spectrum, three shoulders at 2.3602 (I_{A4}) eV, 2.3504 eV (I_{A5}), and 2.3438 eV were also observed. The line at 2.3438 eV corresponds to 1LO-phonon replicas of the I_{A2}-line, while I_{A4}- and I_{A5}-lines may be associated with another neutral acceptors of unknown nature. In particular, these lines may be ascribed to the presence of Cl related centers, namely a complex composed of Zn vacancy and Cl on Te site (V_{Zn}–Cl_{Te}) [1 and refs. therein]. The exciton binding energies on these acceptor centers are 20.9 meV and 30.7 meV, respectively. The line at 2.3327 eV (I_{DAP}), which is attributed to the recombination of DAP, followed 1LO- and 2LO-phonon replicas.

At T_s = 673 K, an intense I_{A2}-line appears in the PL spectrum at 2.3711 eV as well as a weak free exciton emission (I_X-line) at 2.3834 eV. The I_{A2}-line, ascribed to the radiative recombination of an excitonic emission bound to neutral shallow acceptor, is dominant in the PL spectrum. The DAP emission bands also appear in this spectrum at 2.3240 eV, 2.2977 eV, and 2.2715 eV. Last two bands are due to 1LO- and 2LO-phonon replicas of the line at 2.3240 eV. In this spectrum, there also observed Y_2-band followed its LO-phonon replica. Another I_{Y1}-band

at 2.1914 eV may also be related to structural defects, likely dislocations. This band is observed for the films grown at different T_s, but its energy position depends on the growth conditions of the films and corresponds to the energy region of 2.1906 – 2.2125 eV. A further increase of the substrate temperature to T_s = 723 K leads to a strong increase in the intensity of the Y_2-band at 2.1529 eV. This indicates a significant increase of the density of dislocations in the sample. The ILO-phonon replicas of this band at 2.1296 eV also are observed in the spectrum. Similarly to the spectrum obtained for the samples grown at T_s = 673 K, in this case the intense I_{A2}-line at 2.3716 eV is also observed, which have been assigned to an exciton bound to neutral acceptor. This acceptor may be due to the residual impurities such as Li, Na or P [1 and refs. therein]. It should be noted that some difference of energy for the I_{A2}-line for the films grown at different T_s may be due to the influence of dislocations on the energy position of the impurity levels. The PL bands observed at 2.3558 – 2.2286 eV are associated with the recombination of DAP and their LO-phonon replicas. The most intense I_{A2}-line for the film grown at T_s = 873 K appears at 2.3702 eV followed by 1LO-phonon replicas at 2.3445 eV. The shoulder on the low-energy edge of the I_{A2}-line appears at 2.3625 eV, which corresponds to the I_{A3}-line similarly to the spectrum obtained for the sample grown at T_s = 623 K. The presence of the I_{A3}-line confirms the occurrence of a C_{Te}-D_{Zn} complex in the films. This line is followed by the 1LO- and 2LO-phonon replicas at 2.3363 eV and 2.2310 eV, respectively. Besides that, the band-edge region emission other PL bands can be identified at 2.1526 eV and 2.2125 eV, which is due to the presence of the dislocations in the sample. The weak I_O-band at 2.0542 eV which is observed in the PL spectrum for the film grown at T_s = 873 K is associated with the presence of oxygen, namely, O_{Te}-centers and its complexes [1 and refs. therein]. Since this band appears in the film grown at high substrate temperature, it indicates that the oxygen concentration is strongly depending on the vacuum conditions of the film deposition. In our case the oxygen concentration is low for the different growth conditions.

In summary, the low temperature photoluminescence spectra of CdTe and ZnTe thin films prepared by the close-spaced vacuum sublimation technique under different growth temperatures were investigated and their structure was analyzed. It was shown that the A^oX-line observed for the CdTe films is caused by the recombination of

acceptor bound excitons. The intensity of this line is low. The most intensive line at 1.545 eV is caused by the emission with the participation of free electrons and the shallow acceptor level with the energy about 60 meV. Such acceptor is attributed to the Na or Li residual impurities in CdTe films. The appearance of the broad PL band in the low-energy region (1.38-1.50 eV) is caused by the recombination of the donor-acceptor pairs (DAP) with the participation of the acceptor complexes of type (V^{2-}_{Cd} $+D^{+}$). The presence of the 1.47 eV emission band is caused by extended defects like dislocations. These two bands are practically absent in the PL spectrum of the sample grown at T_s=623 K. It indicates that the optimal temperature conditions of the growth of polycrystalline CdTe films correspond to the following temperatures: T_e = 873 K and T_s = 623 K. These films have a single cubic phase with the low dislocation density and stacking faults defect concentration. The PL spectra of the investigated ZnTe films grown at different T_s show the emission of the free excitons along with the intense lines attributed to the excitons bound to the neutral acceptors. The appearance of the acceptors is associated with the Li, Na, P or Cu residual impurities. The DAP emission has small intensity which indicates the presence of low concentrations of complex acceptor centers in the ZnTe films. In addition to this emission, the PL spectra show other bands in the low-energy region (2.10-2.22 eV) which are related to structural defects like dislocations. The emission of these bands and the lines related to the radiative recombination of the excitons bound to the neutral acceptor strongly depend on the growth condition of the ZnTe films. It was established that the optimal conditions of the ZnTe film growth correspond to the substrate temperature of T_s = 673 K. For such films, the line associated with the recombination of the excitons bound to neutral shallow acceptors, which are attributed to the Li, Na or P residual impurities, is dominated, while the intensity of the band related to the dislocations is smaller. It should be noted that in the investigated PL spectra, the band attributed to the oxygen impurity is practically absent. Thus, the study of the PL spectra of the investigated CdTe and ZnTe films makes it possible to determine their optimal growth condition in order to obtain the films of good optical quality. The obtained results are in good agreement with the structural investigations carried out earlier by us using X-ray diffraction technique [1 and refs. therein].

STRUCTURAL AND OPTICAL PROPERTIES OF VACUUM-DEPOSITED ZNS NANOSTRUCTURES [2]

Zinc sulfide as a traditional luminescent material which has attracted attention of material scientists due to its properties suitable for designing new low-cost and reliable solar and photovoltaic devices and opto- (acusto-) electronic active elements. Light emitting diodes (LEDs), photodetectors, sensors, electro-optical modulators, and optical cover layers, etc. based on ZnS successfully function for decades [2 and refs. therein]. Zinc sulfide doped with Cu or Mn is a good powder phosphor having about 100% quantum efficiency [2 and refs. therein].

ZnS films and nanosized particles are now being of particular interest as perspective base for constructing functional devices with unique characteristics. Among them are nanoscaled electronic devices, lasers, sensors, and chemical, gas and biological detectors etc. [2 and refs. therein].

Despite the enormous number of references concerning the preparation of ZnS-based nanostructures the question of producing these structures at low substrate temperatures (less than 500 ^{0}C) without catalyst is not highlighted until recently.

The aim of this part of our work is to show the effect of deposition temperature at preparing ZnS films on monocrystalline wafers with large lattice parameter discrepancy on morphology, structure and substructural features of the layers.

Films and nanostructures of zinc sulfide were prepared by vacuum evaporation of the material with semiconductor-quality purity in quasi-closed volume (close-spaced vacuum sublimation (CSVS)) [2 and refs. therein]. High-purity monocrystalline cubic ZnSe wafers were used as substrates. The deposition was performed onto the crystallographic (220) plane. The evaporator temperature was T_e = 900 ^{0}C. The substrate temperature had been changed in the range T_s = (150-550) ^{0}C. Time of deposition was about 600 s.

High-resolution scanning electron microscopy was applied for studying the morphology of the samples (JEOL JSM-6510).

EDAX and SEM (REMM-103-01) methods enabled to determine the element composition of the films and nanostructures.

Structural investigations were carried out with using X-ray diffractometer DRON 4-07 (Ni-filtered K_α-radiation of Cu-anode). The

spectra were registered in the angle range 2θ from 20^0 to 80^0, where 2θ is the Bragg angle. X-ray radiation was focused according to the Bragg-Brentano method. The spectra were normalized by zinc intensity of (220) ZnSe peak. The phase analysis was carried out by comparing interplane distances and specific intensities of diffraction patterns from the investigated samples and etalon JCPDS [2 and refs. therein].

The quality of the film texture had been estimated by the Harris method [2 and refs. therein]. The pole density was calculated as $P_i = \frac{(I_i/I_{0i})}{\frac{1}{N}\sum_{i=1}^{N}(I_i/I_{0i})}$ where I_i, I_{0i} are integral intensities of i-diffraction peak of the sample and etalon; N is a number of lines in the X-ray diffraction pattern. The dependencies P_i - φ (where φ is an angle between chosen direction and the normal to different crystallographic planes corresponding to the reflexes in the XRD patterns) were built on the base of the calculation. The angle φ was calculated for cubic and hexagonal lattices according to expressions given in [2 and refs. therein]. The axis of the texture has values corresponding to the maximum P_i. The orientation factor was calculated as $f = \sqrt{\frac{1}{N}\sum_{i=1}^{N}(P_i - 1)^2}$. The charge was used as the etalon of the textured sample.

The interplane distances for sphalerite and wurtzite phases of the chalcogenides were carried out by position of $K_{\alpha 1}$ component of all the most intensive lines registered in XRD-patterns. The expression $a = \lambda \frac{(h^2 + k^2 + l^2)^{1/2}}{2\sin\theta}$ (where λ is X-ray wavelength) was used for calculating the lattice parameter of the cubic phase of materials [2 and refs. therein].

Lattice parameters a and c of the hexagonal phase for ZnS were calculated according to the next expressions

$$a = \frac{\lambda}{2\sin\theta}\sqrt{\frac{4}{3}(h^2 + hk + k^2) + \left(\frac{a}{c}\right)^2 l^2},$$

$$c = \frac{\lambda}{2\sin\theta}\sqrt{\frac{4}{3}\left(\frac{c}{a}\right)^2 (h^2 + hk + k^2) + l^2},$$

where *c/a* value was suggested to be 1.639 [2 and refs. therein]. We have used reflexes contributing negligible calculation error (reflexes (100), (110) and (102) for the determination of *a*, and reflex (002) for the parameter *c*) [2 and refs. therein].

Further we have applied the Nelson – Riley extrapolation method for more precise determination of the parameters *a* and *c* for both phases [2 and refs. therein]. Least-squares method has enabled to linearly approximate the obtained numerical values.

The XRD results were also used for the description of the coherent scattering domain (CSD) size in the films, especially for determination of their arbitrary size from FWHM [2 and refs. therein]. We suggested that the physical line broadening is due to the dispesiveness of CSDs only. Then the maximal values of CSD size (L) in the films can be calculated using the Scherer's relation $L = \frac{K\lambda}{\beta\cos\theta}$, where $K \sim 0.9$ is a coefficient weakly depending on the grain shape, β is a physical broadening of the X-ray line.

To differentiate the diffraction broadening due to physical (β) and instrumental (b) effects the profiles of X-ray lines were approximated by Gauss and Cauchy functions.

Transmission IR-spectra of ZnSe substrates and the systems substrate-film in the ave number range (500-4000) cm^{-1} are recorded with using IR-Fourrier-spectrophotometer SPECTRUM ONE (Perkin-Elmer). Transmission spectra of ZnS films and nanostructures are obtained subtraction of the transmission coefficients of the bilayered system and substrate. The well-known procedure [2 and refs. therein] was used for the simplification of further analysis.

Figure 3 displays images of the surface for ZnS films and nanostructures.

It is found that condensates deposited at T_s = 150 ^{0}C have a fractal-like structure (Figure 3 a), the nanowires of some hundred nm length had been grown as the substrate temperature was elevated (T_s = (240, 350) ^{0}C). The calculation demonstrated the thickness of these nanowires about

(15-80) nm (Figure 3 e). We have observed some reduction of the nanowire's arbitrary thickness at the increase of the condensation temperature (Figure 3 b, c). It should be noted that the images of nanowires obtained at T_s = 240 ^{0}C and 350 ^{0}C are not identical because of changes in seed formation mechanism under the change of the substrate temperature. At T_s = 550 ^{0}C the polycrystalline ZnS film was formed at the surface of ZnSe single crystals, the grain size was estimated to be D~0.34 μm.

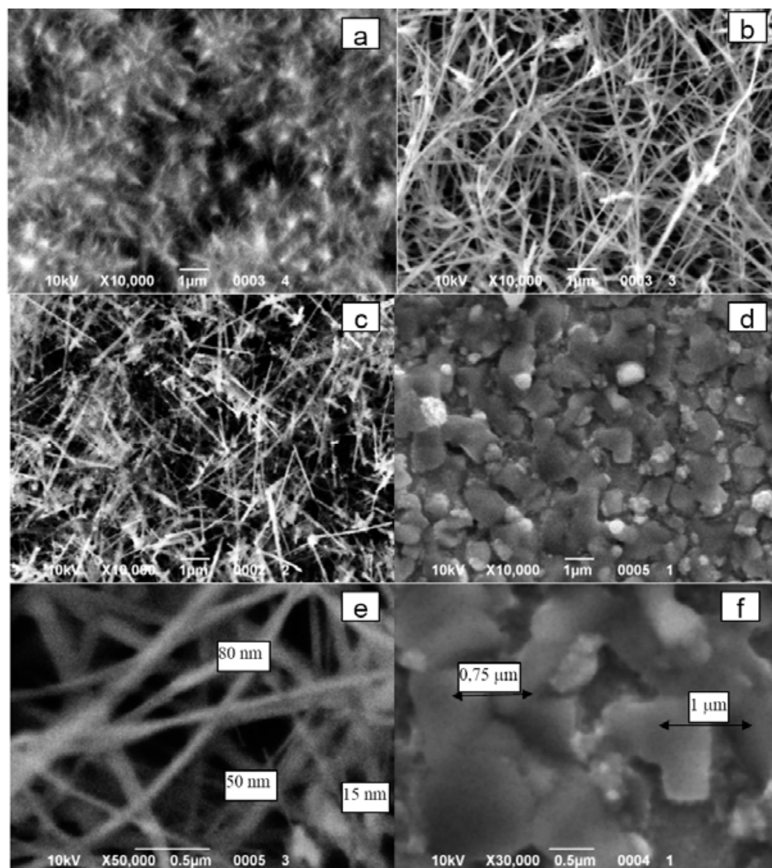

Figure 3. Surface micrographs of ZnS films and nanostructures prepared at different substrate temperatures T_s: 150 ^{0}C (a); 240 ^{0}C (c, d); 350 ^{0}C (b); 550 ^{0}C (e, f).

The technology described in this work does not use the previous catalyst (Ag, Au or other metallic nanodots) for growth of ZnS nanostructures [2 and refs. therein]. We suggest it possible while ZnSe monocrystalline substrates were used at the condensation. As the lattice parameters of ZnSe and ZnS are sufficiently different the epitaxial three-dimensional ZnS seeds are formed on the substrate (Wolmer-Weber or Stranski-Krastanov growth mechanisms [2 and refs. therein]) which are transforming in nanowires.

Figure 4 illustrates typical EDAX spectra for ZnSe monocrystalline substrate and bilayered system ZnS/ZnSeThe spectra point out the lines of the compound components only, foreign contaminations are not registered due to high purity of the materials. Composition of ZnS is almost stoichiometric.

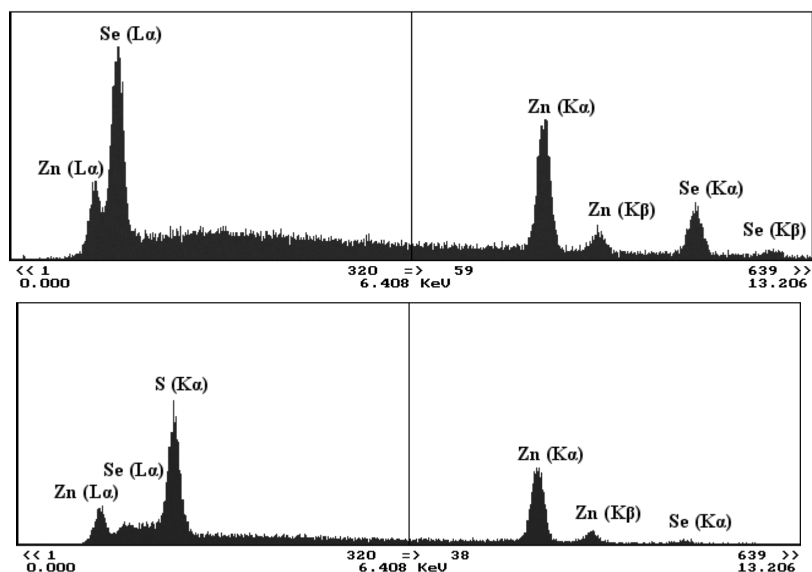

Figure 4. Characteristic EDAX spectra of the monocrystalline substrate (a) and the nanostructural ZnS layers (b) obtained at T_s=550 ^{0}C.

Figure 5 presents XRD patterns of bilayered systems ZnS/ZnSe. The strong peak is related to cubic ZnSe monocrystalline substrate (220) plane dominates at $(45.04\text{-}45.14)^0$. We have also registered very weak lines (<0.6%) 53.46^0, 65.12^0 and $(72.31\text{-}72.60)^0$ identified as reflexes

from the planes (311), (400) and (331) of the cubic phase ZnSe showing the block-like structure of ZnSe single crystal.

Along with the peaks mentioned above we have registered reflexes ~28.50^0, 47.60^0, and 56.60^0 from films and nanostructures based on ZnS. The peaks 47.60^0 and 56.60^0 were sufficiently broader than others. Experimentally revealed diffraction peaks may be interpreted as reflexes from the planes (111), (220), (311) of the cubic phase ZnS or we have reflexes from the planes (002), (110), (112) of the hexagonal phase. As the diffraction angles for crystallographic planes are practically coinciding their origin is not established until recently, However, the peaks of weak intensity (<1%) at 27.03^0-27.13^0 and $(40.40\text{-}40.50)^0$ corresponded to reflexes from the planes (100) and (102) of the hexagonal phase were also observed. It is enable us to conclude that the nanostructured layers and films have hexagonal structure, and peaks from planes (100), (002), (102), (110), and (112) wurtzite are also registered. This conclusion correlates with data of authors [2 and refs. therein] which have found that nanowires ZnS prepared in their experiments have hexagonal structure.

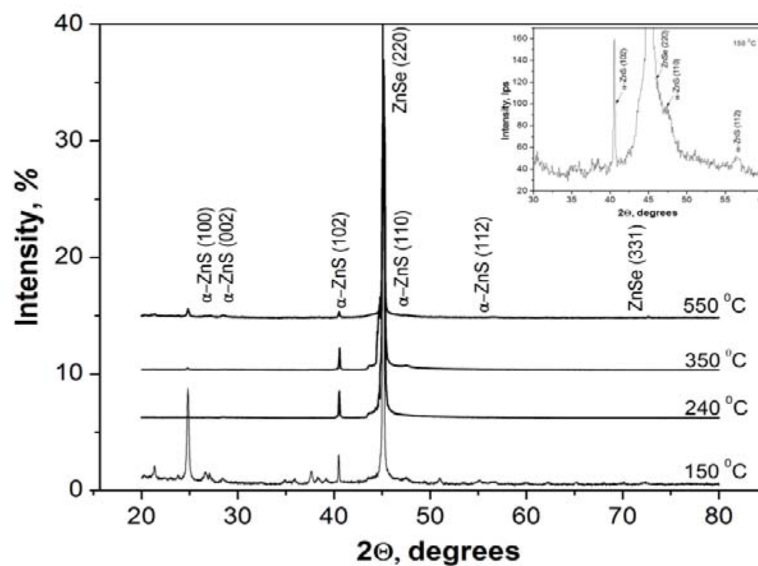

Figure 5. X-Ray diffraction patterns of bilayered structures ZnS/ZnSe prepared at different substrate temperatures T_s.

Table 1. Lattice parameters of ZnS and ZnSe

T_s, ^{0}C	ZnSe	ZnS					
	$a_{(220)}$, nm	$a_{(100)}$, nm	$a_{(110)}$, nm	$a_{(102)}$, nm	a_{H-P}, nm	$c_{(002)}$, nm	c_{H-P}, nm
150	0.56848	0.37920	0.38311	0.37414	**0.38186**	0.62670	**0.62484**
240	0.56774		0.38273	0.37361	**0.38311**	0.62562	**0.62676**
350	0.56882	0.38058	0.38319	0.37450	**0.38274**	0.62756	**0.62759**
500	0.56853		0.38324	0.37458	**0.38279**	0.62778	**0.62761**
Reference	0.56688	*a*=0.3811 nm, *c*=0.6234 nm [13]					

XRD-patterns of the sample grown at T_s=350 ^{0}C also demonstrate weak reflexes (<0.9%) from the planes (002) and (400) of the cubic phase ZnS at 59.91^0 and 70.04^0. Thus, it is possible to call the sample "bi-phase system". As we have mentioned above other samples have also single-phase structure of the hexagonal modification.

We have defined the lattice parameters of the materials according to the position of (220) line ZnSe and the most intensive lines ZnS. These values for the cubic phase of ZnSe and the hexagonal phase of ZnS are listed in Table 1. This Table also presents more precise values of *a* and *c* calculated by Nelson-Riley. It seen that the values of the lattice parameters for ZnSe are in the range *a* = (0.56775–0.56882) nm; these data are somewhat higher than those given in JCPDS [2 and refs. therein].

It should be noted that the values *a, c* of the hexagonal phase ZnS determined by reflexes from various crystallographic planes are sufficiently different. The lowest values *a* are obtained by the reflexes from the (102) plane: *a* = (0.37361-0.37458) nm, and the maximum ones are obtained by the reflexes from the (110) plane: *a* = (0.38273-0.38324) nm. It is known that the (110) plane is parallel to the axis *c* of the hexagonal lattice and, obviously, to the axis of the nanowires. Thus, the inter-planar distance in direction normal to the nanowire axis (by its thickness) is a maximal one among those calculated for various directions. The lattice parameters of nanostructures defined by the Nelson-Riley method (*a* = 0.38186-0.38311 nm, *c* = 0.62484-0.62676 nm) are somewhat larger than reference values for bulk single crystals (*a* = 0.3811 nm, *c* = 0.6234 nm [2 and refs. therein]) but they good correlate with data for nanowires (*a* = 0.38210 nm, *c* = 0.62573 nm [2 and refs. therein]).

There is a trend of increasing values of lattice parameters ZnS obtained using reflexes from various crystallographic planes and the Nelson-Riley method as the condensation temperature increases. We suggest that this effect is due to building-up Se atoms evaporated from the substrate into ZnSe lattice.

Reverse pole figures from the Zn nanostrutures obtained at various substrate temperatures are shown in Figure 6 a. As it seen, the samples are textured. Along this, the dominated orientations of crystallites and nanowires ZnS are [102], [002], and in sample deposited at T_s=150 ^{0}C, is the [112]-direction. The form-factor values for investigated samples are *f*

= 1.52-1.96. These data are larger then those obtained us early for ZnS films on disordered substrates under the same technological conditions [2 and refs. therein].

The CSD sizes in directions normal to the crystallographic planes (110), (002) and (102) are calculated by the physical of diffraction reflexes of ZnS hexagonal phase. Figure 6 d plots the results. As is seen the SCD sizes by direction *c* of the wurtzite lattice ($L_{(002)}$) and in perpendicular direction ($L_{(110)}$) are different in some cases. This difference is very good seen in nanostructured condensates prepared at the substrate temperatures T_s = 240 ^{0}C, 350 ^{0}C. In this case value of $L_{(002)}$ takes care of length, and $L_{(110)}$ stands for thickness acknowledging that nanowires grow in direction [002]. Obvious, the arbitrary thickness of nanowires decreases 18.5 nm down to 16 nm in condensates obtained at T_s=250 ^{0}C and 350 ^{0}C. These data are in good correlation with those obtained from microscopic studies and reflect the trend of decreasing thickness of nanowires under increase of T_s described above. SCD sizes in direction of the crystallographic wurtzite axis *c* $L_{(002)}$=(102.7-113.1) nm are somewhat lesser then those registered by electron microscopy (about some hundreds nm) pointing out that nanowires can have some SCD by length. In polycrystalline ZnS films deposited at T_s=500 ^{0}C the SCD sizes in various directions are almost the same.

IR-spectroscopy is often applied for determining composition and purity of films and nanostructures ZnS [2 and refs. therein]. Transmission spectra of ZnSe substrates and bilayered systems ZnS/ZnSe are plotted in Figure 7 a. Figure 7 b shows transmission spectra of the films and nanostructures ZnS obtained by subtraction of these spectra. As is seen, the maximum transmission coefficient in all the range of investigated wave numbers belongs to the nanostructured ZnS layers deposited at T_s=150 ^{0}C and 240 ^{0}C.

The weaker light transmission of the nanostructured sample prepared at T_s=350 ^{0}C may be explained by presence of solid ZnS layer at the ZnSe hetero-interface. As it was mentioned above, this sample has a binary phase structure: hexagonal structure with inclusions of the cubic phase. The solid epitaxial film grown at T_s=500 ^{0}C has a minimum *T* value. We have to note that the IR-transmission spectra of films and nanostructures ZnS deposited in vacuum have no sharp absorption lines (unlike the layers prepared by chemical methods [2 and refs. therein]). This fact demonstrates high purity of condensates and acknowledges data

obtained by EDAX. In particular, the spectra show no absorption in the range 3000 cm^{-1} due to valent oscillations of N-H group, 1588 cm^{-1} – NH_2, 1029 cm^{-1} – C- N, lines 1080 and 1352 cm^{-1} bound with CH_2 by groups commonly presented in spectra of chemically deposited films. There is no line at 1667 cm^{-1} due to oxygen presence and at 423 cm^{-1} due to ZnO formation.

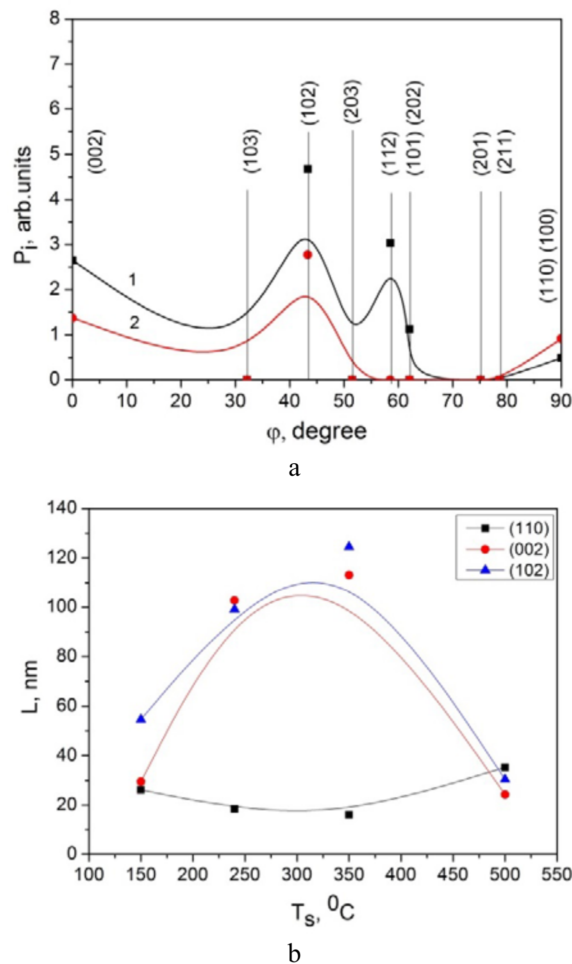

Figure 6. Pole density P_i as a function of the incidence angle φ between the [002] direction and the normal to the reflection plane for ZnS nanostructures, T_s ^{0}C: 150, 350 (a); Effect of the substrate temperature on the CSD size (b).

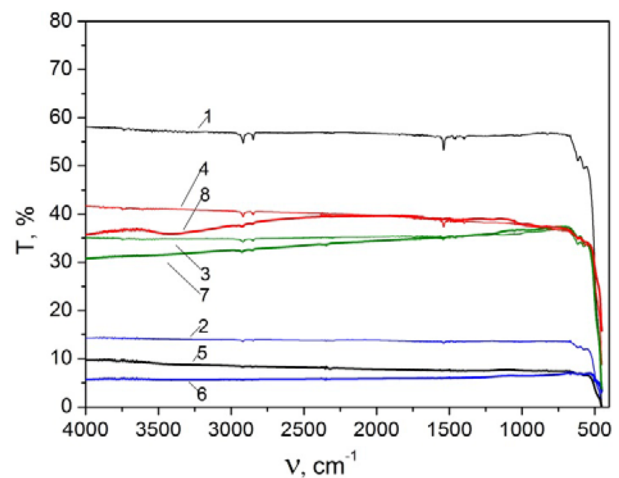

.

a

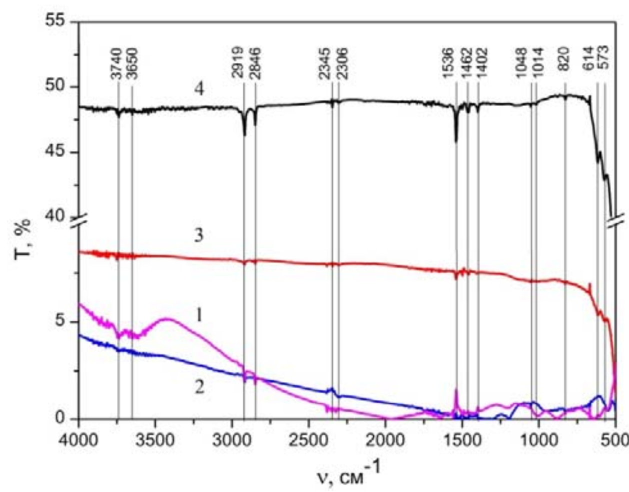

b

Figure 7. IR-spectra of the substrates ZnS (1-4) and bilayered ZnS/ZnSe structures (5-8) (a), ZnS films and nanostructures (b) prepared at T_s, ^{0}C: 150 (1); 240 (2); 350 (3); 500 (4).

However, the IR-spectra show some weak absorption lines. Table 2 lists values of wave number and energy for these lines. The absorption lines observed in the spectra in the wave number range (3356-3759) cm^{-1}

and (1274-1594) cm^{-1} are (on our opinion) due to valence oscillations of OH groups, for the range (2778-3268) cm^{-1} by the same vibrations of the $=CH_2$ groups, and the group C(OH) contributes for the range (1030-1282) cm^{-1}, the group CO_2 is responsible for the line 2345 cm^{-1} [2 and refs. therein].

Impurities containing hydrogen and oxygen atoms could contaminate material due to the strongly inhomogeneous relief of the samples at oxidation of the products exposed to air after preparation before placing samples into chamber for IR-investigations. Carbon atoms could penetrating the films and nanostructures under vacuum evacuation of the samples.

In conclusion, it is shown that nanostructural ZnS layers can be prepared by the CSVS method on monocrystalline ZnSe wafers without using Au nanodots or other metallic nanodots as catalyst. It is found out that changing the substrate temperature leads to production of films with various surface reliefs: fractal relief, nanofibers, and solid polycrystalline layers. Diffractometric (XRD) studies of the samples allowed to establishing there hexagonal structure with the lattice parameters a = (0.38186-0.38311) nm, c = (0.62484-0.62676) nm. It is shown that the nanorods are growing along the [001] direction of vurtzite. The size of the SCD size in direction of c axis and in the normal direction according to axis of the nanostructure in the lattice of the given phase is determined with taking into account the half-width of the diffraction lines ($L_{(002)}$ =(102.7-113.1) nm) and in the normal direction ($L_{(110)}$ = (16.0-18.5) nm). Comparing these results and data of microelectronic microscopy enabled us to demonstrate that the nanorods are monocrystalline by thickness, at the same time they contain some SCD by length. EDAX and IR-spectrometry acknowledged high chemical purity of ZnS films and nanostructures.

STRUCTURAL CHARACTERISTICS OF $Zn_{1-x}Mn_xTe$ POLYCRYSTALLINE FILMS [3]

The material science researchers are drawing their attention to the semi-magnetic solid solution $Zn_{1-x}Mn_xTe$ thin films as an unique object with perspective photoluminecsent, magnetic and magneto-optical features making it possible to use these compounds for designing devices

of micro- and optoelectronics, photovoltaics and spintronics [3 and refs. therein]. Change of the impurity concentration allows varying the band gap and the lattice constant of the solid solution which is important under formation of heterojunctions between this compound and other semiconductors. Thus, examining influence of physical technological conditions of condensation on the element composition and structural parameters of the thin semi-magnetic solid solution films is seemed to be important. However, the properties of $Zn_{1-x}Mn_xTe$ samples are not well examined until recently because of technological challenges (compound dissociation under evaporation and sufficient difference of the components' pressure). The thin 3-component layers of this compound are fabricated by methods partially compensating these troubles: MBE [3 and refs. therein], hot wall epitaxy (HWE) [3 and refs. therein], pulse laser deposition, MOVPE [3 and refs. therein] and others. We have here used the method of the close-spaced vacuum sublimation (CSVS). This technique thanking to the technical features of the evaporator allows obtaining stoichiometric films of multicomponent semiconductors of high purity under good controllable technological process [3 and refs. therein].

Thin films $Zn_{1-x}Mn_xTe$ were prepared on cleaned glass substrates under growth pressure in the chamber no more than $5\cdot10^{-3}$ Pa. The detailed description of the experimental setup for the CSVS technique is presented in [3 and refs. therein]. The charge of the semiconductor purity degree containing 10% Mn was evaporated. The evaporator temperature was T_e = 800 ^{0}C. The substrate temperature was changed in the interval T_s = (150-550) ^{0}C. The typical condensation time was about t = 15 min.

TEM technique (PEMMA-103-01) was used to investigate the morphology of the surfaces of the films. The arbitrary grain size (D) in condensates was determined according to the Jeffries method. Structural characteristics were examined by using films with the thickness l~ (2-4) μm, this value was determined from the photo-images of the cleavage surface of the condensates.

The structural investigations of $Zn_{1-x}Mn_xTe$ films were performed by the XRD unit DRON 4-07 in Ni-filtered K_α radiation of the copper anode in the angle range 2θ from 10^0 to 80^0, where 2θ is the Bragg angle.The Bragg-Brentano method was used to focus of the X-ray radiation. The experimental curves were normalized by the intensity of (111) peak of the cubic phase. The phase analysis was carried out by comparing inter-

plane distances and arbitrary intensities of the X-ray peaks from the investigated samples and the etalon according to data of JCPDS [3 and refs. therein].

The texture of the films was estimated according to the Harris method [3 and refs. therein]. The pole density was calculated using the expression $P_i = (I/I_{0i})/\{[1/N][\sum_{i=1}^{N}(I/I_{0i})]\}$,, where I_i, I_{0i} are integral intensities of i-diffraction peak for a film and the etalon, N is a number of lines registered by the XRD technique. The orientation factor was found from the expression $f = \sqrt{(1/N)[\sum_{i=1}^{N}(P_i - 1)^2]}$. The $Zn_{1-x}Mn_xTe$ powder has served as an etalon of the sample without texture.

The lattice constant of the charge used for evaporating films and the lattice constant of $Zn_{1-x}Mn_xTe$ layers obtained at various condensation modes were determined according to the position of the $K_{\alpha 1}$ component in all the most intensive lines of experimental XRD patterns. The expression $a=\lambda(h^2+k^2+l^2)^{1/2}/(2\sin\theta)$, was applied for calculating the lattice constant of cubic phase, here λ is a wavelength of the X-ray radiation, *h, k, l* are Miller indices [3 and refs. therein]. Further in order to obtain the most accurate values of the lattice constant we will use the extrapolation Nelson-Raleigh method [3 and refs. therein]. The experimental data were rebuilt in coordinates $a(c)$–$1/2\cos^2\theta(1/\sin(\theta)+1/\theta)$. The minimal square technique was then applied for linear approximation of these functions. The precision of the method is 0.001%. The K_α line resolution was done by the Rachinger method using the software package DIFWIN.

The element analysis of the films was carried out by using characteristic X-ray radiation induced by the proton beam [3 and refs. therein]. The investigations were made by means of the electrostatic accelerator “Sokil” with the proton beam energy up to 2 MeV (IAPh of NAS Ukraine, Sumy) [3 and refs. therein]. The collective spectra from some regions of the sample surfaces were registered (PIXE), and then the point-to-point scanning of these regions was done by using micro-beam (μ-PIXE). The typical region size was about 200×200 μm. The cross-section of the probe is 4×4 μm^2, the charge Q = 4×10^{-10} C/pixel, the scan region was about 50×50 pixel, the scanning step is 4 μm, the proton energy is E_p = 1.5 MeV. Under «pixel» one means a stationary position of the probe at discrete scanning. These studies have resulted in a map of the distribution of the doping element (Mn) on the surface area and the

element composition of the condensates in some regions of the films. The working-out of the PIXE spectra was carried out by using the program GUPIX.

The experimental studies demonstrated that the growth of $Zn_{1-x}Mn_xTe$ films was analogous to the condensates' growth of other chalcogenides [3 and refs. therein]. These films have a grain size D = (0.50-1.12) μm at the thickness l ~ (2-4) μm, and the grain size has increased as the substrate temperature has elevated. The electron microscopy images of the surface and cross-section of $Zn_{1-x}Mn_xTe$ films prepared under various substrate temperatures are shown in Figure 8. The analysis demonstrated that the calculated D values were somewhat lower than those in ZnTe films fabricated at the same conditions [3 and refs. therein].

The X-ray diffraction patterns from $Zn_{1-x}Mn_xTe$ thin films deposited at various substrate temperatures are plotted in Figure 9. The single phase structure of the stable cubic modification (ZB) is a typical structure for these condensates. As a rule, the XRD patterns gave revealed the reflections from the planes (111), (200), (220), (311), (222), (400), (420), (311), and (422) of the cubic phase. The most intensive peaks were the peaks (111). This fact points out the existence of the growth texture with an axis normal to the plane [111]. The XRD pattern from the film deposited at T_s = 150 ^{0}C shows a line of low intensity (0.7% from the intensity of the line (111)) at the angle 73.49^0, which may be interpreted as the reflection from the crystallographic (444) Mn plane. The additional lines were not observed in other XRD patterns.

Our conclusion about the existence of the [111] growth texture in the films is confirmed by the calculation by the method of reverse pole figures (Figure 10a). The pole density has a maximum value for crystallographic planes (111), (222). The texture [111] is a typical one for A_2B_6 thin films prepared by vacuum evaporation [3 and refs. therein], earlier we have revealed this texture in ZnTe films deposited by the same technology [3 and refs. therein].

Figure 10b shows how the orientation factor f depends on the substrate temperature for $Zn_{1-x}Mn_xTe$ films. As is seen the orientation factor increases with the substrate temperature elevation from f = 0.56 (T_s = 150 ^{0}C) up to 2.19 (T_s = 550 ^{0}C). Thus, the high-temperature condensates have a good quality texture. The experimental data obtained by the authors earlier [3 and refs. therein] for ZnTe films are presented

for a comparison. Obviously, the additional Mn doping does not sufficiently change the quality of the film texture.

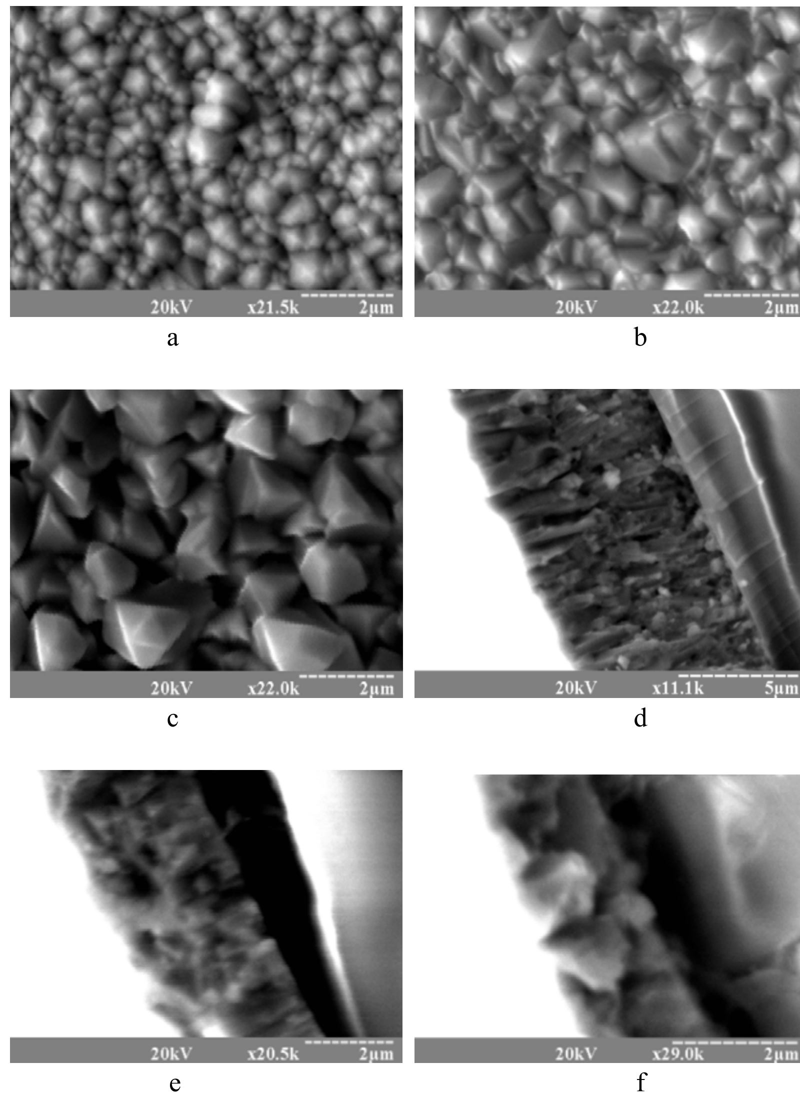

Figure 8. Microphotographs of the surface (a-c) and cross-section of the $Zn_{1-x}Mn_xTe$ films (d-f) deposited under the substrate temperature T_s, ^{0}C: 150 (a, d), 350 (b, e) and 550 (c, f), respectively.

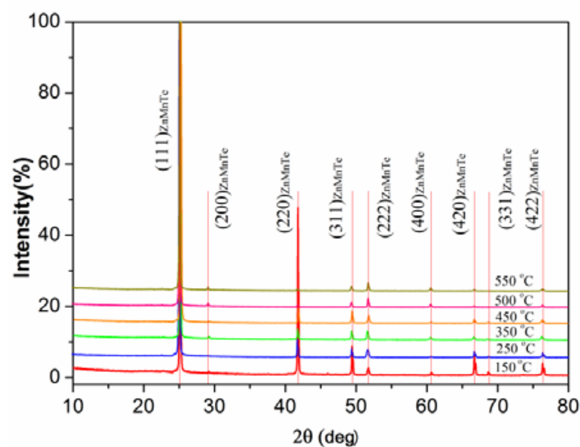

Figure 9. X-ray diffraction patterns of the $Zn_{1-x}Mn_xTe$ films fabricated under various physical technological condensation modes.

Figure 11 plots the lattice constant dependence of the solid solution $Zn_{1-x}Mn_xTe$ on the condensation temperature. The function a-T_s for ZnTe films prepared by the authors earlier [3 and refs. therein] is shown for the comparison. It is found out that the experimental values of the lattice constant for the solid solution $Zn_{1-x}Mn_xTe$ (a = 0.60998-0.61043 nm) are lesser than those for the films ZnTe grown under the same conditions (a = 0.60890-0.61165 nm). It may be caused by the replacement of Zn atoms with Mn atoms in the crystal structure of the material. As is known, the Mn atoms have a smaller atomic radius [3 and refs. therein]. As is demonstrated by Figure 4 the dependence of the lattice constant on the condensation temperature is complex as a possible consequence of the composition change. As the substrate temperature increases from T_s = 150 ^{0}C to T_s = 450 ^{0}C the lattice constant a of the material is somewhat elevated (from 0.60998 to 0.61043 nm), then its value stabilizes at a = 0.61015 nm.

PIXE method was applied for some surface areas of the films $Zn_{1-x}Mn_xTe$ to determine the manganese concentration. It is revealed that the manganese content in the samples is estimated to be (1.61-3.04) ат. % and it depends on the temperature of the substrate and evaporator. Scanning the samples' surfaces by the proton beam (μ-PIXE) resulted in a homogeneous area distribution of the Mn atoms. The general PIXE spectra and Mn area distribution maps are plotted in Figures 12 and 13.

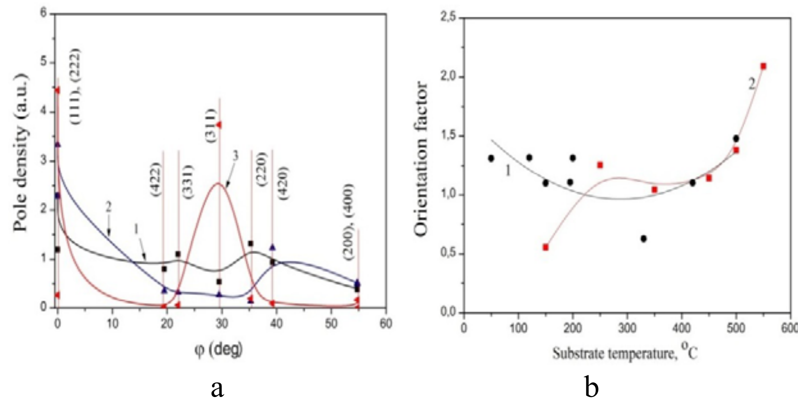

Figure 10. Dependence of the pole density P_i on the angle φ between the texture axis and the normal vector to the reflection plane for $Zn_{1-x}Mn_xTe$ films prepared at T_s , ^{0}C: 150 (1), 350 (2), 550 (3)(*a*) and dependence of the orientation factor f on the substrate temperature for the films ZnTe (1) and $Zn_{1-x}Mn_xTe$ (2) (b).

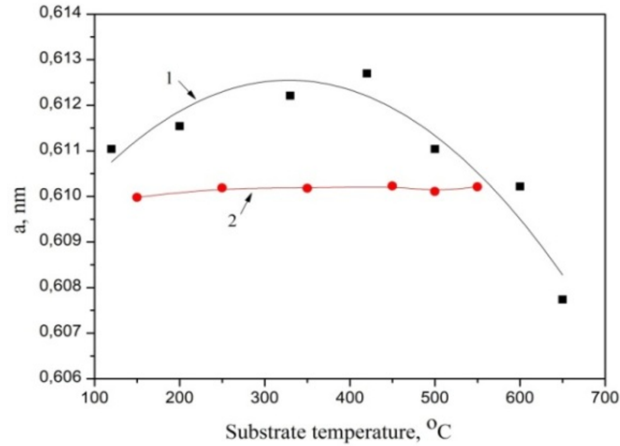

Figure 11. Dependence of the lattice constant on the substrate temperature T_s for films ZnTe (1) and $Zn_{1-x}Mn_xTe$ (2).

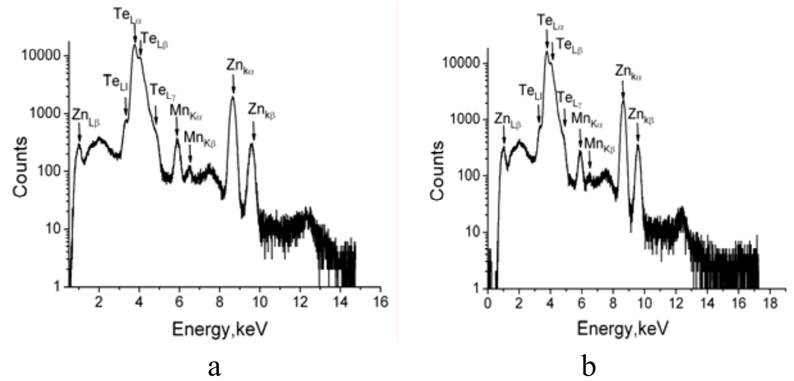

Figure 12. The total PIXE spectrum from the $Zn_{1-x}Mn_xTe$ films under irradiation by the proton beam with energy 1.5 MeV (on the area 200×200 μm). The substrate temperature T_s, ^{0}C: 350 (a), 450 (b).

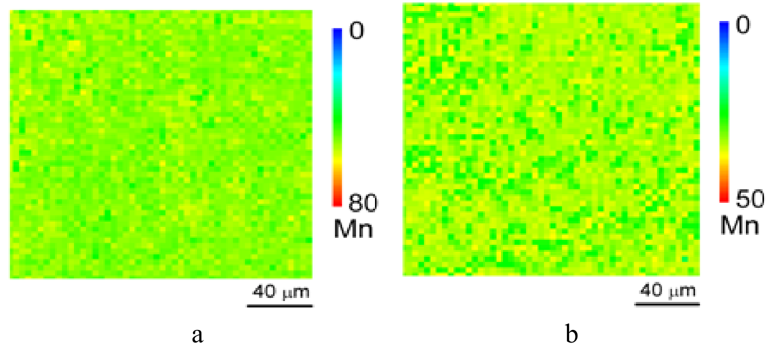

Figure 13. Maps of Mn distribution on the sample surface (the surface area is 200×200 μm). (Scan area is 50×50 pixels). The substrate temperature T_s, ^{0}C: 350 (a), 450 (b).

Table 2 shows results on study of the element composition of the investigated films. As is obvious, under the elevation of the substrate temperature from 350 ^{0}C to 550 ^{0}C the Mn concentration in the condensates lowers from 3.04% down to ~1.7%. Besides that the films are characterized by Te predominance (C_{Zn}/C_{Te} = 0.70-0.87).

The manganese precipitates in the films were not observed neither by electronography nor X-ray studies, the lattice constant of the material has decreased in comparison with that of the doped compound; these

observations have led us to conclusion that the Mn atoms are likely built-in the crystal structure of ZnTe forming the corresponding solid solution.

Table 2. The element concentration of the $Zn_{1-x}Mn_xTe$ films

T_s, ^{0}C	T_e, ^{0}C	wt.% Zn	wt.% Mn	wt. %Te	at. % Zn	at.% Mn	at.% Te	C_{Zn}/C_{Te}	C_{Zn+Mn}/C_{Te}
350	800	28.9	1.7	69.4	43.5	3.0	53.5	0.81	0.87
450	800	30.6	1.1	68.4	45.7	1.9	52.4	0.87	0.91
550 (area 1)	800	26.2	1.0	72.8	40.5	1.9	57.6	0.70	0.74
550 (area 2)	800	26.3	0.9	72.8	40.7	1.6	57.7	0.71	0.73

Summarizing the results, we should note the following features of the surface morphology and structural peculiarities of $Zn_{1-x}Mn_xTe$ films prepared by CSVS technique under various technological modes of condensation:

1. It is found out that $Zn_{1-x}Mn_xTe$ condensates have the grain size D = 0.50-1.12 μm at thickness l ~ 2-4 μm, the value D has increased under the substrate temperature elevation.
2. The stable single cubic phase ZB structure is revealed as a typical one for the investigated films. Calculations carried out by the method of reverse pole figures have allowed to reveal the axial growth texture [111] in thin layers. The perfectness of this texture has improved as the condensation temperature has been increased.
3. It is shown that the experimental values of the lattice constant for $Zn_{1-x}Mn_xTe$ (a = 0.60998-0.61043 nm) are lesser than those for ZnTe films (a = 0.60890-0.61165 nm) grown under the same conditions.
4. Using PIXE method the manganese concentration in $Zn_{1-x}Mn_xTe$ films was determined: (1.61-3.04) at. %, and it depended on the substrate and evaporator temperature. Scanning the sample surface by the proton beam (μ-PIXE) showed that the manganese is uniformly distributed on the sample surface with formation of the solid solution.

Chapter 3

LED SULFIDE AND MERCURY-CADMIUM-ZINK-TELLURIDE THIN FILM-BASED HETEROSTRUCTURES [4]

In this chapter we consider some interesting experimental results given by the examination of led sulfide and ZnCdHgTe thin film-based heterostructures.

CONSTRUCTION OF ENERGY BAND DIAGRAM FOR A HETEROSTRUCTURE N-ZNSE-P-PBS

The energy band diagram of any heterostructure is its "visit card" for prospective device applications. Let us illustrate the procedure of the band diagram construction using experimental data obtained from examinations of anisotype heterojunctions *p-PbS-n-ZnSe* [4 and refs. therein].

The investigated *p-PbS/n-ZnSe* heterostructures were fabricated by the molecular beam epitaxy (MBE) of lead sulfide films of 1-3 μm thickness on monocrystalline zinc selenide wafers at the substrate temperature T_s = 540 K and pressure in the vacuum chamber 10^{-9} Torr

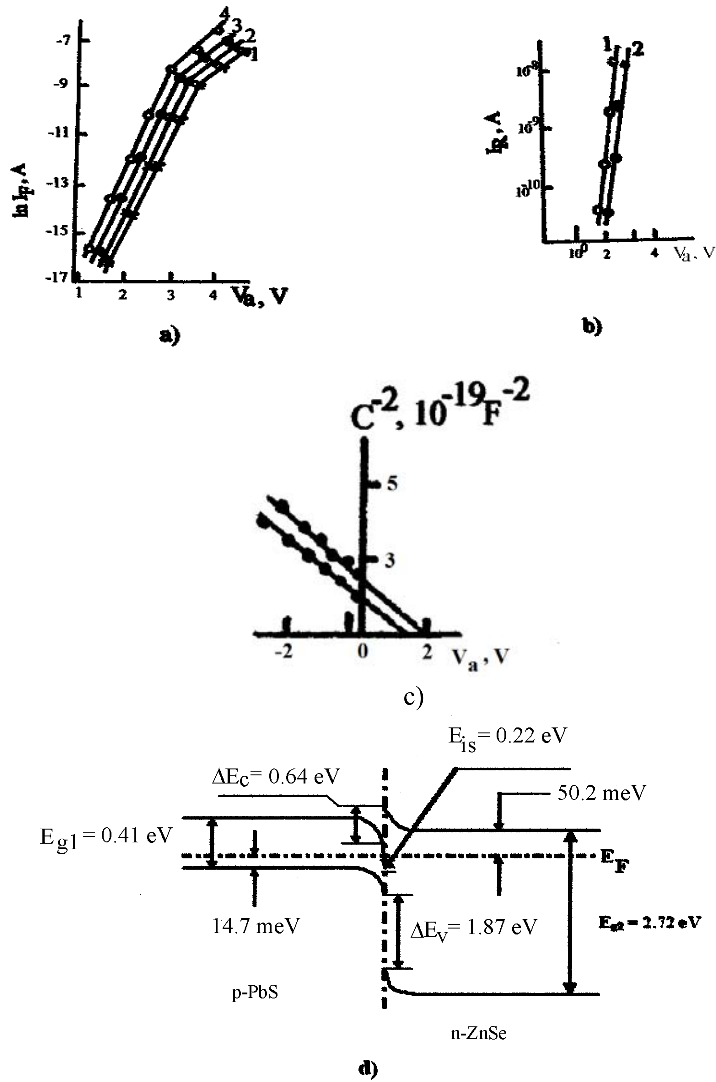

Figure 14. Electrical characteristics of the abrupt heterojunction *p-Pbs-n-ZnSe*: a) forward IVCs at T, K: 1 – 77, 2 – 125, 3 – 205, 4 – 293; b) reverse IVCs at *T*, K: 1 – 77, 2 – 293; c) CVC at *T*, K: 1 – 77, 2 – 293; the frequency of the test signal *f* = 1 MHz; d) equilibrium energy band diagram of the examined heterojunction (not in scale), T = 293 K ([4 and refs. therein]).

As Figure 14 shows, the heterostructures fabricated are abrupt heterojunctions characterized by exponential current-voltage dependencies ($j \sim exp(eV_a/nk_BT)$ with the ideality factor $n = 3.1 – 8.0$) and linear $C^{-2} = f(V_a)$ capacitance-voltage functions in the wide range of applied bias ($-4.0 \le V_a \le 4.0$ V) and temperatures ($T = 77 – 293$ K).

Numerical simulation of the experimental results gave the following expressions for measured electrical characteristics with account of the interface states:

$$j_f = 0.25Aev_{th}N_DX\exp[-(\Delta E_c+E_{is})/2k_BT]\exp(eV_a/nk_BT), \qquad (1)$$

$$j_r = j_sXV_a(E_{F1} + E_{F2} - eV_a), \qquad (2)$$

where A is the heterojunction area, v_{th} and N_1 are the carrier thermal velocity and concentration in the substrate ($ZnSe$), X is the barrier tunneling transparency coefficient, j_s the saturation current density, and E_{F1} and E_{F2} are quasi-Fermi levels for majority carriers in the heterocomponents. The interface states energy level E_{is} is found from C-V-measurements to be equal approximately 0.22 eV.

Experimental capacitance-voltage measurements allowed to calculate the following important parameters of this heterojunction: i) the full charge of the interface states (IS) $Q_{is} = 2.1 \cdot 10^{-5}$ $Cl \cdot cm^{-2}$; ii) the IS density $N_{ss} = 1.3 \times 10^{13}$ $eV^{-1}cm^{-2}$; iii) the width of the space charge region $W = 210$ nm; iv) the capacity of the space charge region $C_{ss} = 1.1 \times 10^{-8}$ $F \cdot cm^{-2}$.

The calculation of the energy band diagram for a nonideal abrupt heterojunction requires more precisely account of electronic properties of the heterocomponents [4 and Refs therein]. In our case the valence band discontinuity ΔE_v is to be calculated as follows:

$$\Delta E_v = (\varepsilon_p)^{B!} - (\varepsilon_p)^{B2} + \sum_{i=1}^{2} (-1)^i[\{[(\varepsilon_p)^{Ai} - (\varepsilon_p)^{Bi}]^2 \cdot 0.25 + (1.06h^2/\pi^2 a_1^2\}^{1/2} - \{(\varepsilon_p)^{Ai} - (\varepsilon_p)^{Bi}\}/2 \pm (\varepsilon_0 a_1)^{-1}\Sigma q_i^* \pm E_{is} \pm (k_BT/e)\ln[v_{th}(\tau/D)^{1/2}\delta\Delta a/a^3], \qquad (3)$$

where $(\varepsilon_p)^{Ai}$, $(\varepsilon_p)^{Bi}$ are atomic orbital energies of Zn, Se and S, q^* are their effective charges, D, τ, σ are the diffusion coefficient, carrier lifetime

and recombination cross-section in the wide-gap substrate (Tables 3, 4), $\Delta a = |a_1 - a_2|$, $a = 0.5(a_1 + a_2)$, a_i $(I = 1, 2)$ are the lattice constants of PbS and ZnSe. The conduction band discontinuity is expressed as $\Delta E_c = E_{g1} - E_{g2} - \Delta E_v$. The energy band diagram of the nonideal abrupt heterojunction *p-PbS/n-ZnSe* is plotted in Figure 14, d.

Table 3. PbS and ZnSe parameters used for the calculation of the energy band diagram

Parameter	ZnSe	PbS
Lattice constant a, nm	0.569	0.594
Band gap E_g, eV	2.72	0.41
Thermodynamic work function		
φ, eV	4.84	3.80
m_n*, units of m_0	0.17	0.105
m_p*, units of m_0	0.60	0.105
D, $cm^2 \cdot s^{-1}$	15.0	
τ, s	$\sim 10^{-5}$	
σ, cm^2	$\sim 10^{18}$	
$N_D \cdot cm^{-3}$	$(0.3 - 2.8) \cdot 10^{17}$	

Note: m_0 is the free electron mass.

Table 4. Atomic orbital energies and effective charges for the elements of the Groups II and VI of the Periodical system

Element	$-\varepsilon_p$, eV	q*, in units of e
Zn	3.38	0.79
Se	9.53	1.30
S	10.27	1.40

ELECTRON SYSTEM PROPERTIES OF SEMICONDUCTOR STRUCTURES BASED ON PBS AND ZNCDHGTE THIN FILMS

Today, the operation of almost any semiconducting device relies on the use of interfaces. Although semiconducting technology started to

utilize interfaces more than 50 years ago, an analogous development is taking off today. Advances in the heteroepitaxy of complex compounds now provide the possibility of fabricating interfaces with atomic precision. Such interfaces can generate electron systems that nature does not produce in the bulk. The electrons interact and order at the interfaces in unique ways, so that, for example, field-effect transistors using phase transitions, novel types of quantum Hall systems, and unique superconductors can be obtained. Wellcontrolled interfaces based on different materials have been fabricated and are being used for a possible new generation of electronic devices. The defining property of interfaces - the simple fact that they connect different materials - creates new possibilities for generating novel electronic phases [4 and refs. therein].

The realization of two-dimensional electron gases (2DEGs) in semiconductor interfaces based on Si or on III–V compounds has led to tremendous developments and successes in both understanding fundamental physics and developing new devices. As a fruit of efforts that started in the 1960s, 2DEGs with typical carrier densities ranging from 10^{10} cm^{-2} to 10^{12} cm^{-2} can be generated at a single heterojunction (interface between two different materials) or in doped heterostructures that form superlattices (periodic arrays of interfaces).

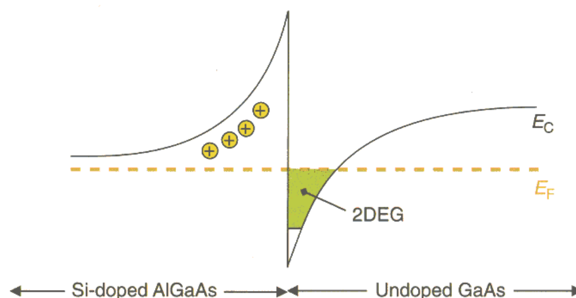

Figure 15. Band diagram showing the formation of a two-dimensional electron gas (2DEG) at a Si-doped *AlGaAs–GaAs* heterojunction (4 and refs. therein).

As shown in Figure 15 for a single heterojunction, electron gases are formed in quantum well structures with typical widths on the order of 10 nm. The potential well perpendicular to the interface causes quantization of the electronic states. Along the plane, the carriers can move with a

high mobility. Whereas these mobilities reached only $\sim 10^4 cm^2 V^{-1} s^{-1}$ in early III–V heterostructures, their top values now exceed $10^7 cm^2 V^{-1} s^{-1}$ at low temperatures. High mobilities and long mean free paths are essential to generate quantized Hall resistances according to the integer or fractional quantum Hall effects (QHEs) or to use the electron gases, for example, in high-electron-mobility transistors (HEMTs).

The concept invented to attain the high mobility is to spatially separate the doping layer from the mobile carriers and thereby suppress scattering at the ionized dopants. The spatial separation of the conduction layer and the charge-generation layer is a principle that also offers great potential for these heterostructures [4 and refs. therein].

Consider electronic properties of the photosensitive *n-PbS/n-ZnSe* heterostructures fabricated by the molecular beam epitaxy (MBE) of lead sulfide films of 1-3 μm thickness onto monocrystalline zinc selenide wafers at the substrate temperature T_s = 540 K and pressure in the vacuum chamber 10^{-9} Torr [4 and refs. therein]. The carrier concentration and the Hall mobility were $4.5 \cdot 10^{17}$ cm^{-3} and 10^4 $cm^2V^{-1}s^{-1}$, respectively. *ZnCdHgTe* layers were grown by the liquid phase epitaxy (LPE) and served as substrates for $Pb/p\text{-}Zn_{0.17}Cd_{0.07}Hg_{0.76}Te$ Schottky barrier fabrication. The as-grown LPR-layers had the hole concentration $3.0 \cdot 10^{16}$ cm^{-3} and Hall mobility 600 $cm^2V^{-1}s^{-1}$ at 77 K [4 and refs. therein].

The model mentioned above is applicable for abrupt heterostructures, so one should investigate IVC and CVC for examination of their abruption (Figure 16).

The most interesting point in semiconductor heterostructures investigations is the construction of energy band diagrams. As is shown (Figure 16, a), the capacitance-voltage dependence is a straight line in coordinates $C^{-2} = f(V_a)$ and the current-voltage characteristics are described by the equations (1 - 2).

The energy band diagrams were constructed according to the triangle potential well approximation [4 and Refs. therein]. The energy levels E_0 and E_1 (Figure 16 b, c) are appeared in the narrow interlayer range at the heterointerface with the electron state concentration approximately 10^{11} – 10^{12} cm^{-2} (calculated by experimental capacitance-voltage measurements).

Both heterostructures were photosensitive in the wavelength ranges 2 – 5 μm and 2 – 11 μm, respectively. The investigations of the carrier

lifetime carried out for the Schottky contacts *Pb/p-ZnCdHgTe* (Figure 16, d) showed values approximately up to 100 ms.

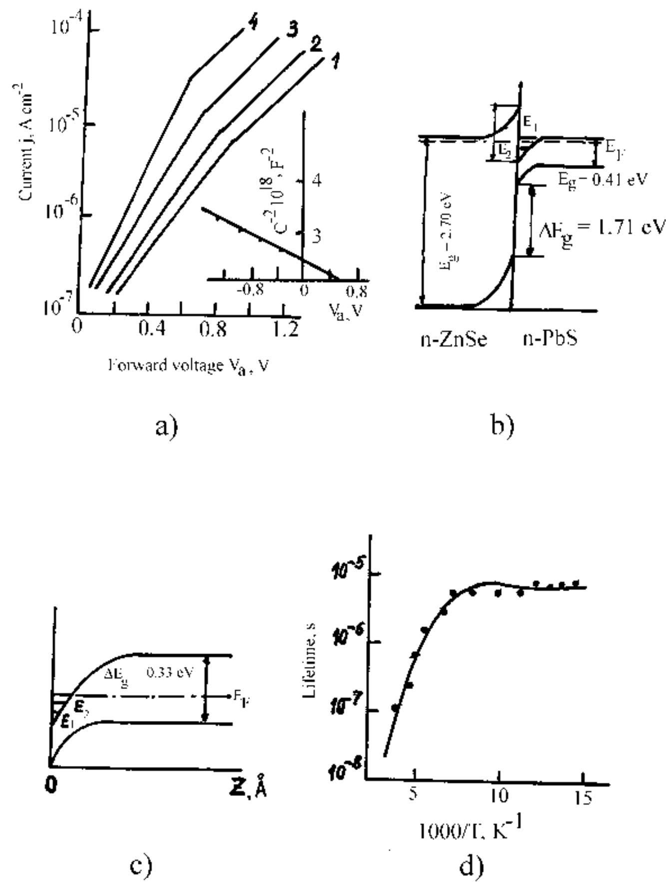

Figure 16. a) Current-voltage and capacitance-voltage (insert, T = 77 K) characteristics of *n-PbS/n-ZnSe* heterostructure; *T,* K: 1 – 77, 2 – 180, 3 – 235, 4 – 293; b) energy band diagram of the n-PbS/n-ZnSe heterostructure, T = 77 K; $E_0 = 3.76\ meV$, $E_1 = 4.12\ meV$; c) energy band diagram of the Schottky contact *Pb/p-ZnCdHgTe,* T = 77 K; d) the carrier lifetime temperature dependence for the Schottky contact *Pb/p-ZnCdHgTe* ([4 and refs. therein]).

Minority carrier lifetime was measured by the photoconductivity decay technique. Experimental data were compared with that obtained from examinations using band-to-band radiative and two Auger

recombination mechanisms. These results proved that the concentration of recombination centers in the epitaxial *ZnCdHgTe* layers is almost negligible.

QUASI-TWO-DIMENSIONAL ELECTRON LAYER IN ZNCDGTE- AND PBS-BASED HETEROSTRUCTURES

How to calculate the energy spectra of the charge carriers located in quasi-walls depicted in the band diagrams (Figures 14-16)? Now we are going toward the more detailed numerical procedure.

As is known, narrow-gap II-VI/IV-VI semiconducting materials are compounds of choice for studies on low-dimensional electron systems. This is owing to their small conduction band effective mass which leads to comparatively large energy spacing at feasible dimensions. Two-dimensional electron gas (2DEG) may be produce by a metal-insulator-semiconductor (MIS) structure, by a MBE-grown heterostructure or a superlattice [4 and Refs. therein]. The effect is sensitive to interface properties as well as to the epitaxial growth conditions. It is of interest for characterization of inversion lyers, heterostructures and superlattices. Now we present the first demonstration of quasi-two-dimensional electron systems in *ZnCdHgTe* and *PbS* epitaxial layers where the 2DEG is formed in the inversion layers of a Schottky barrier and a *p-PbS/n-ZnSe* heterostructure, respectively.

High quality *p*-type *ZnCdHgTe* epilayers grown by a modified LPE method were used for Schottky device fabrication. We needed to obtain a metal-semiconductor (MS) structure with the lead evaporated onto the $Zn_{0.17}Cd_{0.07}Hg_{0.76}Te$ substrate (E_g = 300 meV at 77 K). The as-grown quaternary compound exhibited a hole concentration of $5x10^{16}$ cm^{-3} with a Hall mobility of about 400 $cm^2V^{-1}s^{-1}$ at 77 K. Underneath the narrow region between the metl film and the *ZnCdHgTe* epilyer mobile inversion electrons were induced by a gate voltage.

p-PbS films were grown in a conventional MBE system. The growth was monitored with reflection high-energy electron diffraction (RHEED). Growth rates were ranged from 0.05 to 0.1 μm h^{-1} and the substrate temperature was about 540 K. Monocrystallinr *n*-type (110) *ZnSe* 1-3 mm thick was used as a substrate. The (110) orientation was chosen because higher quality *PbS* films may be grown on this surface.

The determined carrier concentration was equal to about $4.5x10^{17}$ cm^{-1} and Hall mobility was 8000 $cm^{-2}V^{-1}s^{-1}$ at 77 K. Surface morphologies were examined by several techniques, including X-ray double diffractometry, transmission electron microscopy, and Auger spectroscopy. The film thickness was measured with an interference microscope.

The results of surface investigation by means of interference microscopy showed that *PbS* films exhibited the tessellated structure which forms potential relief responsible for the electron system behaviour in the heterojunction region [4 and refs. therein].

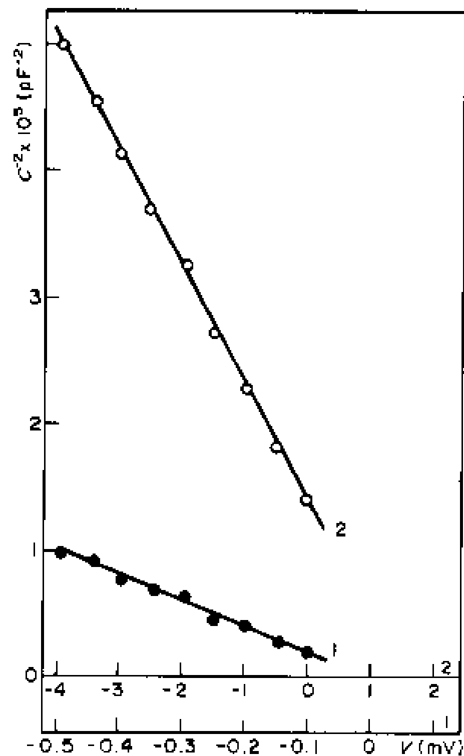

Figure 17a. Capacitance-voltage characteristics of *Pb/p-ZnCdHgTe* (curve 1) and *p-PbS/n-ZnSe* (curve 2) heterostructures at T = 77 K, test signal frequency *f* = 1 MHz ([4 and refs. therein]).

The CVCs of the *Pb/ZnCdHgTe* and *p-PbS/n-ZnSe* heterostructures (Figure 17a) indicate that the formed heterojunctions are abrupt. We estimated the main electrophysical parameters [4 and refs. therein]: full interface electron states charge Q_{is}, interface electron state density N_{is}, and space charge region capacitance C_{is} (Table 5). Consequently, we assumed that the electron system may be studied using the triangle potential well approximation. The main parameters were calculated according to the model [4 and refs. therein]:

$$E = (h^2/2m^*)^{1/3}[1.5eF(i + 3/4)]^{2/3}, \quad (4a)$$

$$F = (N_{is} + N_A l_1)e/4\pi\varepsilon_0\varepsilon_1, \quad (4b)$$

$$V_1 = e^2 N_A (l_1)^2/8\pi\varepsilon_0\varepsilon_1 + eN_{is}E_i/6\pi\varepsilon_0\varepsilon_1 F, \quad (4c)$$

$$V_2 = e^2 N_D (l_2)^2/8\pi\varepsilon_0\varepsilon_2, \quad (4d)$$

where E_i stands for the triangle well energy levels, F and m^* are the electric field and the free carriers effective mass in the narrow-gap semiconductor, l_1 is the potential well width in the narrow-gap semiconductor, l_2 is an independent variable, and V_1 and V_2 are the conduction band bending (Table 6).

We assumed $l_1 = 0.5$ μm and $l_2 = 0.04$ μm as parameters for these calculations.

Table 5. The main results concerning the electron system energy levels E_i (meV) and the conduction band bendings V_1 and V_2 (meV) obtained by the calculations relevant to *Pb/p-ZnCdHgTe* (upper row)) and *p-PbS/n-ZnSe* (lower row) heterostructures [4 and refs. therein]

E_1	E_2	E_3	E_{10}	E_{20}	E_{30}	V_1	V_2
1.15	1.60	1.91	17.1	26.5	34.5	100	-
1.25	1.72	2.10	30.9	35.5	62.3	490	150

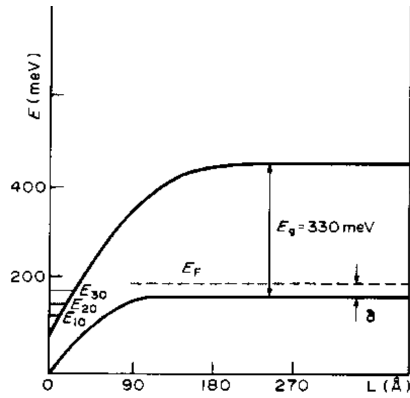

Figure 17b. Energy band diagram of the *Pb/p-ZnCdHgTe* MS-structure. Here, the conduction band bending is equal to 100 meV, E_g = 330 meV is the bandgap value, δ = 2.09 meV is the bulk Fermi level position and is calculated according to the classical semiconductor theory, E_{10}, E_{20}, and E_{30} are the electron system energy levels which are formed in the heterojunction region (After [4 and refs. therein]).

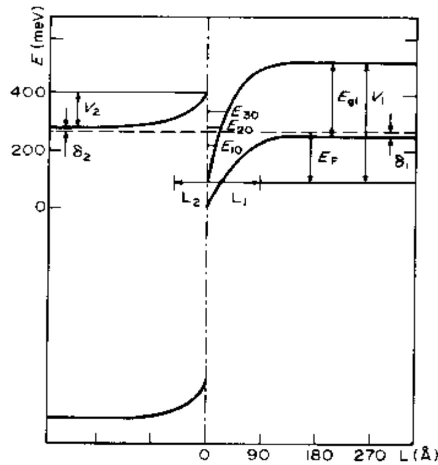

Figure 17 c. Energy band diagram of the *p-PbS/n-ZnSe* heterostructure. Here, V_1 = 490 meV and V_2 = 150 meV are conduction band bendings in the narrow-gap and wide gap heterojunction constituents, respectively, E_g = 310 meV is the PbS bandgap value, δ = 10 meV is the bulk Fermi level position ahd is calculated according to the classical semiconductor theory, E_{10}, E_{20}, and E_{30} are electron system energy levels which are formed in the heterojunction region (After [4 and refs. therein]).

The resulting band diagrams of the heterostructures are shown in Figure 17b,c. as a consequence the investigated electron systems have the quasi-discrete energy spectra because energy level shifts are smaller than the thermal energy k_BT. Thus, the main quantity of electrons is localized at the interface of the structures with a thickness Z of about 0.30 nm. The parameter Z was calculated from the following equation [4 and refs. therein]:

$$Z = \int_0^{\infty} z\psi_i^2(z)dz = 2E_i/3eF, \tag{4e}$$

where $\psi_i(z)$ is an electron wave function.

Current-Voltage Characteristics of Heterostructures Based on Narrow-Gap Semiconductor ZnCdHgTe

The numerical modeling is seemed to be a helpful tool suitable for a prediction of different features of structures and processes under study.

The semiconductor solid solution *ZnCdHgTe* (ZCMT) has been proposed as a new perspective material for different applications for optoelectronic devices operating in the wide temperature range (77-290 K) and wave-length region 4-12 μm. To avoid the sufficient mismatch of contacting materials lattice parameters, ZCMT epilayers were manufactured on *CdTe* and *ZnCdTe* monocrystalline (111) substrates by the modified LPE technology [4 and refs. therein]. However, the structural studies performed after the films growth have demonstrated the mismatch of the layer and the substrate lattice parameters about 0.32-1.29% which in turn causes mismatch deformation generating the interface states band forming at the interface plane (Figure 18a). These states act as recombination centers and significantly change the band-gap diagram of the heterojunction and sufficiently affect the current transfer processes. The I-V and C-V investigations performed for the monitoring of electrical properties of the p-isotype heterostructures $Zn_xCd_yHg_{1-x-y}Te/CdTe$ $(0<x\leq 0.20,\ 0.07\leq y\leq 0.0.18)$ have demonstrated the current-voltage and capacitance-voltage dependencies (Figure 18,a) similar to

ones of abrupt heterojunctions with a sufficient effect of the interface electron states localized in the space charge region.

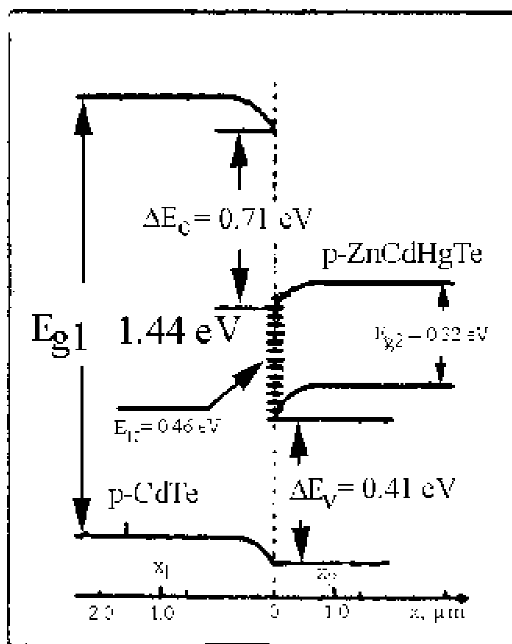

Figure 18a. Equilibrium energy band diagram (T = 300 K) of the examined heterostructure (After [4 and refs. therein]).

In particular, the ideality factor n of both forward and reverse sections of the current-voltage characteristics is more larger than 1 which indicates the dominant trap-assisted tunneling process.

Electrophysical studies have shown that the as-grown epifilms of 8-25 μm thickness were characterized by both *p*- and *n*-type of conductivity. Surface examinations have revealed the inhomogeneous microrelief of .the epitaxial layer surface with the typical element size of about 0.1 μm. The electrical area of the examined samples was estimated to be 4-8 mm^2. The measurements made at 290 K have exhibited the two-section current-voltage dependence and a straight C^{-2} $=f(V)$ characteristic (Figure 18b, c).

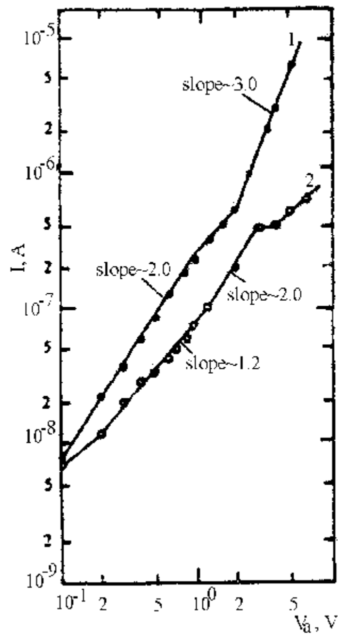

Figure (18b). Experimental room-temperature current-voltage characteristics of the heterostructure under study: 1 – forward, 2 – reverse.

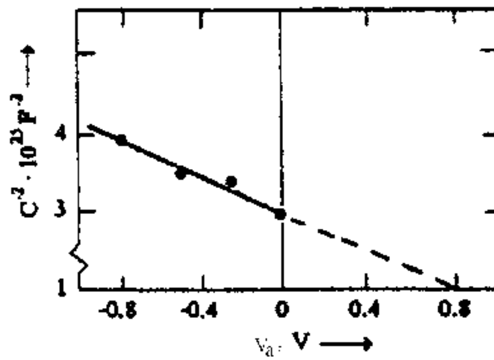

Figure (18c). Experimental room-temperature capacitance-voltage characteristic of the *p-CdTe/p-ZnCdHgTe* heterojunction, the test signal frequency $f = 1$ kHz (After[4 and refs. therein]).

In order to clarify what represents the obtained heterostructure from the point of view of energy parameters the band diagram has been constructed according the theoretical model [4 and refs. therein] developed for heterojunctions with close dielectric constants of contacting materials (Table 6). The main equations for the energy-band diagram parameters calculation are:

$$\Delta E_c=\Delta E_v+k_BT\log(N_{cA}N_{vB}/N_{cB}N_{vA})-(\Delta E_{ex}+\Delta E_{hxc})-2(\Delta E_{im}+\Delta E_b), \quad (5)$$

$$\Delta E_v+\Delta E_c=\Delta E_g. \quad (6)$$

Here ΔE_m (m = c, v, g) are the conduction band discontinuity, valence band discontinuity and the difference between the band-gaps of the contacting materials, respectively, N_c, N_v stand for the effective state densities in *c*- and *v*-bands of both materials (A-index relates to *CdTe*, B-index relates to *ZnCdHgTe*) The third term in (5) accounts the effective electron-hole exchange-correlation energy:

$$E_{xc}\approx-2.5\cdot10^{-7}[1+0.7734y\log(1+y^{-1})N^{-1/3}\varepsilon^{-1}, \quad (7)$$

$$y\approx5.6\cdot10^{8}[m^*/\varepsilon)N^{-1/3}, \quad (8)$$

where N and m^* denote the effective states density and effective mass of electrons or holes in both materials, the final term takes care of the image forces and interface dipole bond energy due to interaction of dangling bonds:

$$E_{im}(A)=(\varepsilon_B-\varepsilon_A)e^2/\pi\varepsilon_0(\varepsilon_A+\varepsilon_B)\varepsilon_A d_B, \quad (9a)$$

$$E_{im}(B)=(\varepsilon_B-\varepsilon_A)e^2/\pi\varepsilon_0(\varepsilon_B+\varepsilon_A)\varepsilon_B d_A, \quad (9b)$$

$$E_b(A) = e^2/4\pi\varepsilon_0\varepsilon_A d_B, \quad (9c)$$

$$E_b(B) = e^2/4\pi\varepsilon_0\varepsilon_B d_A, \quad (9d)$$

where $d=(3)^{1/2}a$, a is a lattice parameter of the corresponding material. The energy spectrum of the interface electron states had been calculated according to the method described in [4 and refs. therein]. The following numerical simulation procedure had been performed with taking into account the values of the calculated band-gap diagram.

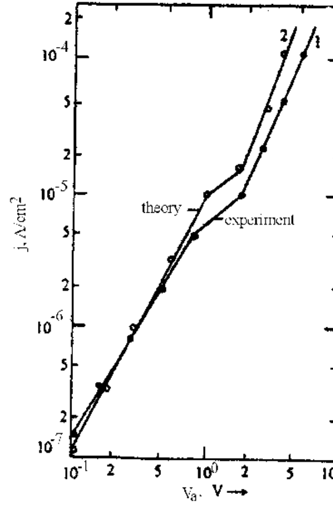

Figure (18d). Experimental (1) and computed (2) room-temperature current-voltage characteristics of the investigated heterostructure. In the region of the applied bias $V_a > 1.1$ V the calculated current values are slightly larger than experimental ones due to the effect of the potential relief of the *ZnCdHgTe* epitaxial layer (After [4 and refs. therein]).

As we have mentioned above, the structural studies performed for as-grown *ZnCdHgTe* epifilm have exhibited quasi-3D symmetrical Gaussian distribution of the surface inhomogeneities characterized by the typical elemental size approximately 0.1 μm, in other words, this value is larger than Debye screening length (L_D is about 0.07 μm). Accounting carriers generation in the space charge region and appearance of surface electron states band E_{is} (see Figure 19a) the expression for the total tunneling current can be written as follows:

$$j \sim \int \exp[-4(m^*)^{1/2}(E_{is})^{3/2}/3e\hbar F]\exp[-(E-E_{is})/\Delta^2]dE, \quad (10)$$

where m^* stands for *ZnCdHgTe* hole effective mass, F is an electric field strain in the heterojunction region, Δ is a tunneling parameter caused by the surface relief of the epifilm, $\Delta << E_g$ (here E_g denotes the forbidden gap of *ZnCdHgTe*) [4 and refs. therein]. Thus, noting the experimental current as

$$j=eAN(\mu_h kT/\tau e)^{1/2} j_s \exp[-(4(m^*)^{1/2}(E_{ss})^{3/2}/3e\hbar F)+(m^* E_{ss}\Delta^2/e^2\hbar^2 F^2)], \quad (11)$$

(here μ_h and τ are holes mobility and recombination life-time in *ZnCdHgTe*, j_s is a saturation current determined from the experimental data) we calculated the value of Δ: $\Delta \approx 52$ meV. On the other hand, the current- voltage dependencies observed experimentally appear not only as the functions of the applied voltage but they are also determined by the value of band-gap or conductance band discontinuity and the energy level of the surface electron states at the interface. So the principal expression for the numerical modeling of the experimental I-V characteristics can be written as follows:

$$j \sim f(\Delta E_v) f(E_{ss}) f(M.P.) V^m, \quad (12)$$

where M.P. stand for *CdTe* substrate parameters (see Table 6), m determines the change of the current-voltage function, that is: $j \sim V^2$ at 0-2 V and $j \sim V^3$ at 2.1-5.0 V. Such a functional dependence gives a good description of experimental results obtained for abrupt *p-p*-heterostructures at applied voltage 0-5 V in case of prevailing tunneling currents and currents limited by the space charge region.

Table 6. Parameters used for the numerical simulation

Parameter	ZnCdHgTe	CdTe
Dielectric constant	16.3 ε_0	10.9 ε_0
Electron effective mass	0.01 m_0	0.11 m_0
Hole effective mass	0.55 m_0	0.35 m_0
Lattice parameter a, nm	0.6392	0.6478
Band-gap E_g, eV	0.32	1.44

Figure (18d) plots the experimental and calculated current-voltage characteristics of the examined heterostructure. It is shown the theoretical curves reveals a good coincidence with the experimental data at applied voltage 0.0 - 1.1 V in both forward and reverse directions; this section is fairly described by the expression given below:

$$I_1=A\exp(-\Delta E_v/kT)e\tau\mu_n\mu_p NV^2L^{-3}=BV^2, \quad (13)$$

where A is an electrical area of the sample, μ_n, μ_p are electron and hole mobilities of the epilayer, τ is a recombination life-time in *ZnCdHgTe*, N is a concentration of charge carriers localized in the space-charge region from the substrate side, L is a part of the space-charge region localized from the substrate side (both N and L values were calculated basing on capacitance-voltage measurements).

The observed discrepancies between experimental and calculated current values at 1.15÷2.0 V are believed to be caused by the influence of *ZnCdHgTe* epilayer surface microrelief [4 and refs. therein].

The forward section of current-voltage characteristic at 2.1-5.0 V can be approximated as follows:

$$I_2 = AX\exp[-(\Delta+E_{ss})/kT]\varepsilon_0\varepsilon_s\tau\mu_n\mu_p V^3L^{-5} = DV^3, \quad (14)$$

where X is a tunneling transparency coefficient, Δ was determined previously (see above).

The tunneling transparency coefficient value has been calculated in assumption that the potential barrier for the majority charge carriers can be described as an aggregate of microbarriers forming by the epifilm surface inhomogeneities. Thus, according to [4 and refs. therein], the triangle potential barrier approximation gives the following expression for X (the trap-assisted tunneling occurs in the interface states band E_{is}):

$$X = \exp\{-[(4d/3\hbar)(2m^*)^{1/2}[(\Phi_B-E_{is})^{3/2}/\Phi_B]+(E_{ss}/k_BT), \quad (15)$$

where d is a width of the barrier (is assumed to be equal approximately 0.09 μm), Φ_B is the barrier height (determined from the experimental measurements), m^* stands for the hole effective mass of the solid solution *ZnCdHgTe*.

The differences observed in that case (see Figure 18d, upper sections of the curves) are possible due to appearance of so-called exceeding tunneling currents as predicted by the theory [4 and refs. therein].

Thus, numerical simulation of *p-p*-isotype heterostructure *ZnCdHgTe/CdTe* current-voltage characteristics performed at room temperature have been shown the quadratic ($j_1=BV^2$ at 0.0-2.0 V) and cubic ($j_2=DV^3$ at 2-5 V) I-V dependencies where coefficients *B, D* strongly depend on the peculiarities of *ZnCdHgTe* epilayer surface and energy parameters of the examined heterostructure as an entity. The results of the computer experiment demonstrate the possibility of manufacturing active elements for charge-couple and tunneling devices.

LUMINESCENCE OF QUASI-2DEG IN HETEROSTRUCTURES BASED ON PBS FILMS

Highest performance of modern often requires more sophisticated structures and non-destructive methods of their properties analysis. Epitaxial techniques offer important advantages in comparison with the bulk grown ones: lower temperature, shorter growth time and reduced precipitation problems enable the growth of large-area samples with good parameters. At present, MBE (molecular-beam technology) is the most mature method of device-quality layer fabrication. In particular, semiconductor devices based on A^2B^6-A^4B^6 heterostructures are of special importance due to the well-known “window effect” as well as a possibility to act as a system of quasi-2D (2D denotes two-dimensional, and 3D denotes three-dimensional) or quasi-3D charge carriers [4 and refs. therein]. Results of photoluminescence studies performed at 77 K on the isotype n-n-heterojunctions *PbS/ZnSe* obtained by the MBE technology are presented here [4 and refs. therein].

The investigated isotype n-n-heterostructures *ZnSe/PbS* were grown by the MBE technology of lead sulfide (E_g = 0.41 eV) films with thickness up to 3 µm on the (110)-oriented *ZnSe* (E_g = 2.72 eV) wafers under the substrate temperature T_s = 540 K (the vacuum level in the effusion cell was estimated to be about 10^{-9} Pa). The samples of 1.5x3.5 mm2 size characterized by the film surface homogeneity were selected for the examinations. Parameters of the contacting materials are listed in Table 7.

Table 7. Parameters of the components of the investigated heterostructures

Material	Parameter
ZnSe	E_g = 2.72 eV
	a = 5.668 Å
	$\varepsilon = 9.1\varepsilon_0$
	$n_e = (7.8 \cdot 10^{16} \div 2.6 \cdot 10^{17})$ cm^{-3}
PbS:Na	E_g = o.41 eV
	a = 5.940 Å
	$\varepsilon = 175\varepsilon_0$
	$n_e = (2 \div 8) \cdot 10^{15}$ cm^{-3}

The electrophysical studies described for the first time in [4 and refs. therein].were shown that the heterostructures based on the materials mentioned in the present article are abrupt heterojunctions.

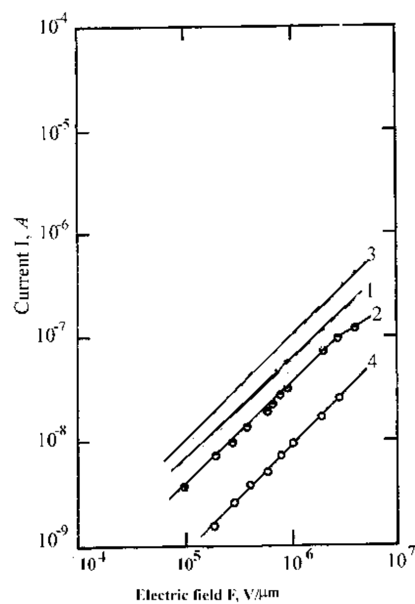

Figure 19. Field dependencies of the examined heterostructure *n-PbS/n-ZnSe*. Functions 1, 3 are forward sections and functions 2, 4 are reverse ones at 300 and 77 K, respectively [4 and refs. therein].

The further electric-field measurements (Figure 19) carried out on the as-grown specimens demonstrated that the processes of the charge carriers transfer are strongly affected by the space-charge region of the heterojunction formed by the surface electron states at the interface. The numerical analysis of the experimental *I-F*-measurements (where *I* stands for the current flowing through the heterojunction and *F* denotes the external applied electric field) showed that the I-F-function can be expressed according to the model developed in [4 and refs. therein]:

$$I = X_{tun}(2\varepsilon\varepsilon_0 A_{el} v_{sat}/LW)F, \quad (16)$$

where X_{tun} is the transparency coefficient of the potential barrier formed at the interface of the heterostructure depending on the energy spectrum of the surface electron states [4 and refs. therein], ε is the dielectric constant, A_{el} is an electrical area of the investigated sample, L takes care of the sample thickness, W stands for the width of the space-charge region determining from the capacitance-voltage measurements [4 and refs. therein] and v_{sat} is a complex function strongly influenced by the parameters of the contacting materials. Such a field dependence indicates on the inhomogeneous (quantum wells continuum, QW-continuum) structure of the potential barrier which determines not only the electric characteristics of the heterostructure but also the emission properties of the grown samples [4 and refs. therein].

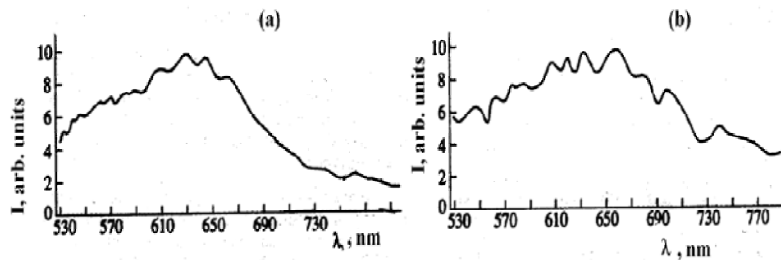

Figure 20. Photoluminescence (a) and electroluminescence spectra of the investigated *n-PbS/n-ZnSe* heterostructure. T = 77 K [4 and refs. therein].

Photoluminescence (PL) of the investigated structures was excited by the light source of the wavelength λ centered on 290 nm. Electroluminescence (EL) was excited by the electrostatic field, F = (0.9

- 1.8)$\cdot 10^6$ V/m. Both PL and EL spectra were registered at T = 77 K in the wavelength range from 0.48 up to 0.8 μm. As it is shown, PL and EL spectra are appeared as the wide Gaussian-like distributions in the wavelength range 0.53-0.80 μm describing by the expression [4 and refs. therein]:

$$I(\hbar\omega) \sim \omega^2 (\hbar\omega - \Delta)^{1/2} \exp[-(\hbar\omega - \Delta)/k_B T], \qquad (17)$$

where Δ stands for the value of the integrated potential barrier consisting of the QW-continuum, ω is a frequency of the excited light source. The energy positions of the emitted radiation maximums are estimated to be about 1.97-2.00 eV; The results show that the emission processes are take place in the subsurface region of the wide-gap material. such a value corresponds neither lead sulphide nor zinc selenide energy parameters as well as the energy levels of the known and uncontrolled impurities. The previous studies [4 and refs. therein] were shown the formation of the quasi-2D electron system at the interface of the examined heterostructures.

The experimental results obtained under the electro- and photoluminescent measurements had allowed concluding that the investigated structure presents a multi-QW continuum localized at the interface. The experimental results are plotted in Figure 20.

As it was mentioned above, the investigated isotype n-n-heterostructure *PbS/ZnSe* is appeared as a heterojunction with QW-continuum at the interface. The experimental data obtained from the luminescent studies showed that the non-equilibrium charge carriers were excited in the subsurface region of the wide-gap substrate adjacent to the spacecharge region of the structure, and then the carriers were confined in the QW-continuum and have relaxed energetically with radiative recombination.

In the other words, this so-called “graded barrier” [4 and refs. therein] acted as a suppressor of the carrier trapping at low temperatures, leading to an improved excitation transfer from the barriers to quantum wells (Figure 21).

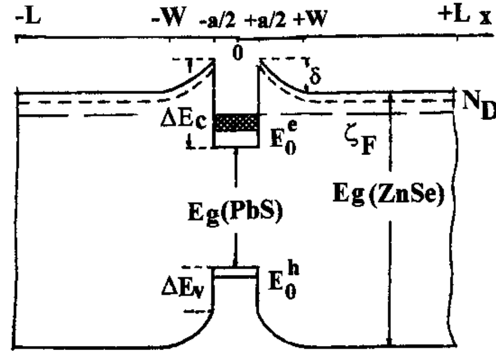

Figure 21. Energy band diagram of the examined heterostructure constructed according to [4 and refs. therein] (non-scaled, the main parameters are listed in Table 7) ΔE_c and ΔE_v are the conduction band and valence band discontinuities (the method of calculation is reported in [4 and refs. therein]), $(E_0)^e$, $(E_0)^h$ are energy positions of the electron and hole levels in quantum well, respectively, a is the quantum well width ($a = (\varepsilon\varepsilon_0 k_B T/e^2 N_d)^{1/2}$, other notes are explained in the text of the chapter [4 and refs. therein].

The barrier value δ was calculated according to the measurements performed previously [4 and refs. therein] and using the Schottky approximation for the depletion layers surrounding the quantum well, we have [4 and refs. therein]

$$(8\varepsilon_0 \varepsilon N_D \delta)^{1/2} = n_S^0 + \Delta n_S - \Delta p_S, \tag{17a}$$

where N_d is donor concentration in the wide-gap material, δ is the potential barrier, $(n_s)^0$ is the surface concentration of the equilibrium electrons, Δn_s stands for the concentration of the non-equilibrium electrons and Δp_s takes care for the concentration of the nonequilibrium holes.

Under equilibrium conditions $\Delta n_S = \Delta p_S = 0$ and

$$n_S^0 = \frac{m_e k_B T}{\pi \hbar^2} \ln\left[1 + \exp\left(\frac{\xi + \Delta E_c - E_0^e - \delta_0}{k_B T}\right)\right] \tag{18}$$

Here ξ is the Fermi level position in the wide-gap substrate, ΔE_c is a conduction band discontinuity [20], m_e is the electron effective mass in

ZnSe, $(E_0)^e$ is energy of electron level in the quantum well. The solution of the equations (7) and (8) makes it possible to calculate the equilibrium values of $(n_s)^0$ and δ. Results of the calculation are plotted in Figure 22.

As it is shown in Figure 22, the value of the barrier δ decreases as the donor concentration in the substrate increases, and the lifetime of the non-equilibrium carriers has to become larger [4 and refs. therein].

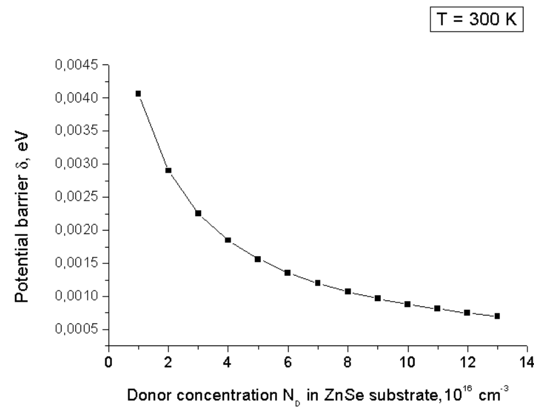

Figure 22. Potential barrier formed by the QW-continuum localized at the interface of the heterostructure vs. donors concentration in *ZnSe* substrate [4 and refs. therein].

At the same time, the intensity of the luminescence spectra in long-wave interval is comparable with the same characteristic in the short-wave region. Thus, the presence of the potential barrier δ increases the effective width of the quantum well for the non-equilibrium carriers under the low level of excitation.

In summary, isotype *n-n*-heterostructures based on thin lead sulfide films and zinc selenide demonstrated good emission characteristics at temperatures below 77 K strongly depending on the properties of the space charge region. The results of luminescent (PL and EL) experiments have been shown the formation of quantum-inhomogeneous barrier at the interface of the examined *n-PbS/n-ZnSe* heterostructure and the technological possibility of monitoring the carrier's confinement and ejection in the region of QW-continuum by means of proper doping of the substrate material [4 and refs. therein].

TIME STABILITY OF ELECTRICAL CHARACTERISTICS OF HETEROSTRUCTURES N-PBS/N-ZNSE [4]

High temperature electronics is likely to be dominated in the years ahead by wide bandgap semiconductor materials. Now the important problem of semiconductor materials science and technology is not only creation of new compounds and structures. The investigations of the time stability of their main structural and electrophysical characteristics are also important, especially the results of_room-temperature studies are of particular interest. From this point of view we had investigated the electrical parameters long-term stability for new heterostructures *n-PbS/n-ZnSe* [4 and refs. therein].

The heterostructures *n-PbS/n-ZnSe* were obtained by the HWE technique of lead sulphide films onto the monocristalline zinc selenide substrates. The growth was monitored with reflection high energy electron diffraction (RHEED). Growth rates were ranged from 0.05 to 0.1 $mm\ h^{-1}$ and the substrate temperature was about 540 K [4 and refs. therein]. Monocrystalline n-type (110) *ZnSe* (1-3 mm thickness) was used as a substrate. The (110) orientation was chosen because higher quality *PbS* films may be grown on this surface. The determined carrier concentration was equal to about (2-6)$\cdot 10^{17}$ cm^{-3} in the temperature range 77-300 K. Surface morphologies were studied by several methods, including X-ray double diffractometry, and Auger spectrosopy. The film thickness was measured with an interference microscope.

For detail examination we selected two sets of the samples characterized by the following carrier concentration of the *ZnSe* substrate: 7.8×10^{16} cm^{-3} (sample 1) and 2.8×10^{17} cm^{-3} (sample 2) at room temperature [4 and refs. therein].

In order to clarify the long-term stability of electrical properties we performed the electrical studies immediately after the samples preparation and after 3-4 years storage of those samples at normal ambient conditions. Current-voltage and capacitance-voltage dependencies were measured in the temperature range 77-300 K and at applied voltage V_a = 0-6 V in both directions. The results are presented in Figures 23, 24 [4 and refs. therein].

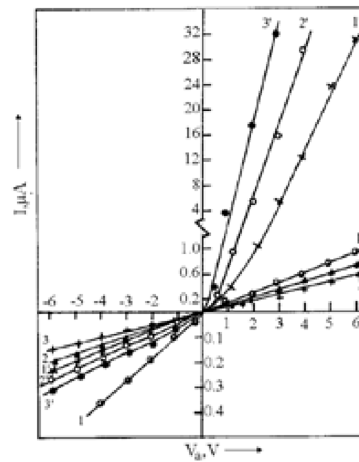

a

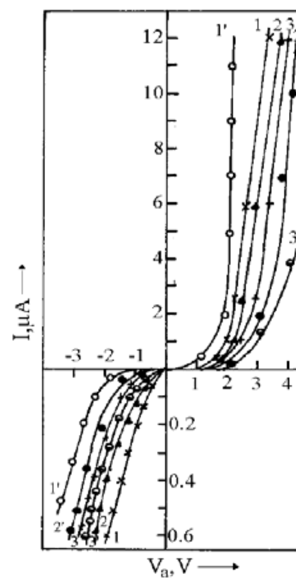

b)

Figure 23. I-V characteristics of examined heterojunctions with (a) n_{ZnSe}=7.8×10^{16} cm^{-3} and (b) n_{ZnSe}=2.8×10^{17} cm^{-3}. Curves 1, 2, 3 show current-voltage dependncies measured immediately after the samples preparation, curves 1', 2', 3' - after 3.5 year storage. T, K: 1, 1' -77, 2, 2' - 185, 3, 3' – 300 [4 and refs. therein].

As one can see, the examined heterostructures are abrupt heterojunctions because they are characterized by the linear dependence $C^{-2}=f(V_a)$ [17]. This dependence was observed after the samples preparation as well as after their storage. Indium contacts were fabricated as ohmic ones. To exclude the possible influence of *ZnSe/electrode* junction on the I-V and C-V characteristics of the investigated heterojunctions the electrical measurements were made for the structures *In/ZnSe* after the heterojuntion *n-PbS/n-ZnSe* growth, during and after the finishing of the storage period. The results [17] showed no considerable rectifying characteristics of these contacts.

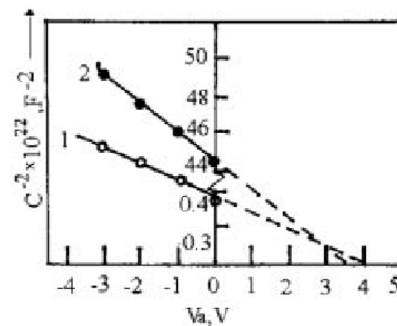

a)

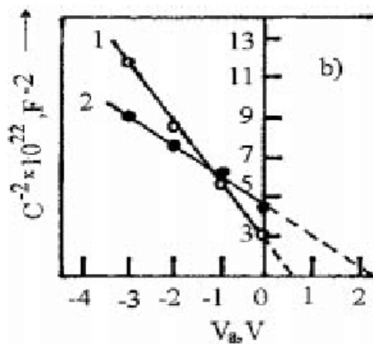

b)

Figure 24. C^{-2}-V_a dependencies of examined heterojunctions (T=300 K, test signal frequency f = 1 MHz): a - immediately after samples preparation, b - after 3 years storage. Carrier concentration in *ZnSe* substrate, cm^{-3}: 1- 7.8×10^{16}, 2 - 2.8×10^{17} [4 and refs. therein].

The current-voltage dependencies of the sample 1 (Figure 23a) were changed from linear ohmic characteristics to exponential ones with non-linearity coefficient $(I_F/I_R)_{Va=const}$ of about 1.02 at 77-300 K. Figure 23b presents two sets of I-V characteristics measured on the sample 2 at the same temperature interval. It is obvious that current-voltage dependencies for this sample had not been changed drastically [4 and refs. therein]. The numerical calculations carried out for the examined heterojunctions showed that the experimental dependencies are described by the following expressions:

$$I_F=Xev_{th}N_{ZnSe}\exp[-(\Delta E_c+E_{ss})/2kT]\exp(eV_a/nkT), \quad (19)$$

$$I_R=(I_s eV_a/kT)^m+I_{leakage}. \quad (20)$$

Figure (25) demonstrates the energy band diagram of heterojunction formed after 3.5 years storage; the valence band discontinuity ΔE_v was calculated according to [4 and refs. therein]. Here X (X is the tunneling transparency coefficient)) value is modulated by potential relief appeared on *PbS* surface (X_{tun} = 10^{-10}-10^{-7}), v_{th} is an arbitrary velocity of charge carriers in *ZnSe* substrate, ΔE_c is the conductance band discontinuity, E_{ss} is the surface electron states energy.

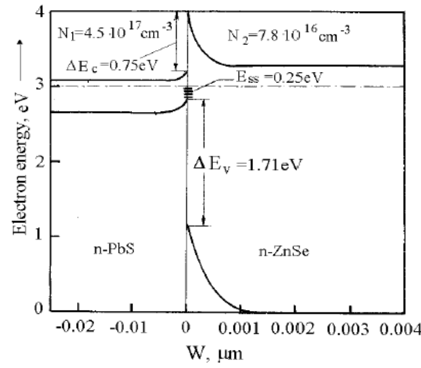

Figure 25. The energy band diagram of heterojunction (sample 1) (n_{ZnSe}=7.8×10^{16} cm^{-3}) after 3.5 year storage at T=300 K and V_a = 0 [4 and refs. therein]. The band parameters were calculated according to the theory described in [4 and refs. therein].

Table 8. Electrical parameters of *n-PbS/n-ZnSe* heterojunctions at room temperature [4 and refs. therein]

Parameter	Sample1 (growth)	Sample1 (storage)	Sample2 (growth)	Sample2 (storage)
C_{ss}, Fm^{-2}	$1.97 \cdot 10^{-4}$	$3.84 \cdot 10^{-4}$	$1.61 \cdot 10^{-4}$	$9.05 \cdot 10^{-4}$
Q_{ss}, $C \cdot cm^{-2}$	$5.47 \cdot 10^{-7}$	$5.23 \cdot 10^{-7}$	$4.42 \cdot 10^{-7}$	$7.84 \cdot 10^{-7}$
E_{ss}, eV	0.25	0.22	0.15	0.18
W_1, μm	0.23	0.21	0.05	0.01
W_2, μm	0.04	0.03	0.03	0.04
N_{ss}, cm-2	$3.43 \cdot 10^{12}$	$3.27 \cdot 10^{12}$	$2.76 \cdot 10^{12}$	$4.9 \cdot 10^{12}$
$N_{\text{"d.a."}}$,cm^{-2}	$3.33 \cdot 10^{10}$	$1.60 \cdot 10^{9}$	$1.13 \cdot 10^{13}$	$8.60 \cdot 10^{12}$

The results of C-V measurements of examined heterojunctions are plotted in Figure 24. As mentioned above, both heterostructures are abrupt heterojunctions in a wide temperature range and this peculiarity has not changed during the storage period. Thus, one can use the capacitance-voltage studies results and theoretical approximations for abrupt heterojunctions for numerical evaluation of some parameters characterizing the examined heterojunctions. They are following [4 and refs. therein]:

i) The space charge region capacitance C_{ss}:

$$C_{ss} = (AeN_2\varepsilon_2\varepsilon_0/2V_d)^{1/2}. \quad (21)$$

Here A is an electrical area of the heterojunction sample, e is an elemental charge, V_d is a diffusion potential, ε_0 is a dielectric constant;

ii) Widths of the space charge region on both sides at the interface of the heterojunction W_1 (*PbS* side) and W_2 (*ZnSe* side):

$$W_1 = (2N_1\varepsilon_0\varepsilon_1\varepsilon_2V_d/eN_2(\varepsilon_1N_1 + \varepsilon_2N_2))^{1/2}, \quad (22)$$

$$W_2 = (2N_2\varepsilon_0\varepsilon_1\varepsilon_2V_d/eN_1(\varepsilon_1N_1 + \varepsilon_2N_2))^{1/2}. \quad (23)$$

Here ε_1 and ε_2 are the dielectric constants of *PbS* and *ZnSe,* respectively, and N_1 and N_2 are the carrier concentration in *PbS* and *ZnSe*, respectively [4 and refs. therein].

In order to estimate the density of the surface electron states we need their full charge calculation [4 and refs. therein]:

$$Q_{ss} = -\{[2e\varepsilon_0\varepsilon_1 N_1 V_{d1}]^{1/2} + [2e\varepsilon_0\varepsilon_2 N_2 V_{d2}]^{1/2}\}, \tag{24}$$

where the contact potentials V_{d1} and V_{d2} are determined from the equations [17]:

$$V_{d2}=(\varepsilon_1 N_1/\varepsilon_2 N_2)\{(k_B T/e)[\exp(eV_{d1}/k_B T)-1]-V_{d1}\}, \tag{25}$$

$$V_d = V_{d1} + V_{d2}. \tag{26}$$

Here V_d is determined from the experimental I-V and C-V measurements; the considerable difference between $(V_d)^{I-V}$ and $(V_d)^{C-V}$ indicates the sufficient density of the surface electron states (Table 5) calculated from ratio [4 and refs. therein]

$$N_{ss} = Q_{ss}/e. \tag{27}$$

The experimental C-V measurements gave us the possibility to estimate directly the number of carriers taking part in current transport in the limits of "disturbed area" $N_{d.a.}$ [4 and refs. therein]:

$$N_{\text{"d.a."}} = 2/e\varepsilon_0\varepsilon_2(dC^{-2}/dV_a). \tag{28}$$

Now we have to calculate the energy spectra of the surface electron states E_{ss} [4 and refs. therein].

The full charge of the surface electron states localized at the heterointerface equals to sum of the same charges on both sides of heterojunction:

$$Q_{ss}= (Q_{ss})^{(1)} + (Q_{ss})^{(2)}. \tag{29}$$

The capacitance of the space charge region is

$$C_{ss} = (C_{ss})^{(1)} + (C_{ss})^{(2)}. \tag{30}$$

On the other hand,

$$(C_{ss})^{(j)} = 2e(n_i)^{(j)}(L_D)^{(j)}[((n_i)^{(j)}/N^{(j)})^{1/2}]\exp[-2E_{ss}/k_BT]. \quad (31)$$

Here $(n_i)(j)$ is an intrinsic carrier concentration in *PbS* ($j = 1$) or in *ZnSe* ($j = 2$), $(L_D)^{(j)} = (\varepsilon_0\varepsilon^{(j)}k_BT/2e^2(n_i)^{(j)})^{1/2}$ is Debye screening length. The simplest mathematical transformations give the following expression for E_{ss}:

$$E_{ss}=(k_BT/e)\ln\{e^4[(n_i)^{(1)}(L_D)^{(1)}((n_i)^{(1)}/N_1)^{-1/2}+ (n_i)^{(2)}(L_D)^{(2)}((n_i)^{(2)}/N_2)^{-1/2}]^2/(k_BT)^2(C_{ss})^2\}. \quad (32)$$

In summary, the obtained data show that the heterojunctions *n-PbS/n-ZnSe* grown on the zinc selenide monocrystals with the lower carrier concentration manifest the abrupt change of the current mechanism which is transformed from the linear one to the tunneling-recombination current caused by the interaction between the charge carriers and surface electron states. The heterojunctions based on the *ZnSe* substrate with the higher carrier concentration do not indicate the considerable change of the current mechanism [4 and refs. therein].

CAPACITANCE STUDIES AND CALCULATION OF ENERGY BAND DIAGRAM FOR HETEROJUNCTION $Zn_XCd_YHg_{1-X-Y}Te/CdTe$ [4]

C-V-measurements were performed at room temperature and under test signal frequency $f = 1$ kHz (Figure 26,a,b) [4 and refs. therein]. Two sets of samples of the isotype *p-p*-heterostructure $Zn_xCd_yHg_{1-x-y}Te/CdTe$ (x = 0.10-0.20, y = 0.01-0.10) were selected: a set of the films No.186 was characterized by *ZnCdHgTe* epilayer carrier concentration of about $9.6\cdot10^{15}$ cm^{-3} and that value for the samples of the set No.205 was about $1.11\cdot10^{16}$ cm^{-3} at 300 K. It is obvious that both C-V-characteristics are linear functions from reverse applied voltage (i.e., $C^{-2} = f(V_a)$); however, C-V-dependencies of the samples from the second group have two linear sections indicated step-like diminution of charge centers in the base of the heterostructure. Calculations performed according to the experimental data gave results listed below (Table 9) [4 and refs. therein].

Table 9. Electrical parameters of the heterostructure *p-ZnCdHgTe/p-CdTe* [4 and refs. therein]

Film	V_{d1} eV	$V_{d1(theor)}$ eV	V_{d2} eV	$V_{d2(theor)}$ eV	N_1, cm^{-3}	N_2, cm^{-3}
№ 186	0.7	0.235	-	-	$3.04 \cdot 10^{11}$	-
№ 205	0.6	0.189	0.28	0.305	$3.04 \cdot 10^{10}$	$2.9 \cdot 10^{8}$

Notes: for the samples of the set No.186 a linear charge centers distribution is observed, at the same time, for the films belonging to the set No.205 a step-like charge centers distribution is observed [4 and refs. therein].

As one can see, there is an appreciable discrepancy between the experimental values of heterobarrier heights (i.e., V_{d1}) and the theoretical ones. This difference consists of about (0.42-0.46) eV, which points out the charged states localized at the heterointerface. Their energy spectrum was calculated and illustrated by band scheme of the examined structures (Figure 27) [4 and refs. therein].

In order to build energy band diagram the theoretical model [4 and refs. therein] developed for heterojunctions with close dielectric constants of contacting materials was applied (Table 10) [4 and refs. therein].

Table 10. Parameters of the heterocmponents used for calculations [4 and refs. therein]

Parameter	ZnCdHgTe	CdTe
Dielectric constant	16.3 ε_0	10.9 ε_0
Electron effective mass	0.01 m_0	0.11 m_0
Hole effective mass	0.55 m_0	0.35 m_0
Lattice parameter a, nm	0.6392	0.6478
Band-gap E_g, eV	0.32	1.44

Main equations used for calculations are:

$$\Delta E_c = \Delta E_v + k_B T \lg \frac{N_{cA} N_{vB}}{N_{cB} N_{vA}} - (\Delta E_{ex} + \Delta E_{hxe}) - 2(\Delta E_m + \Delta E_b), \tag{33}$$

$$\Delta E_v + \Delta E_c = \Delta E_g , \tag{34}$$

where E_m ($m = c, v, g$) are the conduction band discontinuity, valence band discontinuity and difference between band-gaps of the contacting materials, respectively, N_c, N_v stand for effective state densities in *c*- and *v*-bands of both materials (A-index relates to *CdTe*, B-index relates to *ZnCdHgTe*) The third term in (34) accounts the effective electron-hole exchange-correlation energy:

$$E_{xc} \approx -2.5 \times 10^{-7} \left[1 + 0.7734 y \frac{\lg\left(1 + y^{-1}\right)}{N^{1/3} \varepsilon} \right], \tag{35}$$

$$y \approx 5.6 \cdot 10^{8} (m^*/e) N^{-1/3}, \tag{36}$$

where N and m^* denote the effective states density and effective mass of electrons or holes in both materials, the final term takes care of the image forces and heterointerface dipole bond energy due to interaction of dangling bonds [4 and refs. therein].

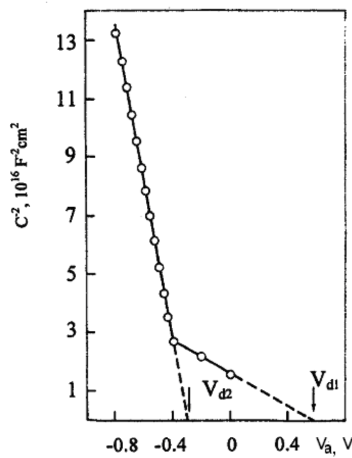

Figure 26a. Capacitance-voltage characteristics of the sample No.186, T=290 K, *f* = 1 kHz [1].

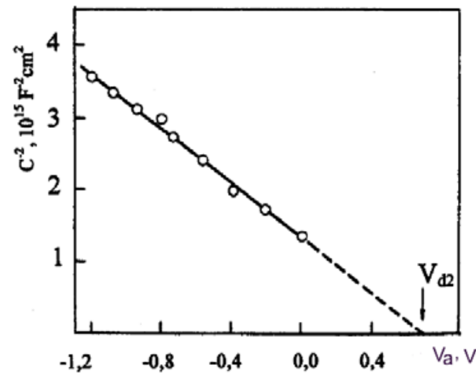

Figure 26b. Capacitance-voltage characteristics of the sample No.205, T=290 K, f = 1 kHz [4 and refs. therein].

The following equations describe the interaction of dangling bonds [4 and refs. therein]:

$$E_{im}(A) = \frac{(\varepsilon_B - \varepsilon_A)e^2}{\pi \varepsilon_0 (\varepsilon_B \varepsilon_A) \varepsilon_A d_b}, \tag{37a}$$

$$E_{im}(B) = \frac{(\varepsilon_B - \varepsilon_A)e^2}{\pi \varepsilon_0 (\varepsilon_B \varepsilon_A) \varepsilon_A d_A}, \tag{37b}$$

$$E_b(A) = \frac{e^2}{4\pi \varepsilon_0 \varepsilon_A d_B}, \tag{37c}$$

$$\mathrm{E_b}(B) = \frac{e^2}{4\pi \varepsilon_0 \varepsilon_B d_A}. \tag{37d}$$

Here $d=(3)^{1/2}a$, a is a lattice parameter of the corresponding material [4 and refs. therein].

In summary, examinations of *Zn-Cd-Hg-Te* quaternary system phase diagram allowed to grow epitaxial layers of $Zn_xCd_yHg_{1-x-y}Te$ solid solutions of different composition. Epitaxial heterostructures $Zn_xCd_yHg_{1-x-y}Te/CdTe$ are fabricated by liquid epitaxy from Te-rich solutions and

stoichiometric melts. Results of experiments presented here allowed to ascertain the dependence of $Zn_xCd_yHg_{1-x-y}Te$ solid solutions band gap on composition $\boldsymbol{x}$ and $\boldsymbol{y}$ [4 and refs. therein].

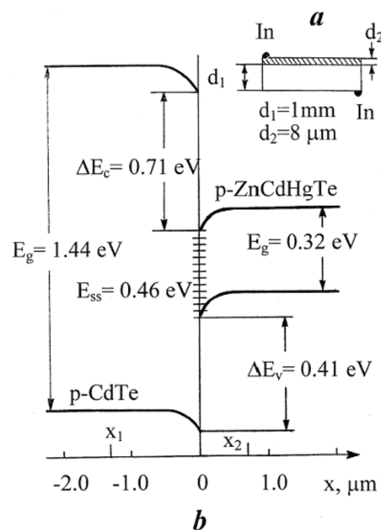

Figure 26. Energy band diagram of the heterostructure *p-* $Zn_xCd_yHg_{1-x-y}Te/p\text{-}CdTe$ at 290 K ($V_a = 0$) [4 and refs. therein].

CURRENT-VOLTAGE CHARACTERISTICS OF ZNCDHGTE FILMS GROWN BY MODIFIED LIQUID PHASE TECHNOLOGY [4]

Modified LPE technology described above is a powerful technique to grow new narrow-gap semiconductor *ZnCdHgTe* as a material alternative to *HgCdTe* solid solutions due to stabilizing effect of *Zn-Hg* bond. The results of electric studies performed on heterostructures $Zn_xCd_yHg_{1-x-y}Te/CdTe$ demonstrate barrier-like characteristics of investigated samples [4 and refs. therein].

Electrical measurements of the as-grown layers were carried out at the applied voltage V_a up to 3 V. Main attention was focused on current-voltage (I-V) measurements which serve as a useful nondestructive tool

suitable for the analysis of the electron transport in the examined structures. The current-voltage characteristics are plotted in Figure 27 [4 and refs. therein]. In order to clarify qualitatively the dominant current components the experimental I-V-dependencies were numerically analyzed. Strong space-charge limited (SCL) tunneling was observed in the forward direction of the applied voltage and transient processes *velocity saturation mode - mobility regime* were registered under reverse bias (Figure 27) [4 and refs. therein].

As it is seen, the experimental dependencies are governed by the power-like law: $I_{exper} \propto V_a^m$, where $m \geq 1$. Both forward and reverse I-V-characteristics of the sample 186 are described as follows [4 and refs. therein]:

$$I \propto \frac{2\varepsilon_0 \varepsilon v_{sat} A V_a}{L^2}, \tag{38}$$

where ε is the dielectric constant of the heterostructure *as a whole*, v_{sat} is the saturation velocity [4 and refs. therein]. The parameter v_{sat} strongly depends on the characteristics of the space charge region and the epifilm grown on the cadmium-telluride substrate, V_a is applied voltage, L is the thickness of the structure and A is geometrical area of the investigated sample [4 and refs. therein].

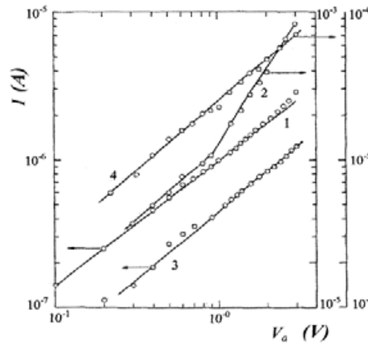

Figure 27. Current-voltage characteristics of the investigated structures (T = 290 K). Forward currents (1, 2) and reverse currents (3, 4) for samples 186 and 205 are shown, respectively [4 and refs. therein].

The forward characteristics of the sample 205 are described by the equation (38) under the applied bias up to 0.9 V and the forward current registered at $V_a > 0.92$ V is described by the following expression [4 and refs. therein]:

$$I \propto \frac{9\varepsilon \varepsilon_0 A \mu V_a^2}{8 L^3}, \tag{39}$$

where μ is the mobility of the charge carriers localized at the interface space charge region. Reverse current of this heterostructure is similar to that observed for the sample 186 [4 and refs. therein].

NUMERICAL MODELING OF ZNCDHGTE THIN FILMS CURRENT-VOLTAGE CHARACTERISTICS FOR LAYERS GROWN BY MODIFIED LIQUID-PHASE EPITAXY [4]

Here we present results of numerical simulation performed for the first time for the examined structures. Numerical modeling of the experimental I-V-data was carried out according to the calculated energy band diagram and the theory developed for the graded-gap structures [4 and refs. therein]. As mentioned above, the results of the microprobe analysis showed composition nonuniformity in the prepared films, this led to the formation of local regions with the concentration of charge carriers higher than the average distribution of carriers in the heterojunction plane. According to the theory developed recently [4 and refs. therein], the phenomenon described above leads to an exponential increase in the tunneling transparency of the interface barrier. The elemental current j is given as

$$j = j_{t0} + \sum \frac{A_i}{A} j_{ti}, \tag{40}$$

where j_{t0} denotes the tunneling current flowing through the heterojunction plane and j_{ti} is the tunneling current occurred in the local regions described above [4 and refs. therein]. This result can be

transformed into the integrated current through the complete heterojunction plane. As shown in Figure 28, the most probable transport of charge carriers is a step-like tunneling not only through the barriers formed due to the peculiarities of the growth technology but also through the barrier arising from the charge centers existing at the interface. However, assuming a Gaussian distribution of the local regions of high tunneling transparency, we can estimate the total current *j* [4 and refs. therein]:

$$j \propto \int \exp\left(-\frac{4m^{*1/2}E_{g2}^{3/2}}{3e\hbar F}\right)\exp\left(-\frac{(E_{g2}-\bar{E}_{g2})^2}{\Delta^2}\right)dE_{g2} \qquad (41)$$

where E_{g2} is the *ZnCdHgTe* band-gap (this is a variable of integration, the average band-gap is presented by the last term in the brackets of the second exponent), m^* is the reduced effective mass of charge carriers, F is the electric field in the heterojunction (it is a function of the charge states localized at the interface concentration and the diffusion potential; both parameters are determined by means of capacitance-voltage measurements) and Δ is a parameter taking care of the epifilm band-gap fluctuations $(\Delta << E_{g2})$ and the corresponding fluctuations in the interface barrier height. The tunneling parameter Δ was determined using the expression [4 and refs. therein]

$$I_{tun} = I_s \exp\left(\frac{m^* E_{g2}\Delta^2}{e^2\hbar^2F^2}\right), \qquad (42)$$

where I_s is a saturation current determined immediately from the I-V studies [4 and refs. therein].

Thus, the numerically simulated reverse current is described by the following expression [4 and refs. therein]:

$$I_R^{theor} = \frac{2\varepsilon_0 \varepsilon A v_{sat} V_a}{L^2} \exp\left(\frac{\phi_{B1}}{k_B T}\right) \exp\left(-\frac{\phi_{B2}}{k_B T}\right), \quad (43)$$

here $\varphi_{B1} = E_{ss} + E_{g2} - \Delta E_c$, $\varphi_{B2} = E_{ss} + \Delta$, $\Delta = 0.02 \div 9.22$ meV, k_B is the Boltzmann constant [4 and refs. therein].

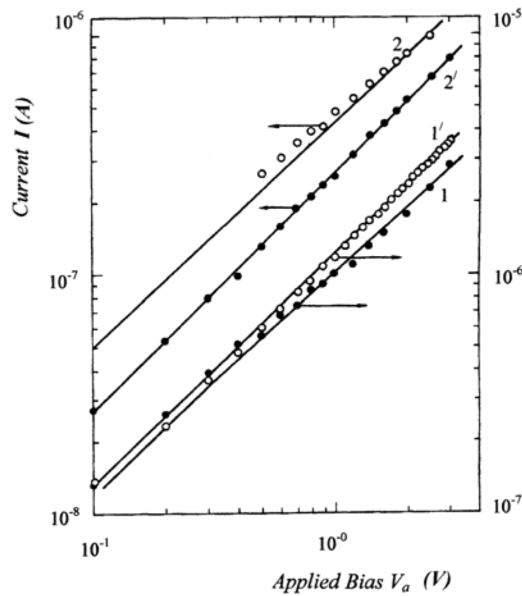

Figure 28. Comparison of calculated reverse (curve 1’) and forward (curve 2’) currents for sample 186 with the experimental data (curves 1 and 2, respectively) [4 and refs. therein].

As shown in Figure 28, a good quantitative agreement is observed in the range of the applied bias up to 0.6 V [4 and refs. therein]. The discrepancy between the experimental and calculated data under the increasing applied voltage is strongly connected with the surface leakage current. The forward section of the I-V-dependence (considering the applied voltage polarity, i.e. the positive direction is *substrate → epilayer* provided the charge carriers injection from the wide-gap material and calculated in the supposition about the carriers transfer

through the barrier formed by the valence band discontinuity) may be presented by the expression (44) [4 and refs. therein]:

$$I_F^{theor} = \frac{2\varepsilon_0 \varepsilon A v_{sat} V_a}{L^2} \exp\left(-\frac{\Delta E_v}{k_B T}\right). \quad (44)$$

Figure 29 (curve 2') illustrates the results of calculations. It is obvious that the power-like dependence is maintained in the entire range of the applied bias [4 and refs. therein].

The observed difference between the experimental and theoretical data demonstrates a strong influence of the exceeding tunneling currents which flow through the "pure" sample and are associated with the epifilm structure. However, the composition fluctuations and the consequential changes in the interface barrier height lead to the shunting effect observed experimentally [4 and refs. therein].

In summary, the results of electric measurements and numerical simulation performed for the first time at room temperature for *p-p*-isotype heterostructures $Zn_xCd_yHg_{1-x-y}Te/CdTe$ (x = 0.10-0.20, y = 0.01-0.10) grown by the method of the modified liquid-phase epitaxy under the applied bias V_a = 0-3 V show a power-like law governed space-charge limited current. The single-mode (so-called *velocity saturation regime*) and two-mode (*velocity saturation regime* → *mobility regime*) tunneling was observed. Microprobe studies revealed that the extended regions of various compositions localized in the heterojunction plane sufficiently affect the band-gap of the epifilm. The tunneling parameter arising from fluctuations in the *ZnCdHgTe* band-gap is calculated by numerical modeling [4 and refs. therein].

INFLUENCE OF THE STRUCTURE OF THE EPITAXIAL ZNCDHGTE FILMS SURFACE ON THEIR CURRENT-VOLTAGE CHARACTERISTICS [4]

Presently semiconductor quaternary solid solutions such as $Zn_xCd_yHg_{1-x-y}Te$ (x = 0.0-0.20, y = 0.0-0.10) are considered to be promising materials of active elements for microelectronic devices working in th temperature range 170-290 K [4 and refs. therein]. The

results of electro-physical characteristics investigations performed not only for epitaxial layers *ZnCdHgTe* but heterostructures based on $Cd_xHg_{1-x}Te$ (x = 0.0-1.0) and $Zn_yCd_{1-y}Te$ (y=0.0-0.08), monocrystals and epilayers mentioned above are of particular interest because the contacting materials' lattice parameter mismatch does not exceed 0.6-1.4% allowing to minimize the heterointerface electron states density, and the presence of zn atoms enhances the *Hg-Te* chemical bond and stabilizes the physical properties of these structures [4 and refs. therein].

The investigated heterostrutures were obtained by modified LPE technology [4 and refs. therein] of *ZnCdHgTe* films on monocrystalline substrates $Cd_{0.2}Hg_{0.8}Te$ and $Zn_{0.04}Cd_{0.96}Te$ of (111) orientation. The structural studies have shown the tessellated structure of as-grown films with 3-8 μm thickness. The typical size of tessel element was estimated to be 0.01-0.1 μm. Detailed Hall measurements indicated that *ZnCdHgTe* has a *p*-type surface conductivity including n-type conducting regions [4]. The majority carrier concentration has been estimated to be (6.7×10^{14} – 5.0×10^{15}) cm^{-3} at 77-290 K [4 and refs. therein].

The capacitance-voltage studies carried out in a wide temperature range (e.g. 77-290 K) demonstrated that the examined heterostructures have abrupt heterojunctions [4 and refs. therein]. In order to investigate current transport processes the current-voltage measurements were performed in the same temperature range. Both heterostructures showed similar current-voltage dependencies. The results for hetrojunction *p-ZnCdHgTe/p-CdHgTe* are plotted in Figure 29 [4 and refs. therein]. As one can see the forward I-V characteristics cn be described qualitatively by the classical exponential expression $I = I_0 exp(eV_a/nk_BT)$, where I0 is a parameter depending on the epilayer *ZnCdHgTe* properties [4 and refs. therein], n is the ideality factor of the heterojunction determining the current mechanism (in this case $n>>1$ for both sections of current-voltage dependence). The reverse currents indicate that in tunneling processes caused by an interaction of charge carriers and electron states located at the heterointerface (the dependence $I_R = f((V_a)^{1/2}))$ is a straight line in all ranges of applied voltage and temperature) [4 and refs. therein].

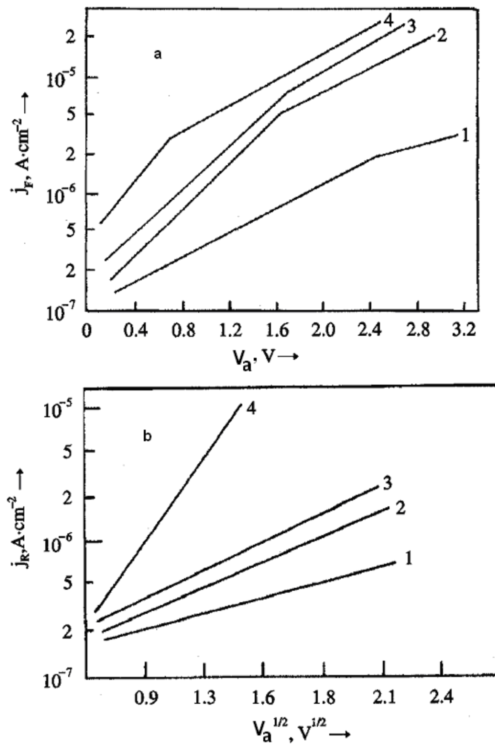

Figure 29. Experimental i-V characteristics of heterostructure p-$Zn_{0.13}Cd_{0.07}Hg_{0.80}Te$/p-$Cd_{0.2}Hg_{0.8}Te$. T(K); 1 – 179, 2 – 206, 3 – 235, 4 – 290; (a) forward sections, (b) reverse sections [4 and refs. therein].

The experimental current-voltage characteristics were numerically modeled [4 and refs. therein]. These I-V characteristics are strongly influenced by the effective number of charge carriers N and the so-called “effective electron length” d, determined as [4 and refs. therein]

$$N = \frac{j_{\min} L \exp\{(1-n_{\min})^{1/2}[(1-n_{\min})^{1/2}-1]\}}{e\mu V_a^{\min}[1-(1-n_{\min})^{1/2}]}, \qquad (45)$$

$$d = \frac{L k_B T (1-n_{\min})^{1/2}[1-(1-n_{\min})^{1/2}]}{e\varepsilon_1 V_a^{\min}}, \qquad (46)$$

where parameter n_{min} = $(V_a/j_{min})(dj/dV_a)$ was determined by graphical differentiation of experimental current-voltage dependences [4 and refs. therein].

The expression for I-V characteristics is as follows [4 and refs. therein]:

$$j = eN\mu V_a L^{-1}[\exp(\varepsilon_1 e V_a d / k_B TL)][1 + (4\mu V_a / v_{th} LP]^{-1}, \quad (47)$$

where μ, ε_l, v_{th} are the mobility, dielectric constant and thermal velocity of charge carriers in *ZnCdHgTe* material, L the electrical lngth of the heterostructure sample and P is the probability of carrier tunneling calculated in the semi-classical approximation. The experimental and calculated I-V dependences are presented in Figure 30 [4 and refs. therein].

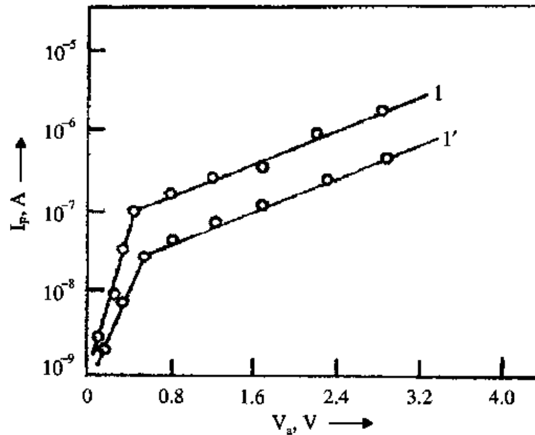

Figure 30. Experimental (curve 1) and calculated (curve 1’) I-V characteristics for the same heterostructure, T = 290 K [4 and refs. therein].

Thus, the obtained abrupt heterojunctions revealed the current-voltage dependences determined by the tunneling current mechanism resulting from the detailed numerical procedure [4 and refs. therein]. It seemed to be useful to consider the epilayer of *p-ZnCdHgTe* as a double-layer structure formed by the bulk-like *p*-type layer and the *n*-type surface-like layer, which is sufficiently strong to allow the analysis of the

observed results in terms of a two-step current mechanism: (i) the tunneling of majority carriers from the bulk of the substrate material to the heterointerface *HgCdTe/ZnCdHgTe* and their recombination at this heterointerface; (ii) the interaction of the *ZnCdHgTe* epilayer free carriers with the potential relief appeared as a consequence of the two-layer surface structure indicated above [4 and refs. therein].

The potential relief can be regarded as a circuit consisting of the islands of the *n*-type conductivity characterized by the effective carrier concentration N and the effective electrical length d [4 and refs. therein]. These values were estimated from the Hall measurements to be the following: $d \approx 10^{-5}$ cm^{-1} and $N \approx 10^{16}$ cm^{-3} [4 and refs. therein], which are in good agreement with the values resulting from the current-voltage studies (Eqs.(46-47)): $d \approx 1.6\times10^{-5}$ cm^{-1} and $N \approx 1.68\times10^{16}$ cm^{-3} [4 and refs. therein].

In summary, the current processes which occurred in the examined heterostructures are caused by the charge carriers tunneling along the local regions appearing on the surface of the epitaxial layer *ZnCdHgTe*. These regions are characterized by higher concentration of charge defects compared to its average value in the heterojunction area. Thus, the potential relief channel-island is formed and determines the observed data [4 and refs. therein].

Capacitance-Voltage Profiling of Heterostructures Based on Epitaxial ZnCdHgTe Layers [4]

Narrow-gap solid solution $Zn_xCd_yHg_{1-x-y}Te$ (ZCMT) has been proposed as a new material for different applications for optoelectronics. The ZCMT based devices are working in wide temperature (77-290 K) and wave-length ranges (4-12 μm). The narrow-gap ZCMT epitaxial layers that are normally deposited on wide band gap *CdTe* substrate form *p-p* heterostructures with various compositions. It is important to define the transition region properties of such structures and capacitance-voltage (C–V) technique seems to be very effective non-destructive characterization method for that purpose. It relies on the fact that the width of a reverse-biased space-charge region (SCR) of a semiconductor

junction device depends on the applied voltage. It should be noticed that defining the SCR could not be accurate due to the difficulties in determination of the straight heterojunction region coordinates [4 and refs. therein]. Classical methods which have been developed for this earlier [4 and refs. therein] do not recognize some of the important issues, such as (i) the effect of the surface states localized at the heterointerface; (ii) SCR spreading in the wide-gap substrate; (iii) uncertainty of the dielectrical constant value (which is usually different for the heterocomponents). Thus, the accurate profiling of charge carriers is a challenge.

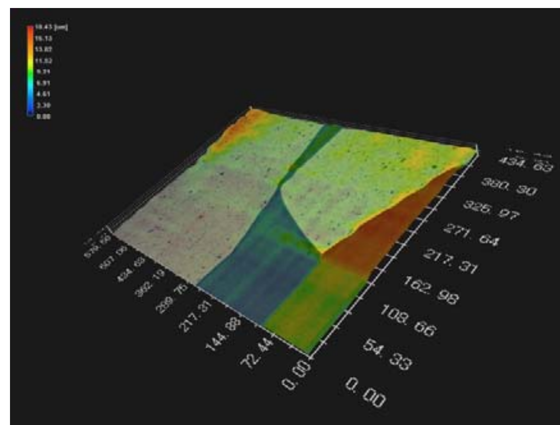

a

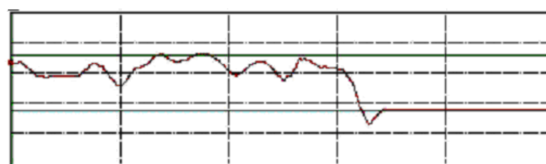

b

Figure 31. The surface profile of the layers (a) (the measured area (600x430) μm^2) is investigated by the digital microscope VHX-100K with profile measurement unit VHS-S15K (KEYENCE) (b), the thickness of the film was estimated to be about 8 μm.

ZnCdHgTe epilayers of 5÷8 μm thickness were grown on 3 mm thick *CdTe* (111) substrates with modified LPE technology [4 and refs. therein]. Structural studies of the grown structures revealed lattice parameters mismatch 0.32÷1.29 % of contacting materials and a presence of a transition region of various composition (TRVC) near the heterointerface. Various samples of p-p heterostructures $Zn_xCd_yHg_{1-x-y}Te/CdTe$ ($0<x\leq0.20$, $0.07\leq y\leq0.18$, $N_A - N_D = (10^{15}\div10^{16})$ cm^{-3} at the room temperature) with electrical area A_{el} = 6÷8 mm^2 were chosen for C-V-profiling at 300 K. Indium was used as a material for the electrical contacts. The electrical characteristics of In-*ZnCdHgTe-In* and *In-CdTe-In* structures were studied previously in order to clarify possible contributions in the total heterobarrier value and did not show any specific peculiarities.

Morphological and structural studies of the investigated structures are presented in Figure 31. The results showed inhomogeneous surface morphology.

The main parameters of the examined structure are listed in Table 11. C-V-measurements of the examined heterostructure were carried out under the test signal frequency f = 1 kHz and applied bias V_a = 0 ÷1 V. The simple band diagram is plotted in Figure 32.

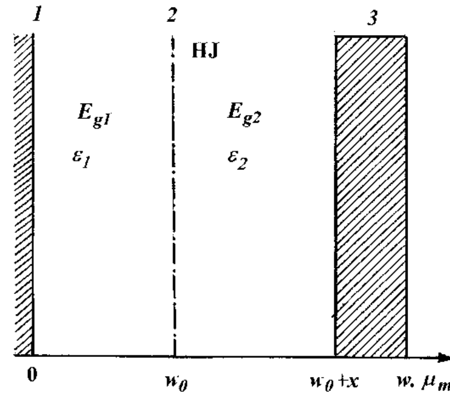

Figure 32. Band diagram of the examined heterostructure: 1 – *In-ZnCdHgTe* contact region, 2 – space-charge region, 3 – transition region of various composition.

The charge carriers' profile was calculated in accordance with the experimental data by the equation (48) [4 and refs. therein] (where ε_1 is dielectric constant of ZnCdHgTe epilayer and w is the width of TRVC):

$$p_{\text{exper}}(w) = \frac{2}{e\,\varepsilon_0 \varepsilon_1 A_{el}^2}\left[\frac{d(C_{\text{exp}\ er}^{-2})}{dV}\right]^{-1}, \quad (48)$$

and the height of potential barrier between the TRVC and ZCMT epilayer was determined as

$$V_{contact} = (kT/e)\{\ln((N_A - N_D)/n_i) + \ln(N_{cc}/n_i)\} \quad (49)$$

where n_i is ZCMT intrinsic carrier concentration estimated in standard way assuming *ZnCdHgTe* energy bands parabolicity:

$$n_i = 2\left(\frac{2\pi kT}{h^2}\right)^{3/2}\left(m_h^* m_e^*\right)^{3/4}\exp\left(-\frac{E_{g1}}{2kT}\right), \quad (50)$$

here N_{cc} is determined by means of C-V measurements. The calculations were resulted in heterobarrier height $V_{contact}$~ 0.21 eV.

Calculation of the heterostructure effective dielectric constant as a function of the coordinate x was based on the following considerations [4 and refs. therein]: under small reverse bias the SCR is localized near *In-ZnCdHgTe* contact region, so the initial section of the C-V characteristic is determined by the parameters of the narrow-gap compound (E_{g1}, ε_1).

As the reverse voltage increases, the SCR edge crosses the heterointerface (including the part which is localized near the heterointerface) and moves into depth of the wide-gap substrate (Figure 32). Under these conditions the capacitance value on the right side of the heterointerface is determined by the parameters of wide-gap substrate. Here E_{g1} and ε_1 are band-gap and dielectric constant of the narrow-gap *ZnCdHgTe* epilayer, E_{g2} and ε_2 are the corresponding parameters of *CdTe* substrate. Although the experimental C-V measurements show the

linear dependence $C_{exper}^{-2} = f(U_a)$ (Figure 34, function 1), the charge carriers' profile determined from these data according to the theory described in [4 and refs. therein] (Figure (34), curve 1) does not pretend to be a correct one because the heterojunction coordinate is not exactly known in advance.

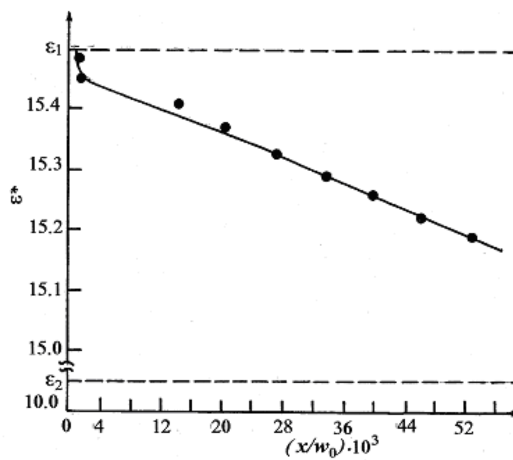

Figure 33. Dependence of the effective dielectric constant from the width of TRVC.

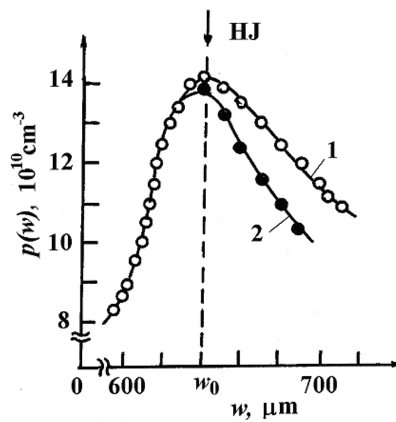

Figure 34. Initial (curve 1) and corrected (curve 2) charge carriers profiles near the heterointerface.

For more accurate calculations we assumed [4 and refs. therein] that the heterointerface is located at a distance w_0 from ZnCdHgTe side (Figure 33). Also we used the flat capacitor model to determine the complete capacity of examined structure under applied reverse bias V_a :

$$C = \frac{C_1 C_x}{C_1 + C_x}, \tag{51}$$

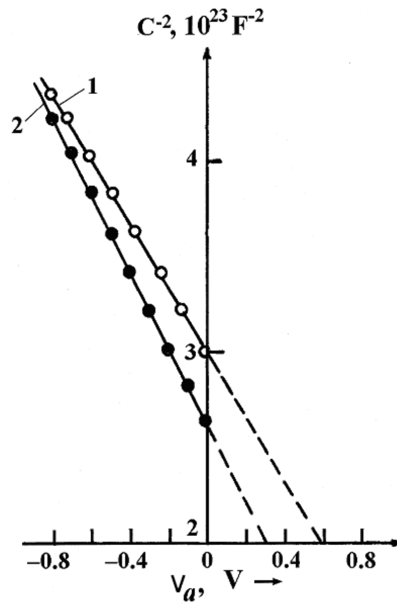

Figure 35. Experimental (function 1) and numerically modelled (function 2) capacitance-voltage characteristics of the examined heterostructure.

where C_1 represents the narrow-band gap epilayer capacitance and C_x is capacitance of the wide-gap substrate with thickness x. Thus, we have obtained two expressions for C and ε^*:

$$C = \frac{\varepsilon^* \varepsilon_0 A_{el}}{w_0 + x}, \tag{52}$$

$$\varepsilon^{*} = \frac{w_0 + x}{(w_0 / \varepsilon_1) + (x / \varepsilon_2)} . \tag{53}$$

The results of the calculations are plotted in Figure 35 and Figure 36. The effective dielectric constant value, which is very close to that of the narrow-gap compound, demonstrates that the SCR is placed near the heterojunction and the corrected carriers' profile $p_{corr}(w)$ (Figure 34, curve 2) is different from the experimental curve determined by the expression (52).

The examined structures with their lattice mismatch form the surface states band that is localized near the heterointerface from the side of narrow-band epilayer. This can cause noticeable effect on the heterostructure barrier characteristics [6,7]. In order to clarify the surface states effect on the heterobarrier height experimental C-V dependence was numerically simulated using the equation (51) [4 and refs. therein], where C_{theor} is considered only as a function of the V_d^0 value (Figure 35).

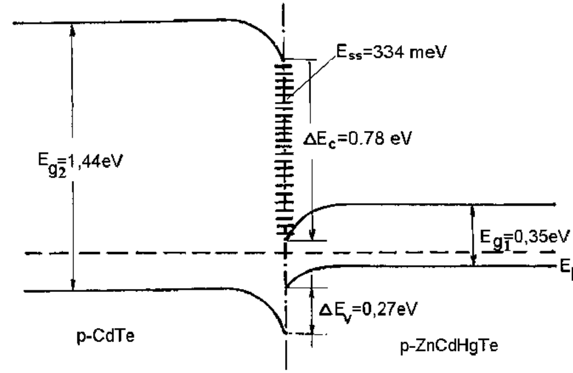

Figure 36. Energy band diagram of the *p-p*-heterostructure *ZnCdHgTe/CdTe* calculated with accounting surface states influence (T = 290 K, $V_a = 0$).

In our approximation, depending on some peculiarities of the TRVC, the diffusion potential V_d^0 was substituted for the so-called effective contacting potential [4 and refs. therein], similarly to the presence of

surface states that caused by the heterocomponents' lattice mismatch [4 and refs. therein] (Figure 36):

$$C = \frac{A_{el}}{2}\sqrt{e^2 \varepsilon_0 \varepsilon_1 \frac{p_{1corr}}{V^0_{d(exper)} + E_{ss} + kT \ln\frac{p_1 \mu_1 E_1}{p_2 \mu_2 E_2} + eV_a}} \tag{54}$$

where E_i ($i = 1, 2$) are electrical fields in the epilayer and in the substrate near the heterointerface, respectively, p_i and μ_i are the majority charge carriers' concentrations and mobilities, and E_{ss} is the surface states energy spectrum. The corresponding electrical field values were determined as

$$E_i = \sqrt{\frac{eV_{di} p_i}{2\varepsilon_0 \varepsilon_i}}, \tag{55}$$

where V_{di} are diffusion potentials referred to the epilayer and substrate which are calculated numerically from the equation (49) based on experimental data:

$$V_{di} = \frac{1}{2}[V^0_{d(exper)} - (-1)^i kT \ln\frac{p_1 \mu_1 E_1}{p_2 \mu_2 E_2} - eV_a] \tag{56}$$

The comparison of these data illustrates a good qualitative agreement between the functions $C^{-2}_{exper} = f(V_a)$ and $C^{-2}_{theor} = f(V_a)$. The theoretical function $C^{-2}_{theor} = f(V_a)$ produces the value .of the heterobarrier $V_d^{theor} \approx 0.30$ eV closed to the $V_{contact} \approx 0.21$ eV.

In summary, the charge carriers profile obtained with the proposed correction matches more accurately the experimental charge carriers' distribution in comparison with that calculated according to the expression (50). The numerical simulation of C-V dependence demonstrated effect of the transition region presence of various compositions localized near the wide-gap substrate interface.

SURFACE STRUCTURE AND ELECTOPHYSICAL PROPERTIES OF ZNCDHGTE THIN FILMS PRODUCED BY PULSED LASER DEPOSITION METHOD AND MODIFIED LIQUID PHASE EPITAXY [4]

Pulse laser deposition (PLD) is a well-known method of depositing thin films and their composed structures [4 and refs. therein]. It has been even recognized as the most versatile method of the thin film preparation techniques.

In recent years, quaternary mixed crystals, such as *CdHgMnTe* or *CdHgZnTe* have attracted much attention [4 and refs. therein]. Laser technology applied for preparation of the corresponding thin films is a perspective and reliable method.

The PLD process takes place in a standard vacuum plant equipped with a turbomolecular pump (Figure 37) [4 and refs. therein]. The optical path of the laser beam is shown by dotted lines.

Target materials are vaporized by pulsed YAG:Nd laser placed in the vicinity of the vacuum chamber. Three different materials can be evaporated from three rotating targets placed side-by-side in the vacuum chamber. The targets are driven from the outside of the vacuum chamber with a help of the magnetic clutch. The angular speed of the targets can be suitably matched to the laser pulse frequency to avoid the overlapping of two sequential laser beam spots on the target surface. The pulse frequency can be chosen between 1 and 50 Hz. Typical working frequency is 10 Hz. The energy of a single pulse can be changed in the range (0.2-.5) J and its duration is 100 ms [4 and refs. therein].

The laser beam is focused on the targets by a concave metallic mirror. Between this mirror and the targets, the laser beam is deflected by another (flat) mirror which switches the beam between targets. Both mirrors are covered by a suitable dielectric thin film to increase the reflectivity to near 100% [4 and refs. therein].

The deflecting mirror is placed on a tripod of which each arm can be electromagnetically shortened slightly to deflect the beam in the proper direction. In this way the laser pulses can be switched between the targets. The time needed to switching the beam between targets can be shorter than 100 μs [4 and refs. therein].

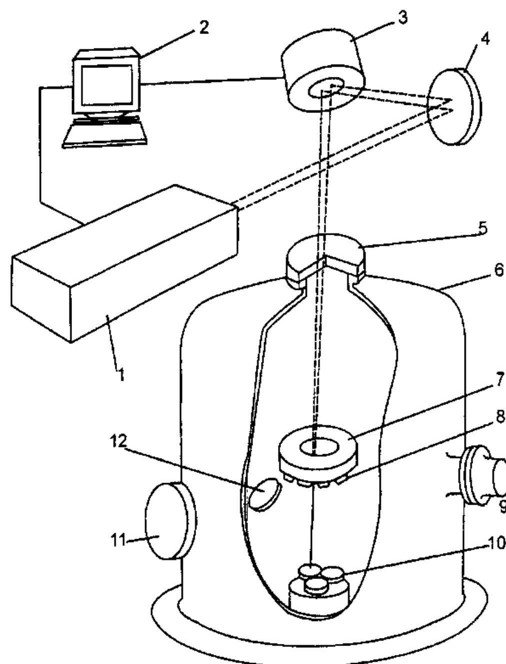

Figure 37. Experimental setup for PLD of A2B6 compounds thin films. The dotted lines show the optical path of the laser beam. (1) YAG:Nd laser; (2) computer controlled system of the laser beam monitoring; (3) device switching the laser beam between targets (optical detector); (4) focusing mirror; (5) optical port; (6) vacuum chamber; (7) substrate holder and heater; (8) substrates; (9) quadruple mass spectrometer port; (10) targets setup; (11) peephole; (12) piezoelectric quartz of the film thickness measuring device [4 and refs. therein].

The evaporated material is condensed on substrates, which are attached to a heater placed above the targets. The targets are pellets, 2 cm in diameter and several millimeters thick, made of powdered material pressed under the pressure of 2.5 MPa. As the laser spot has the diameter of the order of 1 mm, many powder grains are vaporized simultaneously by a single pulse. Under these conditions, a *CdZnTe* target can be prepared from *CdZnTe* powder or from the mixture of *CdTe* and *ZnTe* powders [4 and refs. therein].

The process of the laser pulse triggering and the switching between the targets is computer controlled. By appropriate computer program any set of laser pulses deliberately distributed between the three targets can

be executed. Such a set can subsequently be repeated many times in sequence. In this way, if the targets are made of different materials, one can obtain a mixed material thin film or a sequence of different films (a superlattice) of compositions corresponding to the chemical compositions of the targets or even a superlattice composed of the mixed material layers [4 and refs. therein].

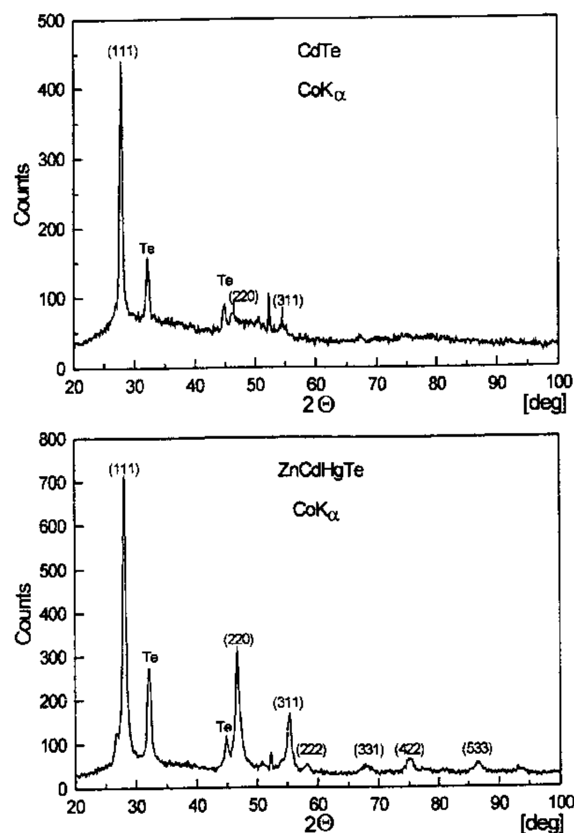

Figure 38. X-ray diffraction patterns for *CdTe* (top) and *ZnCdHgTe* (bottom) thin films. Lines from the *Te* inclusions are also shown [4 and refs. therein].

In the experiments described above the laser pulse energy ranged from 0.3 to 0.5 j, and the spot diameter was about 2 mm. As the result it has been found that the available, splashing-free evaporation rte per pulse

ranges from 10^{-3} to 10^{-1} nm/pulse [4 and refs. therein]. The lower limit corresponds to the evaporation time of several hours for preparation of a film of about 0.5 µm thick [4 and refs. therein].

The films were deposited on clean glass substrates kept at room temperature. Figure (38) shows X-ray diffraction patterns taken in the Bragg configuration from a *CdTe* film 380 nm thick and a *CdHgZnTe* film 650 nm thick (the compositions of the samples are given in Table 11, sample A) [4 and refs. therein]. The evaporation rate was in the range (2-5)10^{-3} mm/pulse [4 and refs. therein].

It is seen that the films are of polycrystalline character with well-crystallized grains. Some preferential orientation in the (111) plane is also observed. Another clearly seen feature is the presence of the tellurium precipitates [4 and refs. therein].

Table 11. Chemical composition of *CdZnHgTe* samples as obtained from XPS analysis [4 and refs. therein]

Film (Nr.)	Target/film	Hg (at.%)	Cd (at.%)	Zn (at.%)	Te (at.%)
A	Target	25.8	5.0	19.2	50.0
	Film	14.7	4.7	16.4	65.5
	Film corrected	20.5	6.6	22.9	50.0
B	Target	40.0	5.0	5.0	50.0
	Film	16.6	6.4	11.0	66.0
	Film corrected	24.4	9.4	16.2	50.0

The chemical composition of two *CdHgZnTe* films was determined from XPS (X-ray photon spectroscopy) investigations [4 and refs. therein]. They confirm that Te appears in two chemical states, which can be ascribed to the free tellurium inclusions and the tellurium entering the compound [4 and refs. therein].

The original data from the XPS investigations for the films are shown beneath the data for the targets (Table 11). The observed relative increase in *Te* content is obviously owing to the *Hg* deficiency. Since it is known that the film is composed of *CdHgZnTe* crystal with Te inclusions, one can determine the crystal composition by assuming that the *Te* content in the crystal is 50% and increasing proportionally to the content of the remaining elements. In such a way corrected film compositions are listed in the third row of the composition data for each

film (Table 11). It is seen that the crystal always has smaller *Hg* content, in comparison with the target, and the *Hg* deficiency is very large in the case of the crystal with high mercury content. Because of the *Hg* deficiency, the relative content of *Cd* and *Zn* is higher. However, the increase in the content is higher for *Zn*. This means that not only mercury re-evaporates from the substrate, but also cadmium does, however to much lesser extent. The latter conclusion is in accordance with observed deficiency of *Cd* in the *CdTe* film [4 and refs. therein].

The question: how does the surface of the layers influence their electric field-induced characteristics, is also of special importance. We consider it for the *ZnCdHgTe* films with inhomogeneous structure of the surface.

As the technological peculiarities of the growth of large-area *ZnCdHgTe* epitaxial films required by the modern photonics can lead to the sufficiently inhomogeneous film surface, the study of the carriers transfer affected by such a relief is seemed to be important.

The microscopic investigations were demonstrated that the as-grown *ZnCdHgTe* film is characterized by the surface relief appeared as aggregates of clusters with typical size in the range of $10^{-2} – 1 \cdot 10^{2}$ μm.

Figure (39) presents the optical image of the surface of investigated sample. *In-Ag* contacts were used for electrical investigations performed not only on the epifilms but also on the specimens of the isotype heterostructures *p-ZnCdHgTe/p-CdTe*.

Experimental current-voltage characteristics (IVC) of the structure investigated are shown in Figure (40). Under the applied bias up to 0.7 V a weak S-like forward dependence is observed. At the same time, the reverse IVC demonstrates a soft exponential character.

To obtain more specific information about the charge transfer processes in the heterostructure the experimental IVCs were recalculated in double logarithmic scale (Figure (41)). As it is shown, three modes of the carriers transport are observed: i) tunneling: $I \sim (V_a)^{3/2}$; ii) space charge limited current: $I \sim (V_a)^{3}$; iii) quasi-ohmic current: $I \sim (V_a)^{n}$, $n < 1$, where V_a is an applied bias.

The reverse IVC (Figure (41)) demonstrates diffusion process up to 0.3 V and velocity saturation current ($I \sim (V_a)^{m}$, m »1) as the voltage increases.

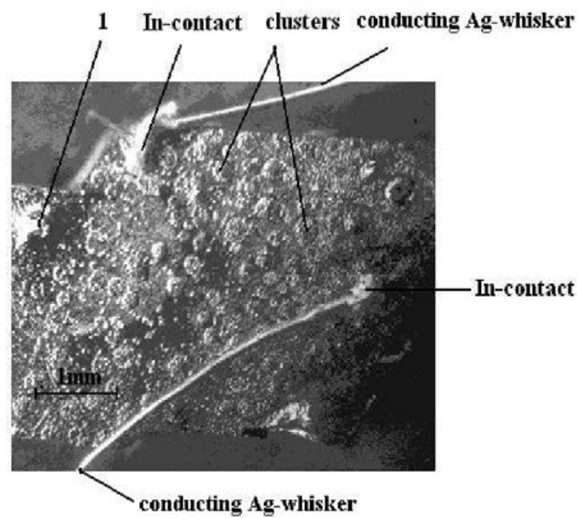

Figure 39. ZnCdHgTe epifilm surface relief; 1 denotes the clusters aggregate.

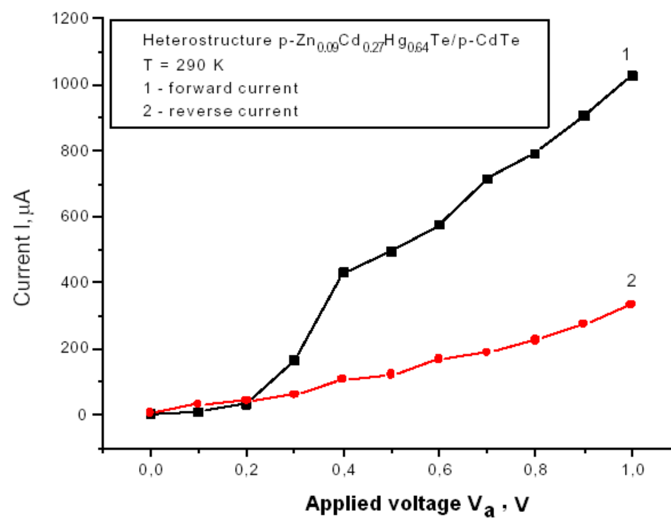

Figure 40. Experimental current-voltage characteristic of the investigated heterostructure.

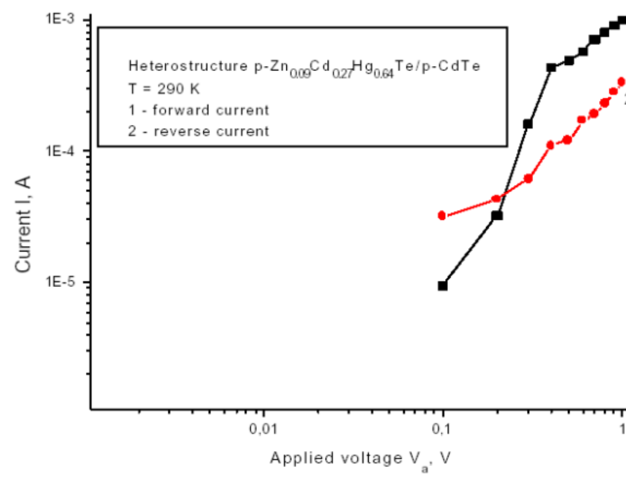

Figure 41. Double-log scaled experimental IVC of the same structure.

The further calculations revealed a necessity of taking into account the so-called surface-leakage current due to the defects of the film surface and inhomogeneity of the interface *film – substrate*.

The randomized relief of the surface contributes to the experimental current as follows:

$$I = \left(\frac{R}{r}\right) I_s \exp(-\alpha\phi(r)) \exp\left[-e(E_g - V_a)/k_B T\right], \quad (57)$$

where $\alpha = (4/3\hbar)(m_e^* \varepsilon\varepsilon_0 / \delta N)^{1/2}$, r is a variable determined by the clusters size range, I_s stands for the saturation current (a complete function strongly depending on the main parameters of the material and determined from the experimental measurements), E_g is the gap of *ZnCdHgTe* film (this value is a composition function), R is the cluster size, δN is the concentration of carriers immediately taking part in process of the charge transport evaluated by the experimental capacitance-voltage measurements, V_a denotes the applied bias. The randomized potential *f(r)* is estimated according to the expression given below:

$$\phi(r) = a(r_0^2)\lfloor 1-(r_0/r)(1+R/r_0)\exp(-R/r_0)sh(r/r_0)\rfloor, \quad (58)$$

where $a = e\,\delta\,N/\varepsilon\varepsilon_0$, $(r_0)^{-2} = n_i e^2/\varepsilon\varepsilon_0 k_B T$, both parameters are determined by the properties of *ZnCdHgTe* epifilm, n_i stands for intrinsic carriers concentration calculated in assumption of parabolicity of the band structure of the solid solution *ZnCdHgTe*. Results of the corresponding calculations are presented in the Figure (42).

It is obvious that the sufficient contribution in the current is caused by the carriers tunneling through the cluster aggregates with size of about 100 mm. Diffusion and tunneling of the carriers through the smaller aggregates are observed under the applied voltage from 0 to 400 mV.

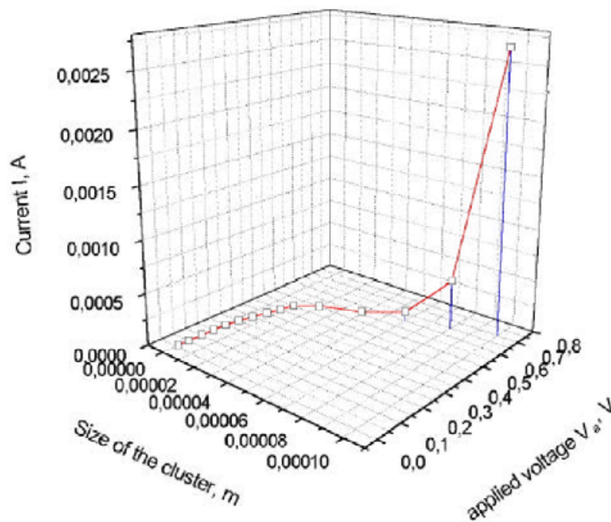

Figure 42. IVC calculated according to the Eq. (57).

In summary, room temperature current-voltage characteristics of the isotype *p-p*-heterostructure *ZnCdHgTe/CdTe* are investigated under applied bias no more than 1.0 V. Different processes of the charge carriers transfer through the interface of the heterostructure are observed: tunneling and quasi-ohmic currents in the forward direction and diffusion and soft ohmic currents under the reverse bias. As the surface of the *ZnCdHgTe* film grown by means of the modified liquid phase technology

on the monocrystalline *CdTe* substrate revealed cluster-like relief and the interface *film-substrate* was also inhomogeneous, it is necessary to take into account the randomized potential appeared on the surface of the film. Data of the calculations demonstrated the considerable contribution to the current of the carriers supplied by the clusters of 100 mm size.

STUDY OF FUNCTIONAL POSSIBILITIES OF ACTIVE ELEMENTS BASED ON ZNCDHGTE FILMS OBTAINED BY LASER TECHNOLOGY [4]

Narrow-gap semiconductor materials belonging to the group A^2B^6 compounds are important for some fields of optoelectronics used for various needs of device fabrication. Heterojunctions based on epitaxial layers *ZnCdHgTe* are of particular interest owing to the simplicity and reliability of growth technology (modified liquid phase epitaxy and pulse laser deposition (PLD) technique). The investigation of experimental data obtained from the simplest electric-field measurements provides a reasonable base for the computational modeling of active elements based on graded-gap semiconductors [4 and refs. therein].

Monocrystalline $Zn_xCd_yHg_{1-x-y}Te$ ($0<x<0.49$, $0<y<0.18$) films were grown on glass substrates by PLD technology using pulse YAG:Nd laser. Deposition was carried out onto substrates under the room temperature. Thickness of the layers was estimated to be 0.065–0.70 μm, room-temperature resistance of the as-grown layers was estimated to be about 10^7 Ohm [4 and refs. therein].

As the targets for the deposition pellets prepared from powder-like binary compounds *CdTe*, *ZnTe* and HgTe were used. To obtain a regular composition of the grown layers the targets were rotated around their axis of symmetry with distance between the target and substrate of 60–90 mm; deposition time ranged from 2 to 6.5 h, the growth chamber pressure was about 10^{-4} Pa. Room-temperature parameters of the as-grown films are as follows: $E_g(Zn_{0.49}Cd_{0.07}Hg_{0.44}Te)$ = 0.81 eV, $E_g(Zn_{0.10}Cd_{0.10}Hg_{0.80}Te)$ = 0.24 eV, $E_g(Zn_{0.39}Cd_{0.18}Hg_{0.43}Te)$ = 0.86 eV, and $n_i = 3.1 \cdot 10^{11}$ cm^{-3}, $n_i = 1.1 \cdot 10^{16}$ cm^{-3} and $n_i = 1.4 \cdot 10^{11}$ cm^{-3}, respectively (see expressions (1)-(2)).

The best samples of 1.8 mm^2 electric area A_{el} were chosen for studies of the room-temperature current-voltage characteristics. The measurements were carried out also under the illumination of the samples by the light source of 100 W power. The range of applied bias V_a was 0-30 V. Note that the experimental current–voltage characteristics demonstrated no considerable difference regardless of the various values of the gap [4 and refs. therein].

Figure (43a) plots the typical experimental data. As one can see, these dependencies are of diode-like character, so that we are able to simulate the data according to the classical models of the physics of semiconductor devices [4 and refs. therein].

To investigate the photosensitivity of the films grown on the single crystal *CdTe* substrates capacitance–voltage measurements were carried out for the as-grown heterostructure *ZnCdHgTe/CdTe* (Figure (43b)). Both dark and light dependencies are also of the barrier-like character [4 and refs. therein].

As it is shown, both dark and illuminated current–voltage dependencies are similar. The weak additional photocurrent is observed under the irradiation of the films by the source of incoherent light. The threshold bias signing the change of the carriers transport mechanism is about 1 V. The current–voltage characteristic can be described as follows [4 and refs. therein]:

$$I_r = I_s\exp(eV_a/nk_BT) + XA_{el}N_0(D_n/\tau_n)^{1/2}\exp[-(eV_d + E_i)/k_BT](\exp[eV_a/k_BT] - 1), \quad (59)$$

$$X = \exp[-(4(2m^*)^{1/2}/3\hbar)d(U-V_d)^{3/2}/U + eV_d/k_BT)], \quad (60)$$

where n is the slope of the experimental curve, X is the tunneling transparency coefficient strongly depended on the threshold voltage U (in our case X is calculated according to the parabolic VCB approximation), N_0 and V_d are the concentration of the charge carriers at the top of the potential barrier and its height (these values are usually determined by the capacitance-voltage studies), d is the barrier width, D_n and τ_n take care of the electrons diffusion coefficient and lifetime, respectively, E_i is the semiconductor potential energy required by the charge carrier to escape the barrier top which also appeared as a function of the .lm surface relief and the applied voltage [4 and refs. therein].

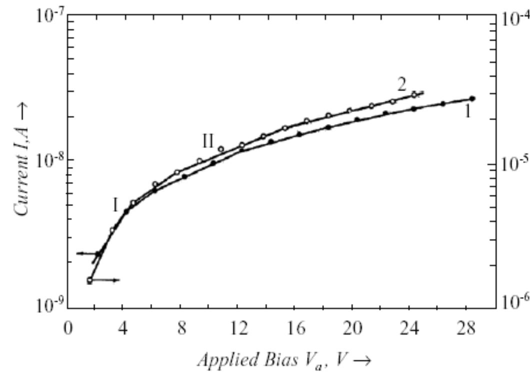

a

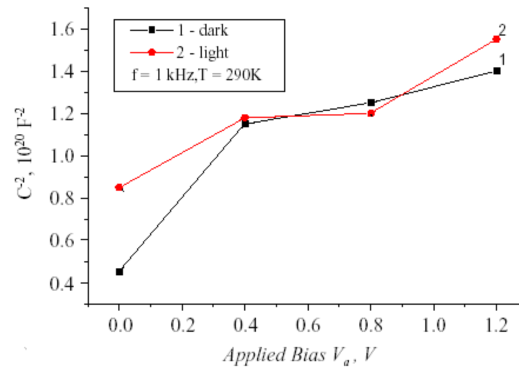

b

Figure 43. (a) Current–voltage characteristics of the investigated samples, T = 290 K. ● - dark current, ○ -light current. Slope I is 2.4, slope II is 0.5–1.07. (b) Capacitance–voltage characteristics of the heterostructure *ZnCdHgTe/CdTe* [4 and refs. therein].

The numerical analysis of the experimental data revealed the necessity of taking into account the effect of atmospheric oxygen (at least up to one monolayer) on the experimental current–voltage characteristics. Due to the large electronegativity (≈ 3.5 eV) oxygen has to create acceptor states in the corresponding material. Their filling (i.e. the dipoles formation) occurs during the process of electrons transfer from the valence band of the compound. The numerical simulation has demonstrated that the current-voltage characteristics performed for the prepared film (Figure (44)) are to be considered for two ranges of the

applied voltage: (i) 0–0.4 V and (ii) up to 20 V. The initial section (under V_a up to 0.4 V) is described by the function given below [4 and refs. therein]:

$$I_{theor}=I_s X A_{el} e N_1 \exp(-\Delta E_v/k_B T)(D_n/\tau_n)^{1/2}\exp[(eV_a/k_B T)-1], \qquad (61)$$

where N_1 is defined from the low frequency (f = 1 kHz) capacitance–voltage measurements. As the applied bias increases, the current is

$$I_{theor(2)}=I_{theor}\exp(-e\Delta_{tun}/k_B T), \qquad (62)$$

here $D_{tun} = I_{ZnTe} - I_{CdTe}$, I is the electronegativity of the corresponding compound.

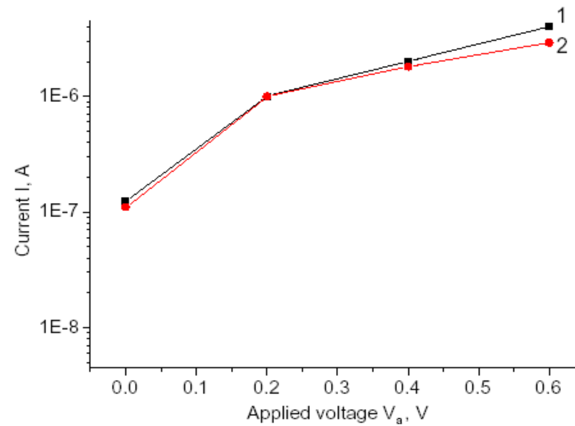

Figure 44. Results of numerical experiment for the *ZnCdHgTe* film (1 - experiment, 2 - theory) [4 and refs. therein].

For irradiated *ZnCdHgTe* .films the current observed experimentally may be written as follows [4 and refs. therein]:

$$j = j_0[\exp(eV_a/nk_B T) - 1] - j_{sc}, \qquad (63)$$

j_0 is a thermoemission current, and j_{sc} is the short circuit current. The open circuit voltage is [4 and fers. therein]

$$V_{oc} = (nk_BT/e)\ln[(j_{sc}/j_0)+1], \quad (64)$$

where $j_0 = A^*T^2exp(-e\varphi_b/k_BT)$ and $A^* = 4\pi m^*e(k_B)^2/\hbar^3$.

Results of the numerical simulation are plotted in the Figure (44) [4 and refs. therein]. In summary, monocrystalline thin films of the narrow-gap semiconductor *ZnCdHgTe* grown by the PLD technology at the first time are investigated. The room temperature electric studies (in particular, current–voltage measurements) revealed the diode-like characteristics. The additional photocurrent caused by noticeable light modulation of the minority charge carriers is observed under irradiation by the light source of 100 W power [4 and refs. therein].

Chapter 4

IMPROVING CONTACTS FOR HIGH-EFFECTIVE SOLAR CELLS

Manufacture of low-cost and reliable high-effective photovoltaic converters is still a challenge. Novel electrochemistry has developed unique methods not only for production of various oxide-semiconductor nanoscaled structures (among them TiO and ZnO), but also for fabrication of effective photovoltaic devices (for example, dye-sensitized solar cells). However, different chemical techniques (in particular, wet technology) based on intrinsic electrochemical processes in the components of the commercial silicon-based solar cells can significantly contribute to solution of the problem mentioned above. Chemical processes are widely employed in the fabrication of electrical contacts arranged at the irradiated surface of solar cells. Silver technology is extensively used in fabrication of silicon solar cells. The function of small particles employed in solar cells is described in [10–13]. Entering nanoparticles into the pores of photon absorbers enhances their efficiency. In this chapter we describe how, for the first time, copper clusters were chemically entered into the micropores of a silver contact. The clusters have affected the electrical properties of the contact; a dark current, which was previously unknown in the case of metals, has been revealed.

The main task of the metallization of electrical contacts for solar cells is the enhancement of its efficiency. It means that the transformation of the radiation energy supplied by our Sun is to be maximal, and the principal way for reaching this goal is lowering the

electrical resistance of the solar cell. To solve this problem we propose to fill in the pores of the silver electrical contact with micro(nano)clusters of silver or other metal. The working-out technology is to be commercially profitable and consistent with the common technology of silicon wafer based solar cells.

The manufacture of standard solar cells based on silicon wafers uses the silver paste in connection with porous printing. The paste film at the elevated temperatures is fired in the emitter layer through the antireflection coating. To provide the higher conductivity the contact stripes of 140 μm width are fabricated. It leads to the about 10% shadowing effect of the surface of the solar cell and, consequently, to the considerable losses of produced electrical current and efficiency of the cell. These effects can be eliminated by the very fine porous printing step with producing contact stripes of about 50 μm width and the following wet chemical deposition of metals as silver, gold and copper. This problem can be solved by the wet chemical current-free metal deposition with the rate of 1 mm/min under temperatures lower $70^{0}C$.

The suitable wet chemical solution is to have the following features:

- a high selectivity, e.g. the metal deposition is to be realized onto the front side of the solar cell and on the Al/Ag soldering pads of the back side only;
- the deposition of the metal on the antireflection coating as well as on the free silicon surface and Al-layer is forbidden;
- the contact structures prepared early by the porous printing of the silver paste are to be not damaged, i.e. the parasite deposition on the edges of the contacts has not exceed the 1.5-times magnified thickness value of the deposited metal layer;
- the contact resistance and the adhesiveness of the deposited contact are to be not affected;
- the process as a whole is to be environmentally friendly.

SOLAR CELL AS AN OBJECT OF INVESTIGATION

A solar cell based on the Si⟨P⟩/SiN_x/Si⟨B⟩-crystal silicon structure with an aluminum contact made on the backside of a wafer and with a front-mounted silver contact was taken as a matter for enquiry; the

silicon nitride layer was 70 nm thick. Some elements of the construction are presented in Figure 45.

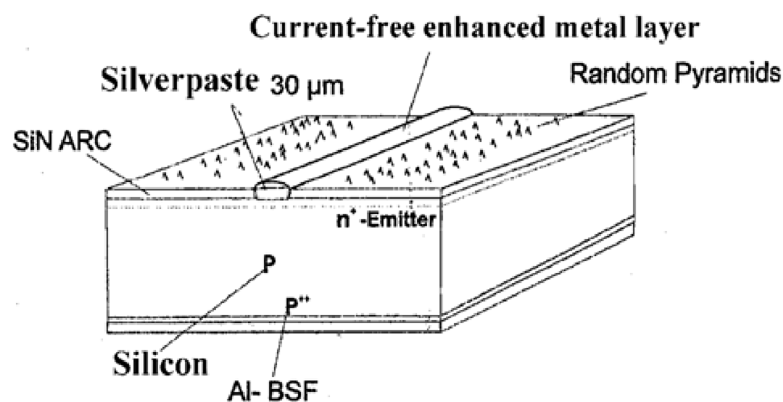

Figure 45. Face-side surface and cross sections of common silicon wafer solar cell.

A current-free enhanced metal layer serves as an electrical contact which represents a silver **s**tripe-**g**eometry **e**lement (further SGE) arranged at the silicon surface.

The silver paste produced by DuPont was taken as a source material for obtaining the contact; the paste was deposited onto a silicon surface through a tungsten net-shaped mask. When drying was completed, the organic components of the paste were burned out in an inert atmosphere at 820–960°C. At the same time, silver was burned in silicon through a 70-nm-thick silicon nitride SiN **a**nti**r**eflection **c**oating (ARC).

The crossed silver contacts on the surface of the silicon wafer are of two kinds (Figure 46). The narrow silver stripe is called “gird”, the wide one is called “busbar”.

After annealing, the electric contact gird is made up from the silver SGEs of 10–20 µm thickness and 120–130 µm width. The busbar has 1 mm width.

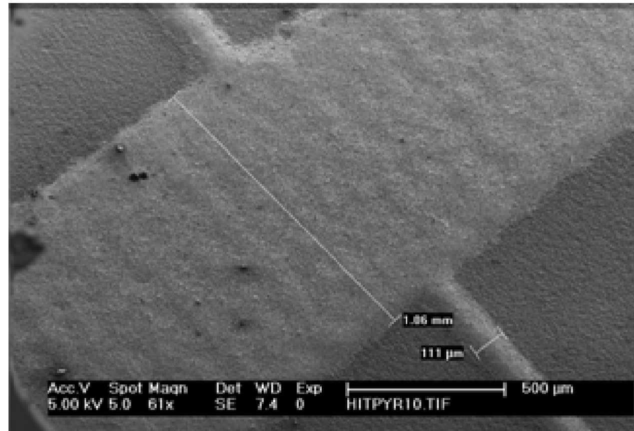

Figure 46. Electron-beam image of the SGE contact surface - the busbar and gird on the silicon wafer before the metal deposition. The width of the gird is 111 µm, the width of the busbar is no more than 1 mm (61× magnification).

The morphology of the surface of the solar cell and the contact strips before and after copper deposition was investigated with a KEYENCE-5000 3D optical microscope. Figure 48 presents the result of computer processing of images of layer-by-layer optical scanning of the silver contact surface.

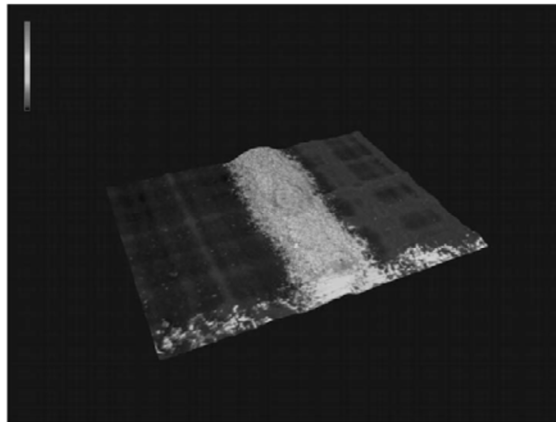

Figure 48. Grid-**c**ontact morphology optical scanning area 430x580 μm^2; magnification 5000x.

The porous structure of silver has been determined with the use of an electron microscope. The electron-beam image of the cleavage of a wafer with a SGE contact is shown in Figure 49. It can be seen that the silver SGE is not balk metal but a porous structure. Cavities are 1–2 μm in length. The electron-beam image of a contact SGE surface is shown in Figure 49, where numerous pores are visible; the pores have access to these cavities.

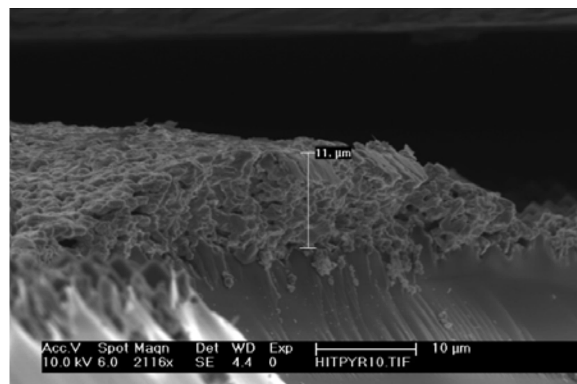

Figure 49. Electron-beam image of a cross-section of a contact SGE made of porous silver and a cleavage of silicon wafer. The SGE is 11 μm in height; 2116× magnification.

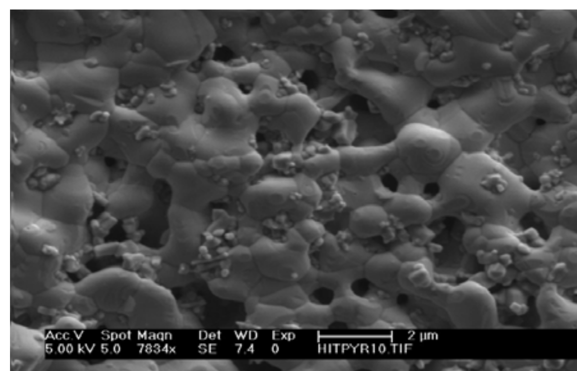

Figure 50. Electron-beam image of surface of the contact SGE made of silver on a wafer. The linear size of pores occurring in silver is under 1 μm; 7834× magnification.

The crystal structure of the metal phases was studied by grazing incidence X-ray diffraction (GIXRD). In a contact SGE 10 µm high and 120 µm wide, silver features the face-centered cubic structure referred to the *Fm3m* crystallographic space group of symmetry. The X-ray diffraction pattern obtained with the grazing incidence X-ray diffraction (GIXRD) technique is presented in Figure 52. The X-ray beam incidence angle was 2. For reference, the X-ray diffraction pattern of a silver structure is shown in the lower part of the figure. Single-crystal silicon wafers were aligned to (110). The associated X-ray diffraction peak with a significant half-width is shown in Figure 52.

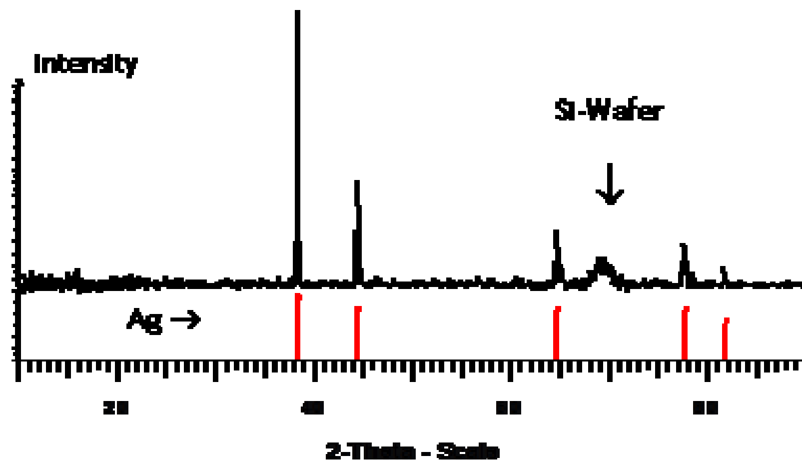

Figure 51. X-ray diffraction pattern of a silver contact SGE and a single-crystal silicon wafer.

The crystal structures of the electrical collector (busbar) and the contact on the back side of the wafer were examined by the GIXRD-technique. The X-ray diffraction pattern of a silver structure is shown in Figure 52. The silver features are demonstrated: the face-centered cubic structure referred to the *Fm3m* crystallographic space group of symmetry is shown in the lower part of the Figure 51. The dash diagram of the Pb crystalline structure is shown in Figure 52. As is seen, the contact contains some crystalline lead phases.

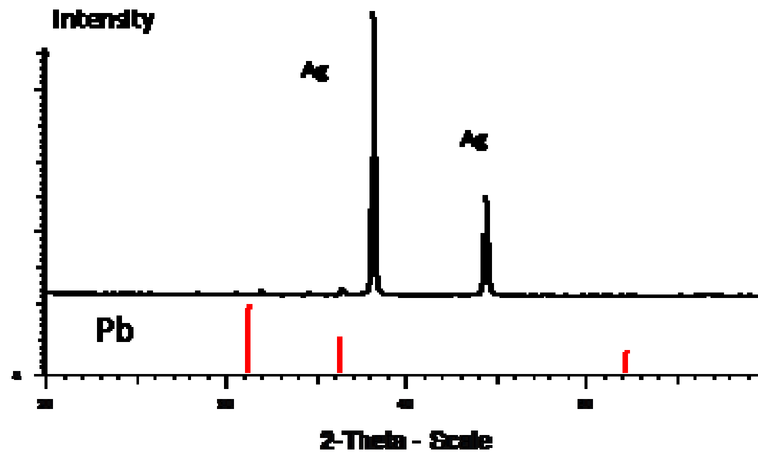

Figure 52. X-ray diffraction pattern of a silver contact SGE (of the busbar) and the back contact with the porous printing paste produced by DuPont. This pattern demonstrates presence of both metals: silver and lead.

Figure 53 shows the X-ray diffraction pattern of the back side of the silicon wafer with an Al-contact. The dash-diagrams of crystalline structures for lead and silicon are presented in the lower part of Figure 54. Its correspondence to the diffraction pattern indicates on the mixture of crystalline phases of Al and Pb.

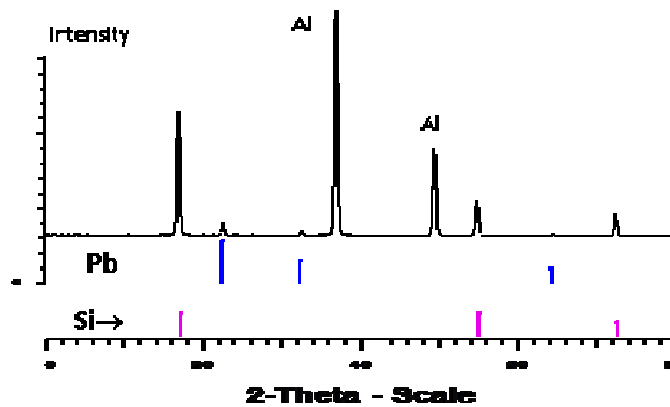

Figure 53. X-ray diffraction pattern of the back side Al-contact on the single-crystal silicon wafer.

At the next step we have analyzed the reference samples with the EDX-method. This technique allows analyzing the samples with two different values of the electron energy: the elemental analysis of the surface is made with 5 keV electron beam and the deeper layers were studied with the 25 keV electron beam. The next three pictures present the results.

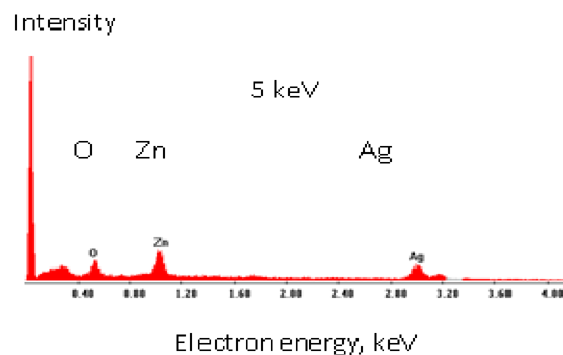

Figure 54. EDX is registered with the acceleration voltage of 5 keV. The Pb-contaning Ag-paste from DuPont is deposited on the surface. This experiment showed no lead on the surface of the sample. The presence of zinc is found out.

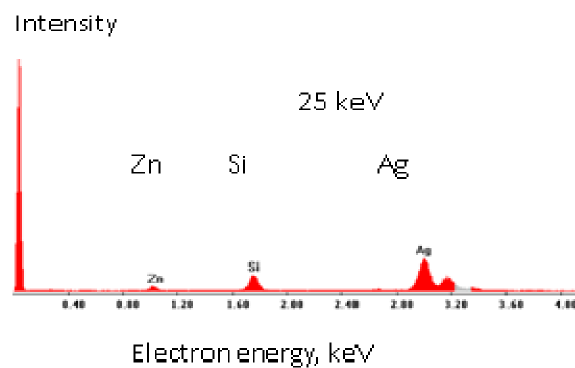

Figure 55. EDX registered with the acceleration voltage of 25 keV. The Ag-paste from DuPont is deposited on the surface. The deep regions of the surface are studied. The Si-peaks force us to conclude that we examine the wafer through the double metal layer. No lead is detected in the semiconductor part of the sample.

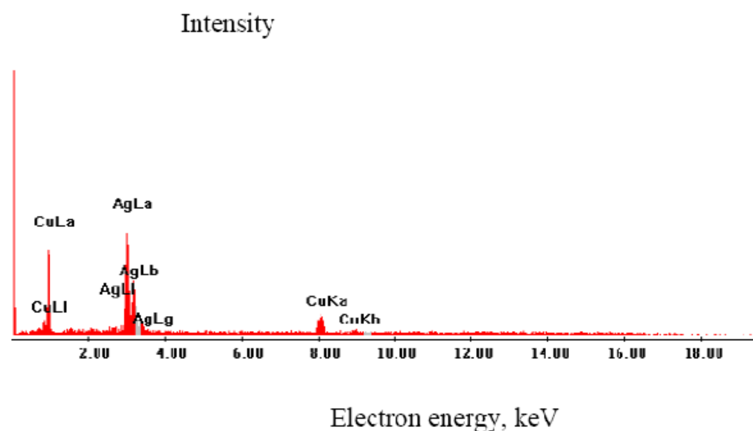

Figure 56. EDX results for electron beam with energy 0-20 keV.

Thus, the EDX study carried out with two different voltages showed that the Ag-paste contains no lead (K_{α} = 10.55 keV), zinc is registered in this paste. Furthermore, we can define the following properties of the reference sample:

- the grid and busbar contain Ag+Zn phase mixture;
- there is no crystalline Zn-phase in the Ag-paste, zinc is to be seemed as a doping agent only;
- polycrystalline lead is placed between the grid and the wafer;
- crystalline phases of Ag and Pb are mixed in the front and back side contacts;
- crystalline phases of Al and Pb are mixed in the backside layer;
- polycrystalline silicon is placed between the metal and Si-wafer;
- the Ag-layers have a porous structure.

Further we will use these results for building the chemical model and description of chemical reactions taking place in the reference sample.

CU-METALLISATION FROM WATER SOLUTION

The topic “Current-free deposition of copper on silicon, silver and aluminum surfaces” is almost not investigated. We have to note that:

- “copper is one of the most effective charge carrier lifetime killers in silicon” [10];
- “copper does not penetrate through the thin chromium diffusion barrier at low temperatures” [11];
- Ni-layer can serve as a protective coating for silicon against copper. The system „current-free Ni/Cu-halvanometallization of Si“ is now studied;
- organic salts are to be origins of metals Ag, Bi, Ti, Nb for the silicon metallization [12].

For Cu-deposition on silicon we have applied the following process [13]:

- Copper hexanoate → Cu + Cu_2O at 200^0C;
- Cu + Cu_2O + H_2 + N_2 → Cu (Metal) at 200^0C.

The current-free Cu-deposition on TiN/SiO_2/Si, WN/SiO_2/Si is carried out from organic solutions of copper sulfates with help of the following reagents [14]:

- EDTA – ethyldiaminotetraacetate;
- glyoxylic acid,
- 2,2-dipiridine,
- polyethylene glycol,
- tetramethylammonium hydroxide.

At the start of the process of Cu-deposition the electrical impuls is necessary. The parameters of the process are as follows: temperature 60-70^0C, time up to 15 min, thickness of the copper layer up to 0.5 μm, pH ~ 11.

The laser beam irradiation of the alkali Cu solution ($CuSO_4$ / H_3BO_3 / NaH_2PO_2) leads to the metal film deposition at the following parameters: pH 9.2/60^0C/60 min [15].

As is known [16], the firma SEG proposes the current-free Ni-deposition and electrochemical technology for copper: “It should be now be clear that a specification that calls for “ELECTROLESS NICKEL” is totally inadequate. There are “horses for courses” and without knowledge of what the deposit has to do, the finisher is operating completely in the dark.” Going back to the history of chemistry, we should refer the reader to some important facts: in old Egypt the Cu-covered mirrors were found out in the Pharaohs tombs. It also is known that in waters of many rivers in Altai Mountains (Russian Federation) iron precipitates were slowly covered by copper.

We also should to remember that Cu-containing systems are available in three solid phases: metal, oxide, and hydroxide. So, in the solution the following ions can be presented: Cu^{+}, Cu^{2+}, $HCuO_2^{-}$ und CuO_2^{2-}. Then the following reactions are possible:

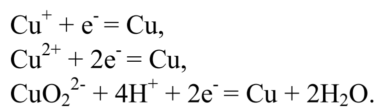

$$Cu^{+} + e^{-} = Cu,$$
$$Cu^{2+} + 2e^{-} = Cu,$$
$$CuO_2^{2-} + 4H^{+} + 2e^{-} = Cu + 2H_2O.$$

It is important that the value of the electrochemical potential of these reactions can be about zero. So, the wafers with contact stripes processed with porous printing technology have unavoidable micro-galvanic elemental pairs which are presenting immediately before the Cu-metallization. We suggest the potential difference of these elemental pairs is very low. Thanking to this minimal value of the potential difference the Cu-deposition on the silver contact stripes is possible without applying additional electrical potential.

To conclusion we have to note that the current-free Cu-deposition is possible without any additional conditions.

Now we briefly consider the most important requests for the metallization processes:

- selectivity of the metallization,
- high adhesion of the substrate,
- advantages compared to commercial baths,
- compatibility with industrial end-processes and materials.

The technological requests for the Cu-metallization are as follows:

- cyanide-free solutions,
- deposition rates of the materials used in the process are to be about 1 μm/min,
- the temperatures in the technological chamber are to be about 40-60^{0}C,
- using the most common (not rare components and compounds) materials in order to keep the cheapest process prices.

Let us consider the special requests:

- the material can be deposited only on the surface with contacts previosly fabricated by the porous printing technique. The ARC-covered front side is not to be covered with any film;
- the long stability of the process;
- save and reliable recycling of the components after the process finishing.

EXPERIMENTAL CU-METALLIZATION

Objects of investigations are the structures with 125x125 and 156x156 mm^2 active area (solar cells) with contacts on the front side and back side, ARC-layers and edges, different porous printing stripes, Al- and Ag-pastes, single crystal and polycrystalline Si wafers. The principal chemical reagent is inorganic Cu-containing salt with 35.3% Cu-content. The experiments were carried out with following copper-containing solutions:

solution 1: 1.0 g Cu / 100 ml H_2O,
solution 2: 0.5 g Cu / 100 ml H_2O,
solution 3: 0.2 g Cu / 100 ml H_2O,
solution 4: 2.0 g Cu / 100 ml H_2O,
solution 5: 5.0 g Cu / 100 ml H_2O.

These solutions have various reaction speeds.

The Cu-containing solution after Cu-metallization was examined by the means of chemical analysis. The aim of this analysis was to establish how silver dissolves from the solution. The analytical method is based on the fact that following reaction is possible:

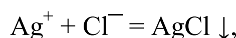

$Ag^{+} + Cl^{-} = AgCl\downarrow$,

and we have obtained the following:

i) AgCl is not found in the solution for metallization; ii) while the metallization of the busbar and contacts takes place no exchange reaction between Cu and Ag is registered; iii) copper covers silver. Thus, copper covers silver without chemical reaction between the metals.

Crystalline copper clusters were deposited from aqueous solutions; they penetrated into pores and covered the silver contact SGE surface of a silicon solar cell. The deposition time varied within 160 min.

The morphology of the surface of the solar cells before and after Cu-deposition was investigated by scanning electron microscope. Results are illustrated in Figures 46, 50. As is seen, all structures have the porous silver surface layer.

The surface structure after the porous printing before the metallization is shown in Figure 46. The electron-beam image of the surface of a silver contact SGE with copper deposited is presented in Figure 57. This electron-beam image of the surface of a silver contact SGE was obtained on a wafer after 5 min copper deposition. As shown in Figure 57, copper particles are smaller than 0.1 μm and smaller than the pore diameter in silver.

Comparison between the initial porous printed surface (Figure 46) and the same surface after the Cu-deposition from the solution (Figure 57) shows the fine porous film on the porous printed layer. We have suggested that the pores in the Ag-surface prepared by the porous printing are filled in with Cu particles.

Comparing this picture with Figure 46, one also can conclude that copper particles are evenly distributed over the silver SGE. The copper particle size is below the pore diameter: copper penetrates into cavities of silver. The initial section of the curve shown in Figure 58-60 corresponds to the partial filling of the silver pores.

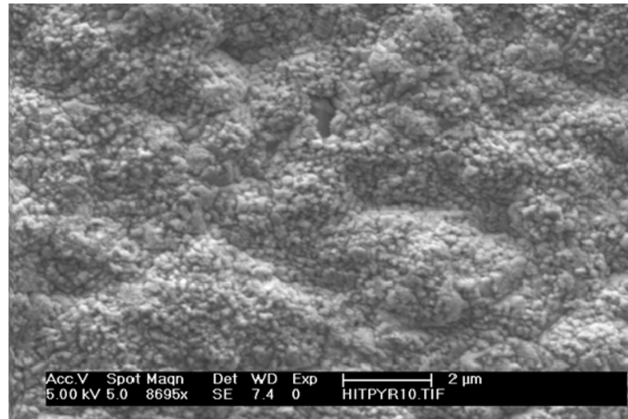

Figure 57. The surface structure after the 5 min Cu-deposition. 8695× magnification.

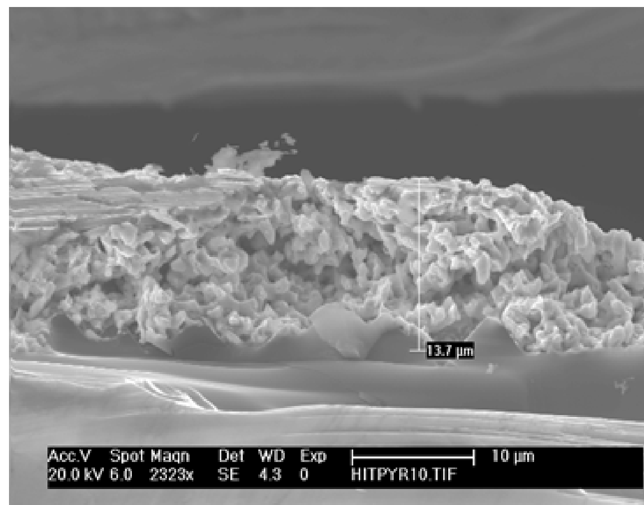

Figure 58. Electron-beam image of cross sectional cleavage of a silver contact SGE obtained on a wafer after 5 min copper deposition. The thickness is 13.7 µm and it has increased up to 37 %.

The deposited copper features a cubic face-centered crystal structure with F*m*3*m* crystallographic point group of symmetry. For a contact SGE with a copper coating, an X-ray diffraction pattern with peaks of maximum intensity is shown in Figure 60. As it can be seen, the copper

reflections show an increase in the intensity with deposition time. Their intensities are compared in Figure 61. It is noted that the intensity ratio steadily grows for 40 min. This means that the copper deposition rate is held constant for this period. The deposition rate decreases when copper has filled silver cavities; then, after 90 min, the copper deposition is essentially brought to completion.

The morphology of the solar cell surface and contact SGEs were investigated before and after the deposition of copper with the use of a KEYENCE-5000 optical scanning microscope. The computer image processing of the data on the in-layers optical scanning of the surface obtained before and after the deposition gives the results presented in Figure 61. The copper deposition onto silver SGE leaves the contact form and profile unchanged; the contact profile alone consists of regularly alternating thicker parts and contractions of a contact SGE. The difference in the height and width ranges up to 5 µm. In some instances, the thin copper layers were responsible for a modest size contraction throughout the height of the contact. It was found that, when copper layers up to 1 µm thick are deposited on a silver contact, they are able to initiate the thinning out of an SGE up to 10%.

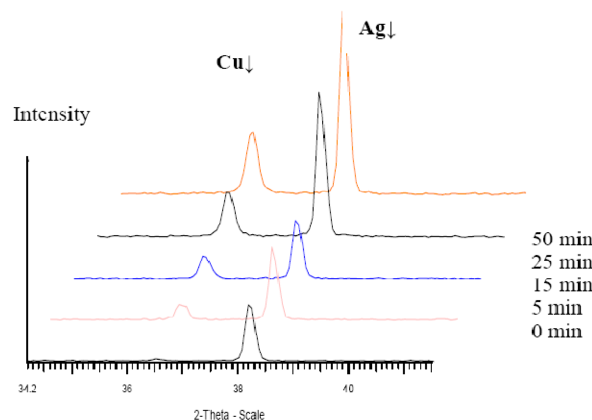

Figure 59. X-ray diffraction pattern of a silver contact SGE obtained before and after copper deposition.

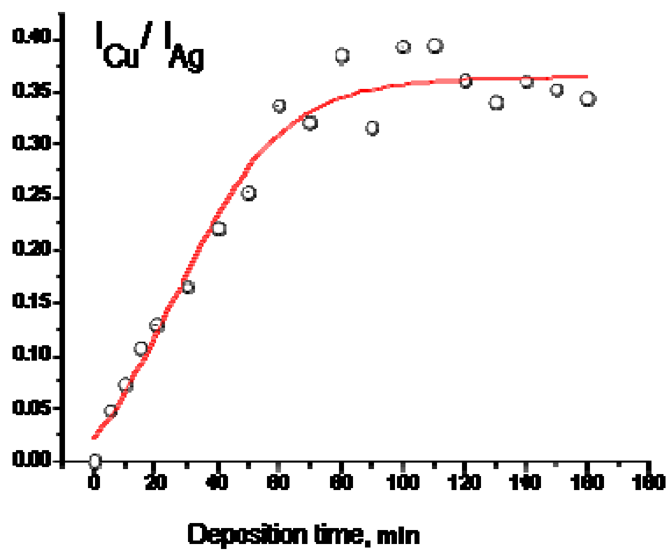

Figure 60. Copper-to-silver peak intensity ratio depending on the deposition time.

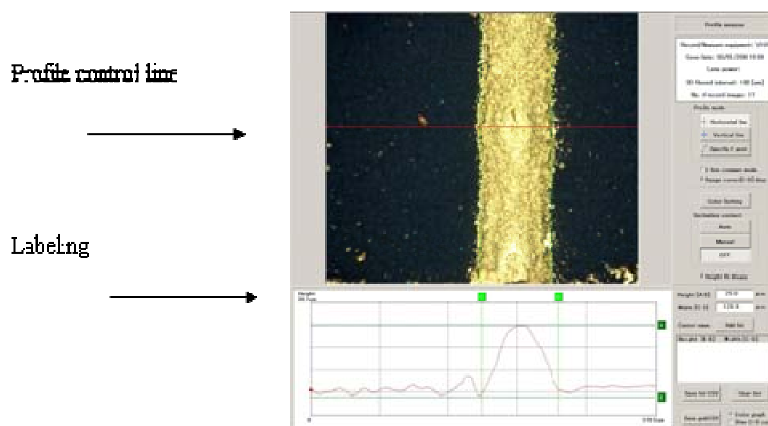

Figure 61. Test record sheet on the imaging of the silver contact SGE with the use of a scanning optic microscope. The SGE is 25.0 μm in height and 129 μm in width.

The electron-beam image of the cleaved facet of a silicon wafer with a contact SGE obtained with the copper deposition is given in Figure 63. It is easily seen that the silver SGE remained a porous body. The SGE thickness grew up to 17.8 μm.

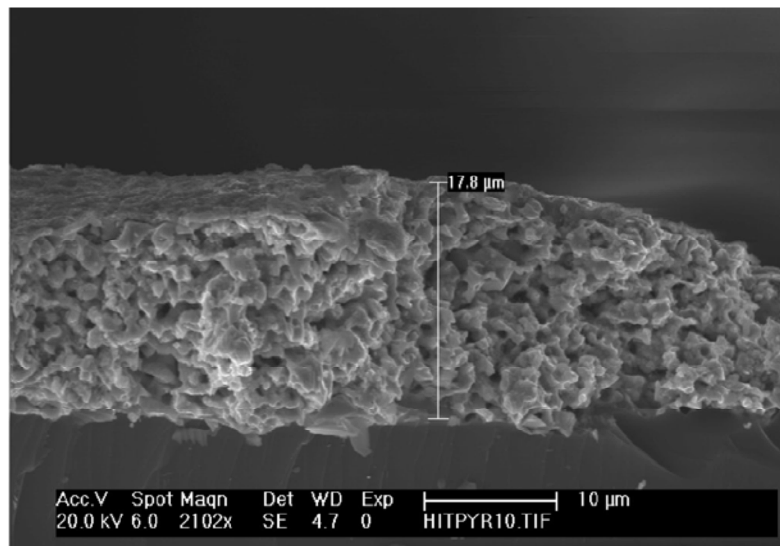

Figure 62. Electron beam image of cross sectional cleavage of contact SGE made of silver on a wafer after 15 min copper deposition. The SGE is 17.8 μm in height; 2102× magnification, the pore diameter in silver is 1-2 μm; 8695× magnification.

The chemical composition of the contact and the copper distribution over the contact depth were investigated by energy dispersive X-ray (EDX) analysis, secondary ion mass spectrometry (SIMS), and X-ray photoelectron spectrometry (XPS). It was found that the copper composition in the silver pores declines with the contact depth. Copper was detected at the silicon–silver interface. Copper diffusion in the silicon escaped detection.

To examine the material properties of the contacts we have used the EDX-method (Figure 63).

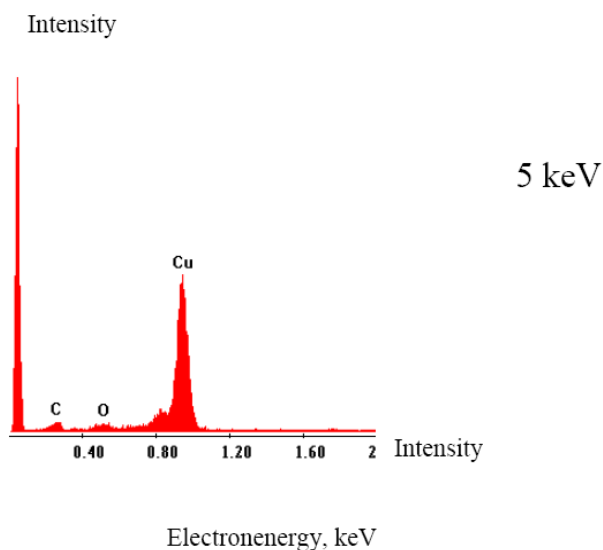

Figure 63. EDX-Analysis with 5 keV. As is seen, copper (but not silver) is placed on the surface.

As we can see on the Figures 63, 64, on the surface of the contact only copper is registered. We note that the thickness of the copper layer cannot be measured by the EDX method.

Now we would like to describe our observations of changes taking place in profiles of the finger contacts and busbar under the Cu-metallization from water solutions without external electrical field. The parts of the standard solar cells with dimensions 125x125 and 156x156 mm^2 were chosen as objects of examination. The deposition area did not exceed 15 cm^2.

The process of the Cu-metallization was carried out at the room temperature. The samples were placed in the glass cuvette of 180 mm height and 1 l volume. The cuvette was filled in with 1.4 g/l Cu-acetic acid solution and 0.02N catalyst concentration. The time of the copper deposition was 5 min.

Figure 64. EDX-analysis using the electron beam with 20 keV energy. The deep layers of the sample are also investigated. The additional Ag-signal is registered.

The next important question is the uniformity of the copper layer. We have studied the solar cells which were stored during various times after the screen printing (contact finger fabrication, the paste annealing was performed in the temperature range 810-960^{0}C) and the chemical bath (Cu-metallization of these contacts). First of all, we have to observe how uniform will be the copper layer produced by the metallization performed immediately after screen printing and paste etching. At the same time, we have found that the solar cells stored 6 months after the screen printing had poor copper covering (only at the edges of the grid), and in the middle of the solar cell we also had seen no Cu layer. How one can explain this fact? We suppose the center of the solar cell has lower potential compared with the outside section of the cell. Why? Because the edge of the solar cell has got higher potential after the chemical bath than the area in the middle of the cell because the electromagnetic field is larger on the edges than that in the central part of the solar cell.

Besides that, the Ag-contacts have various widths (from 80 µm to 120 µm). Our studies showed that the more slim contacts had larger Cu-covering ratio.

Many Ag-pastes contain lead (Pb) as a component. We have checked the possible effect of lead on the formation of Cu layer on the silver contacts. Our investigations have showed no difference between

metallization results for Ag-contacts fabricated by using the Pb-free pastes and lead-containing ones.

We also have examined the uniformity of copper layer deposited on silver contacts immediately after the paste annealing and after 1 day storage of the industrially fabricated solar cells. The copper layer was completely uniform in the first case. For the set of the samples stored 24 hours we have registered lowering Cu-deposition rate only for two samples, for other 98 structures we have observed no changes either in uniformity of the copper layer or the rate of Cu deposition. Thus, we can conclude that the "fresh" samples (with storage times no more than 24 h) are the most suitable objects for Cu-metallization in sense of the layer uniformity and deposition rate.

The next stage of our experiments was studying the contact profiles before and after the metallization. DEKTAK measurement unit gave us a possibility to define the width and height of the contact fingers and, consequently, to calculate the cross section of the contacts. We have chosen two sets of the solar cells with various pastes:

- solar cells from the set1: silver-containing paste DuPont with lead and DuPont Al-containing paste with lead,
- solar cells from the set2: silver-containing paste DuPont with lead and Heraeus Al-containing paste with lead.

Tables 12 - 13 and Figures 65-66 illustrate the results. The statistical working-out was carried out for each experimental point (10 measurements for the each point). The DEKTAK software allowed us to estimate the geometrical parameters of the Ag-finger contacts.

What did we obtain? Let us to analyze the experimental results. First of all, we see the sufficient mean variation of the geometrical parameters of the contact fingers. The height of the fingers produced with using DuPont paste is varied between 11.1 μm and 17.1 μm. The statistically estimated mean value is about 14.0±1.6 μm. The cross section of the fingers is in the range from 534 to 1665 μm^2, the mean value is 1234±242 μm^2. The width of the contact finger is 125±3.5 μm.

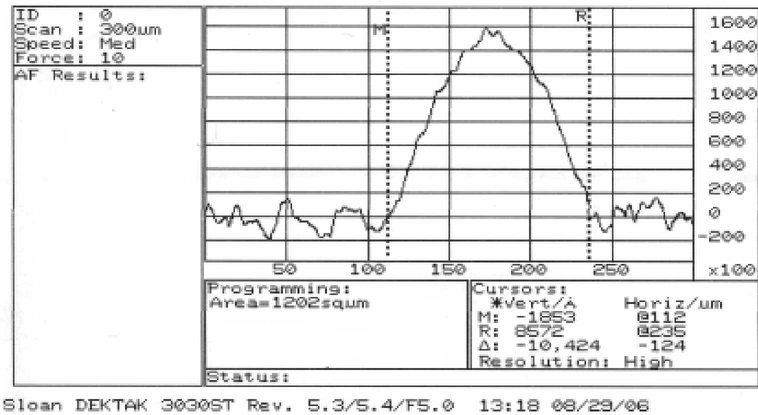

Figure 65. Profile scan of the contact finger without copper. The height of the finger is 15.7 μm; its width is 124 μm.

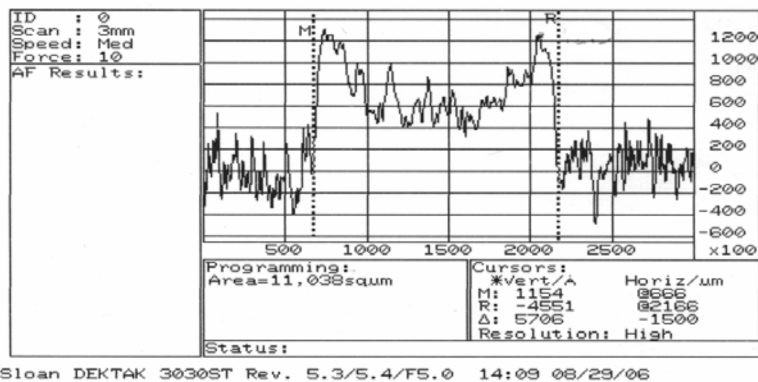

Figure 66. Profile scan of the contact busbar without copper. The busbar height is 12.3 μm, its width is 1.50 mm.

The similar statistical estimation was carried out for the height and cross section of the busbar. It was found that the height of the contact finger is 6.62±16.6 μm with the mean value of 12.5±1.5 μm (8 measurements for each point). The cross section value changes from 6913 to 13972 μm^2. The width of the contact finger is estimated to be 151±0.02 μm.

The analysis of the geometry of contact fingers showed no changes for narrow and wide contacts after the cu-metallization. The statistical dispersion of the contact parameters after the metallization has lowered. For example, the height of the finger has been decreased from 1.6 to 1.0 μm. The range of the cross section values for narrow contacts changed from 242 to 167 μm^2 and for the busbar this value decreased from 4800 to 2400 μm^2.

Table 12. Changes of width and thickness of the finger and busbar before and after Cu-metallization for the samples from the Set 1

Property	**Finger**		**Busbar**	
	Reference	**after Cu-deposition**	**Reference**	**after Cu-deposition**
Height, μm	14.0 ± 1.6	16.5 ± 1.0	12.5 ± 1.5	16.6 ± 1.8
Δ, %	2.5 μm or 18 %		4.1 μm or 33 %	
Width, μm	125 ± 3.5	138 ± 7.2	1510 ± 20	1510 ± 30
Δ, %	8 μm or 10 %		0	
Cross-section, μm^2 μm^2	1234 ± 242	1519 ± 167	8500 ± 4800	13700 ± 2400
Δ, %	285 μm^2 or 23 %		5200 μm^2 or 61 %	

Table 13. Changes of width and thickness of the finger and busbar before and after Cu-metallization for the samples from the set 2

Property	**Finger**		**Busbar**	
	Reference	**after Cu-deposition**	**Reference**	**after Cu-deposition**
Height, μm	9.75 ±1.22	12.2 ± 1.8	12.6 ± 1.2	14.0 ± 1.0
Δ, %	2.45 μm or 25 %		1.4 μm or 11 %	
Width, μm	114 ± 6	139 ± 17	1500 ±10	1530 ±20
Δ, %	24 μm or 21 %		30 μm or 2 %	
Cross-section, μm^2	746 ± 154	1110 ± 180	11800 ± 1700	13900 ± 1400
Δ, %	364 μm^2 or 49 %		2100 μm^2 or 18 %	

As is seen, the height and width of the contact finger are increased: 33% and 21%, respectively. The cross section of narrow contact fingers after the Cu-metallization was increased in about 49% and that of the busbar up to 61%. We should note that the aim of metallization carried out for the contact fingers is lowering of the specific resistance. The expression for calculating specific resistivity includes the cross section value. It is impossible to estimate the efficiency of the contact metallization using the width and height of the copper layer. Our experiments showed the 60% effective increase of the cross section surface of the contact finger. It means that the Cu-metallization may enhance the efficiency of common solar cells. However, it is important to know: is there a possibility to decrease the contact surface without minimizing the cross section surface of the contact finger after the Cu-metallization? To answer this question we had performed the profile measurements of the contact fingers using the DEKTAK profilometer. The results are plotted in Figures 65-67.

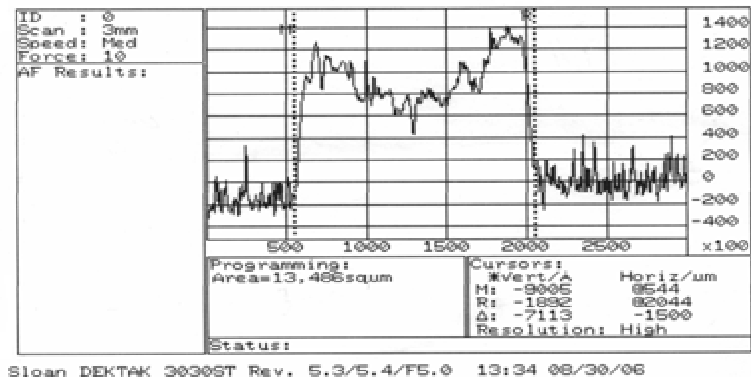

Figure 67. Profile scan of the busbar contact after Cu-deposition. The busbar height is 14.7 μm, the width is 1.50 mm.

It is seen that the contact height of the sample from the set 1 increases and its width decreases after Cu-metallization. The same dependence is observed for the samples from the set 2. Figures 67- 68 show that the profile and height as well as the cross section of the plateau have been changed. Figure 69 demonstrates that the cross section of the plateau is changed after the Cu-deposition. This feature of the process

allows us keeping the contact cross section regardless minimizing its width. Arrows in Figure 70 point out that the cross section is kept (12000 μm^2) without changes, and at the same time the busbar width has decreased from 1.50 mm to 0.87 mm.

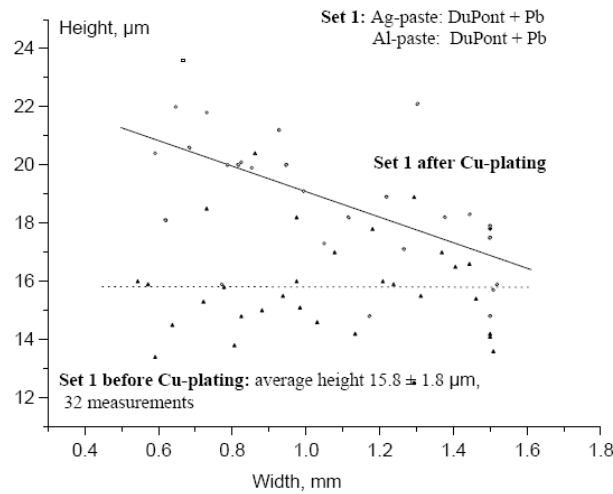

Figure 68. Busbar height as a dependence of the width of the busbar before and after metallization (set1).

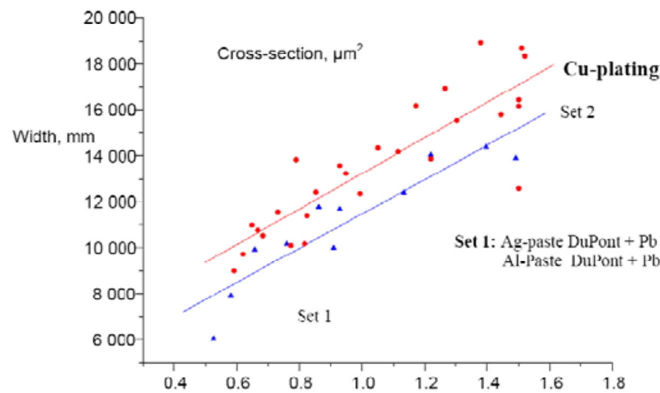

Figure 69. Busbar cross sections of samples from the set1 and set 2 after Cu-metallization.

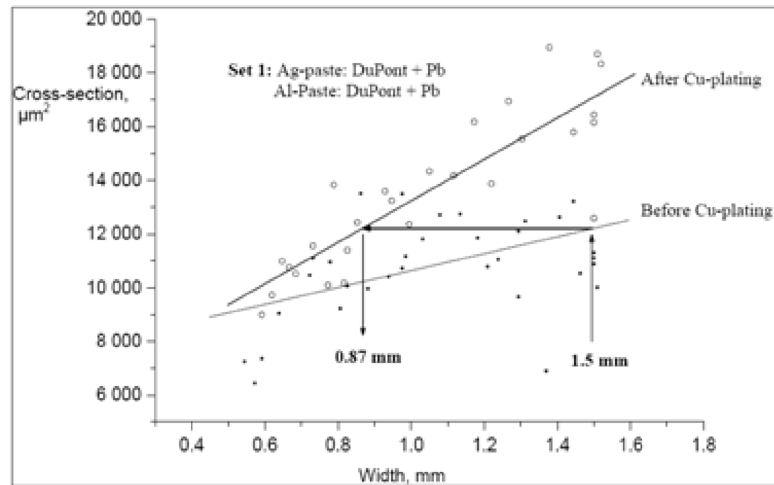

Figure 70. Busbar cross-sections of the samples of set 1 before and after Cu-metallization.

The resistivity of the contacts was measured at room temperature with the use of a Keithley 236 two-probe conventional meter. As shown in Figure 71, two measuring probes were arranged at the contact SGEs which were 8 mm apart. The probe consists of a tungsten needle with a point 120 μm in diameter (Figure 72). The measurements were performed for two specimens placed in a box with black walls and a solar simulator. The experimental results are presented in Figure 74.

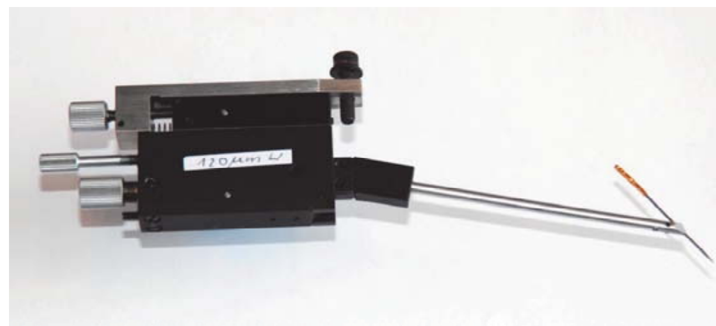

Figure 71. Tungsten measuring needle arranged in a holder and shown at the right of the figure.

Figure 72. The point of tungsten needle seen through an optical scanning microscope. The point is 120 μm in diameter; 5000× magnification.

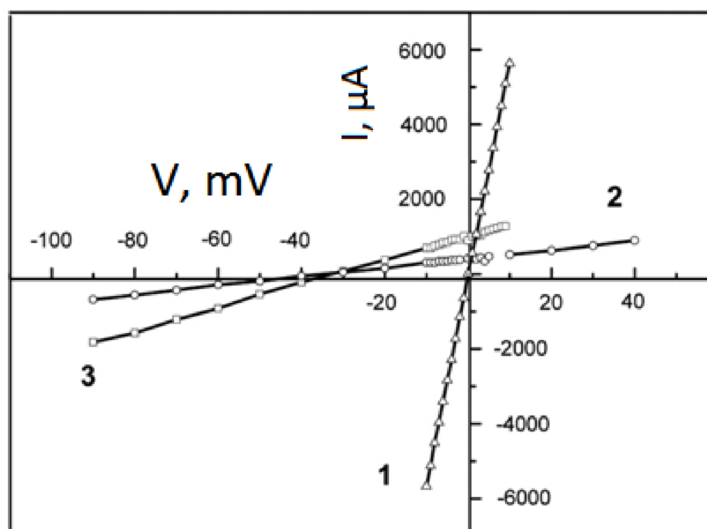

Figure 73. Current–voltage dependences for (1) a contact SGE made of silver, (2) a contact SGE with copper clusters positioned in the silver pores, and (3) SGE with a copper layer positioned on the surface and with copper clusters positioned in the silver pores.

Curve 1 is the current–voltage dependence for the initial silver contact SGEs arranged at a wafer surface. Other curves in Figure 73 are the current–voltage dependences for contacts obtained after copper deposition. All the curves support the metallic conduction of the contact SGEs. The distinction between them resides in the fact that, in the case of contacts with copper clusters, these curves do not pass through the origin for either the forward current or for the back one. The phenomenon of a current flowing through a metal in the absence of an applied electric field is not outlined in the literature. In our experiment, the luminous current of 450 μA flows along the contact with copper clusters disposed only in silver pores and that of 900 μA flows along the contact with copper clusters disposed in the pores and at the silver surface.

Of fundamental importance is the fact that, in the absence of an applied electric field, the electric current continues to flow along the same samples when a solar simulator was taken out of service. The luminous and dark currents flowing along the contact SGEs are presented in Figure 74. As can be seen, under the zero bias, in the case of darkness, the generation of charge carriers is kept constant in the duration of the experiment. In the silver contact, the dark current is associated with charge carriers generated in the contact itself. The silver clusters positioned in pores and at the silver surface serve as a source of charge carriers for the dark current.

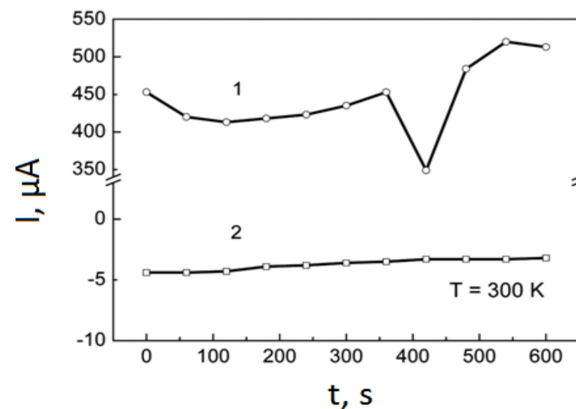

Figure 74. Time dependencies of dark and luminous currents in the absence of applied bias at contact SGEs with copper clusters positioned in silver pores.

As we have shown previously [22], the first attempting for explanation is to consider a Si-based p-n-junction with Ag/Cu-contacts with different heights of barriers formed at the metal-semiconductor interfaces: $¢_{Beff}$ = $¢_{Bn}$ + $¢_{Bp}$ ~ 0.05 eV (this value characterizes the effective barrier heights for electrons and holes, respectively) [22 and Refs. therein] and, on the other side, the barrier may be formed due to the difference of work functions of the contact metals: $\varphi_B = \varphi_{Cu} - \varphi_{Ag} = 0.17$ eV [22 and Refs .therein]. Remembering how the solar cell operates (under illumination the device harvests generated carriers and in darkness our active element produces practically no work, therefore, it should be no current!), we tried to calculate possible currents according to the 9999semi-classical theory of semiconductor devices [22 and Refs. therein]:

$$I_{Cu} = A_{el} A^{**} T^2 T_{tun} \exp(-e\phi_{Beff} / k_B T) \exp(eV_a / k_B T), \quad (65)$$

where I_{Cu} denotes the current producing by illumination of the sample where Cu-atoms are in Ag-pores and on the surface of the Ag-finger, A_{el} is an electrical area of the contact, A** is the effective Richardson constant, T_{tun} is a coefficient of the barrier tunneling transparency, k_B is the Boltzmann constant, V_a is an applied voltage.

What can we obtain for a dark current, when only the deformation of clusters in the contact stripe due to difference between the lattice constants of silver and copper can change the work function and the barrier height, respectively? The expression is as follows:

$$I_{Cu1} = A_{el} A^{**} T^2 T_{tun} \exp(-e\phi_{B1f} / k_B T) \exp(eV_a / k_B T), \quad (66)$$

where I_{Cu1} denotes the current observed under illumination of the sample with cu-atom in Ag-pores of the Ag-finger only; we should note that values of the tunneling transparency coefficient are in the range 10^{-7} – 10^{-5} (they are determined numerically basing on the experimental data). Figures 75 and 76 show results of the numerical experiment.

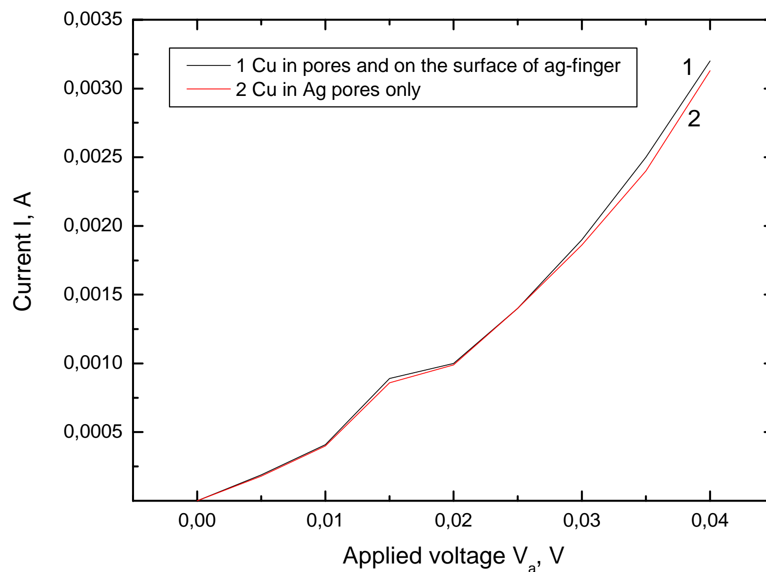

Figure 75. Current-voltage characteristics (numerical experiment!) of the Cu/Ag-cluster contacts of the Si-based solar cell: the calculation is performed according to the expressions (68)-(69) and represents the “forward” sections of the experimental dependencies.

As one can see, the numerical experiment performed in the region of very small applied bias (up to 40 mV) produces only a qualitative agreement with the measurements. First, there is no a “solar-cell feature” (calculated IVCs are beginning from zero unlike that of the illuminated solar cells), second, the values of experimental and calculated currents are also different. The semi-classical approximation (we introduced it by using the tunneling transparency coefficient) does not take into account all features of the conductivity of nanoscaled cluster structures. Before we discuss the further results we would like to say some words about current-voltage dependencies of nanostructures. The overlap energy between different sites is related to the width of the energy bands. The second factor is disorder-induced broadening of the energy levels. If the ratio of these values is small, it is hard to match the width of the energy level on one site with that of a neighboring site to that the allowed energies do not overlap and there is no appreciable conductivity through the sample. On the other hand, if the ratio is large, the energy levels

easily overlap and we have bands of allowed energy, so that there are extended wave functions and a large conductance through the sample [22 and Refs. therein].

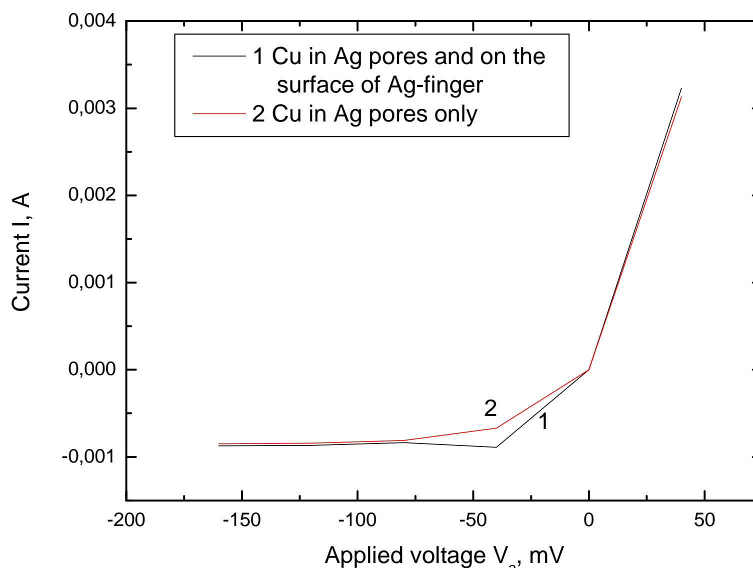

Figure 76. Current-voltage characteristics (numerical experiment!) of the Cu/Ag-cluster contacts of the Si-based solar cell: the calculation is performed according to the expressions (1)-(2) and represents both sections of the experimental dependencies.

The current flowing along a silver contact with copper clusters is induced by charge carriers generated in the semiconductor section of the wafer when the solar cell is illuminated. The density of carriers generated within the *p*–*n* junction is two orders of magnitude higher than that which occurred in the copper clusters, because the luminous current is two orders of magnitude larger than the dark one (Figure 76).

Depositing copper onto silver does not result in the formation of the silver–copper solid solution. The contact between the crystal structures assures the electrical potential difference. The difference is inadequate to generate current carriers. However, the contact between the silver–copper crystal structures may result in the compressive deformation of a metallic SGE and in a decrease in the electron work function for copper clusters.

We suppose that, in darkness, charge carriers generated by copper clusters within a contact SGE, which is the component part of the solar cell, are governed by the deformation of the SGE [15]. It is known [16] that the deformation of metal cluster structures may result in high temperature superconductivity.

In summary, the conversion of the solar energy is widely used in the production of electric power. In regular and industrial units, its efficiency depends on the grade of the component base [17]. As revealed hear, the dark current flowing along the silver contact arranged at the illuminated side of a silicon element makes it possible to produce additional electricity in amount of 5% of the averaged "light" value. Therefore, even with no changes in the semiconductor part of any solar cell, the efficiency of the solar energy conversion will be elevated when the copper–silver contacts are used in these units.

We have presented the method of metallization for silver contacts used under fabrication of commercial silicon wafer-based solar cells. This technique is applicable for covering the silver contacts with Ni, Sn, other metals and their mixture layers.

REFERENCES

[1] Yu.P. Gnatenko, P.M. Bukivskij, A.S. Opanasyuk, D.I. Kurbatov, M.M. Kolesnyk, V.V. Kosyak, H. Khlyap. Low-temperature photoluminescence of II–VI films obtained by close-spaced vacuum sublimation, Journal of Luminescence 132 (2012) 2885–2888.

[2] Kurbatov, D., Opanasyuk, A., Sofronov, D. and Khlyap, H. (2013), Structural and optical properties of vacuum-deposited ZnS nanostructures. Phys. Status Solidi A210, No.2, 291-296 (doi: 10.1002/pssa.201228499).

[3] D.I. Kurbatov, O.V. Klymov, A.S. Opanasyuk, A.G. Ponomarev, P.M. Fochuk, H.M. Khlyap. Structural characteristics of $Zn_{1-x}Mn_xTe$ polycrystalline films. Proc. of SPIE Vol. 8507 85071J-1, 2012.

[4] H. Khlyap, Physics and Technology of Semiconductor Thin Film-Based Active Elements and Devices. Bentham Science Publishers Ltd., 2009, 127 pp. eISBN: 978-1-60805-021-5.

[5] T.V. Kozar', N.A. Karapuzova, G.V. Laptev, V.I. Laptev, G.M. Khlyap, O.V. Demicheva, A.G. Tomishko, A.M. Alekseev. Nanotechnologies in Russia, 2010, Vol. 5, Nos. 7–8, pp. 549–553. © Pleiades Publishing, Ltd., 2010. Original Russian Text © T.V. Kozar', N.A. Karapuzova, G.V. Laptev, V.I. Laptev, G.M. Khlyap, O.V. Demicheva, A.G. Tomishko, A.M. Alekseev, 2010, published in Rossiiskie nanotekhnologii, 2010, Vol. 5, No. 7–8.

[6] V. I. Laptev, O. V. Demicheva. Patent of Russian Federation No. 2443037.

[7] V. I. Laptev, O. V. Demicheva. Patent of Russian Federation No. 104775.

[8] T.V. Kozar', N.A. Karapuzova, G.V. Laptev, V.I. Laptev, G.M. Khlyap, O.V. Demicheva, A.G. Tomishko, A.M. Alekseev. Nanotechnologies in Russia, 2010, Vol. 5, Nos. 7–8, pp. 549–553. © Pleiades Publishing, Ltd., 2010. Original Russian Text © T.V. Kozar', N.A. Karapuzova, G.V. Laptev, V.I. Laptev, G.M. Khlyap, O.V. Demicheva, A.G. Tomishko, A.M. Alekseev, 2010, published in Rossiiskie nanotekhnologii, 2010, Vol. 5, No. 7–8.

[9] V. I. Laptev and H. M. Khlyap*, Doklady Physical Chemistry, 2009, Vol. 424, Part 2, pp. 40–42.*

[10] M. A. Greenwood, "Solar Cells, Array Films Constructed from Nanotubes," Photonics Spectra 41 (9), 114–116 (2007).

[11] S. Pillai, K. R. Catchpole, T. Trupke, and M. A. Green, "Surface Plasmon Enhanced Silicon Solar Cells, "J. Appl. Phys. 101 (9), 093105.1–093 105.8 (2007).

[12] H. Han, U. Bach, Y._B. Cheng, and R. A. Caruso, "Increased Nanopore Filling: Effect on Monolithic All Solid State Dye Sensitized Solar Cell," Appl. Phys. Lett. 90 (21), 213510.1–213510.3 (2007).

[13] D. C. Johnson, L. M. Ballard, K. W. J. Barnham, J. P. Connolly, M. Mazzer, A. Bessiere, C. Calder, G. Hill, and J. S. Roberts, "Observation of Photon Recycling in Strain Balanced Quantum Well Solar Cells," Appl. Phys. Lett. 90 (21), 213505.1–213 505.3 (2007).

[14] S .J. Pearton, J. W. Corbett and T. S. Shi. Appl. Phys. A 43,153-198, (1987)

[15] J. Härkönen, et al. 26th PVSC; Sept. 30-Oct.3, 163-165, (1997)

[16] E. J. Lee, D. S. Kim, S. H. Lee. Solar Energy Materials & Solar Cells, 74, 65-70,(2002)

[17] K. F. Teng, R. W. Vest. IEEE Transactions on component, hybrids, and manufacturing technology. Vol. 11. N.3. 291-297, (1988)

[18] C. M. Hong, S. Wagner. IEEE Electron device letters, Vol.21.No.8, 384-386, (2000).

[19] Z. Wang. T. Ida, H. Sakaue, S. Shingubara, und T. Takahagi. Electrochemical and Solid-State Letters, 6 (3), C38-C41,(2003)

[20] S. Z. Chu, M. Sakairi, und H. Takahashi. J. Electrochem. Soc. 147 (4), 1423-434, (2000)

[21] http://www.secfinishes.co.uk
[22] Laptev V. I., Khlyap H. High-effective solar energy conversion: thermodynamics, crystallography and clusters. In: Solar Cell Research Progress (Ed. Josef A. Carson), Nova Science Publishers, New York, 2008. Pp. 181-204.

INDEX

A

accelerator, 25
access, 101
accounting, 82
acetic acid, 114
acid, 106
adhesion, 107
aluminum surface, 106
annealing, 99, 115, 116
aqueous solutions, 109
ARC, 99, 108
argon, 4, 5
atmosphere, 99
atoms, 5, 7, 8, 19, 23, 28, 31, 73, 124

B

band gap, 5, 8, 24, 67, 81
bandgap, 43, 57
barriers, 54, 70, 124
base, 12, 13, 63, 92, 127
baths, 107
bending, 42, 43
bias, 35, 48, 68, 69, 71, 72, 78, 79, 81, 88, 90, 91, 93, 95, 123, 125
binding energy(s), 7, 8, 9
Boltzmann constant, 71, 124
bonds, 47, 65, 66

C

cadmium, 6, 7, 68, 88
carbon, 9
catalyst, 12, 16, 23, 114
cell surface, 111
chalcogenides, 13, 26
challenges, 1, 24
chemical, vii, 12, 20, 23, 73, 86, 87, 97, 98, 105, 108, 109, 113, 115
chemical deposition, 98
chemical properties, vii
chemical reactions, 105
chromium, 106
cleavage, 24, 101, 110, 113
clusters, 88, 89, 90, 92, 97, 98, 109, 122, 123, 124, 126, 127, 131
commercial, 97, 107, 127
compatibility, 107
composition, 12, 20, 24, 26, 28, 30, 66, 69, 72, 78, 87, 90, 92, 113
compounds, 1, 3, 4, 5, 23, 37, 40, 57, 85, 92, 108
computational modeling, 92
computer, 51, 85, 100, 111
condensation, 3, 4, 6, 8, 15, 16, 19, 24, 25, 28, 31
conductance, 49, 60, 126

conduction, 36, 38, 40, 42, 43, 47, 55, 65, 123
conductivity, 4, 5, 45, 73, 76, 98, 125
configuration, 87
confinement, 56
constituents, 43
construction, 33, 38, 99
copper, 24, 97, 98, 100, 106, 107, 108, 109, 110, 111, 113, 114, 115, 116, 117, 119, 122, 123, 124, 126, 127
correlation, 20, 47, 65
cost, 12, 97
covering, 115, 127
crystal structure, 28, 31, 102, 110, 126
crystalline, 102, 103, 105
crystallites, 9, 19
crystals, 3, 4, 7, 84
CSD, 7, 14, 20, 21
cyanide, 108

D

decay, 39
defects, vii, 1, 3, 4, 5, 6, 7, 8, 11, 76, 90
deficiency, 87
deformation, 44, 124, 126, 127
deposition, 3, 4, 10, 12, 24, 84, 92, 98, 100, 106, 107, 108, 109, 110, 111, 112, 113, 114, 116, 118, 119, 123
deposition rate, 108, 111, 116
depth, 79, 113
detection, 4, 5, 113
detection system, 4, 5
dielectric constant, 47, 53, 61, 64, 68, 75, 79, 80, 82
diffraction, 13, 14, 17, 20, 23, 25, 102, 103
diffusion, 35, 61, 70, 82, 83, 88, 91, 93, 106, 113
diffusion process, 88
diodes, 1, 12
dipoles, 94
discontinuity, 35, 36, 47, 49, 55, 60, 65, 72
dislocation, 7, 9, 11
disorder, 125
dispersion, 118
dissociation, 24
distribution, 25, 28, 30, 48, 64, 69, 70, 83, 113
donors, 7, 56
dopants, 38
doping, 25, 27, 38, 56, 105
drawing, 23
drying, 99

E

effusion, 51
Egypt, 107
electric current, 123
electric field, 42, 49, 53, 70, 88, 123
electrical fields, 83
electrical properties, 44, 57, 97
electrical resistance, 98
electricity, 127
electrochemistry, 97
electroluminescence, 53
electromagnetic, 115
electron(s), 5, 11, 20, 26, 36, 37, 38, 40, 41, 42, 43, 44, 45, 47, 48, 49, 50, 53, 54, 55, 57, 60, 62, 63, 65, 68, 73, 74, 93, 94, 101, 104, 105, 109, 113, 115, 124, 126
electron diffraction, 57
electron microscopy, 20, 26
electron state, 38, 42, 45, 48, 49, 53, 60, 62, 63, 73
emission, 5, 7, 9, 11, 53, 54, 56
energy parameters, 47, 51, 54
epitaxial films, 88
epitaxial growth, 40
equilibrium, 34, 54, 55, 56
etching, 115
evacuation, 23
evaporation, 12, 24, 26, 86, 87
examinations, 33, 39, 45, 51, 66
excitation, 4, 5, 54, 56

exciton, 7, 9

F

fabrication, 38, 40, 51, 92, 97, 115, 127
Fermi level, 35, 43, 55
film thickness, 41, 57, 85
films, vii, 1, 3, 4, 5, 6, 7, 9, 10, 12, 14, 15, 17, 20, 22, 23, 24, 25, 26, 27, 28, 29, 30, 31, 33, 38, 40, 41, 44, 51, 56, 57, 63, 64, 69, 73, 86, 87, 88, 92, 93, 95, 129
fluctuations, 70, 72
force, 104
formation, 15, 21, 24, 31, 37, 54, 56, 69, 94, 115, 126

G

geometrical parameters, 116
geometry, 99, 118
glycol, 106
grain size, 15, 24, 26, 31
grazing, 102
growth, 3, 4, 5, 7, 10, 16, 24, 26, 31, 40, 44, 51, 57, 59, 61, 70, 88, 92
growth mechanism, 16
growth pressure, 24
growth temperature, 10
growth time, 51

H

height, 50, 70, 72, 79, 82, 93, 101, 111, 112, 113, 114, 116, 117, 118, 119, 120, 124
helium, 4, 5
hexagonal lattice, 13, 19
history, 107
homogeneity, 51
horses, 107
hydrogen, 23
hydroxide, 106, 107

I

illumination, 93, 124
image(s), 14, 15, 24, 26, 47, 65, 88, 100, 101, 109, 110, 111, 113
impurities, 5, 6, 7, 9, 10, 11, 54
incidence, 21, 102
independent variable, 42
inhomogeneity, 90
integration, 70
interface, vii, 20, 35, 37, 40, 42, 44, 47, 48, 49, 50, 53, 54, 56, 61, 69, 70, 72, 83, 90, 91, 113
interference, 41, 57
inversion, 40
ionization, 8
ions, 107
iron, 107
irradiation, 30, 93, 96, 106
IR-spectra, 14, 22
IR-spectroscopy, 20
islands, 76
issues, 77

L

lasers, 12
lattice parameters, 16, 19, 23, 44, 78
lead, 33, 38, 40, 51, 54, 56, 57, 72, 88, 102, 103, 104, 105, 115, 116
leakage, 71, 90
lifetime, 35, 39, 56, 93, 106
light, 20, 53, 54, 93, 94, 96, 127
light transmission, 20
linear dependence, 59, 80
linear function, 63
liquid phase, 38, 91, 92
low temperatures, 38, 54, 106
luminescence, 4, 5, 56

M

magnitude, 126

majority, 35, 50, 73, 76, 83
manganese, 28, 30, 31
manufacturing, 51, 130
mass, 36, 40, 42, 47, 49, 50, 55, 64, 65, 70, 85, 113
mass spectrometry, 113
materials, vii, 1, 3, 4, 5, 8, 13, 16, 19, 37, 40, 44, 47, 51, 52, 53, 57, 64, 65, 72, 78, 84, 86, 92, 107, 108
materials science, 57
matter, 98
measurement(s), 3, 4, 5, 35, 38, 45, 50, 53, 54, 55, 59, 61, 62, 63, 67, 70, 72, 73, 76, 77, 78, 79, 90, 92, 93, 95, 96, 116, 117, 119, 121, 125
melts, 67
mercury, v, 33, 88
metals, 97, 98, 103, 106, 109, 124, 127
meter, 121
microscope, 41, 57, 77, 100, 101, 109, 111, 112, 122
microscopic investigations, 88
microscopy, 23, 41
models, 93
molecular beam, 33, 38
molecular beam epitaxy, 33, 38
monolayer, 94
morphology, 12, 24, 31, 78, 100, 109, 111
MOVPE, 24

N

nanodots, 16, 23
nanofibers, 23
nanoparticles, 97
nanorods, 23
nanostructures, i, iii, vii, 12, 14, 15, 16, 17, 19, 20, 21, 22, 23, 125, 129
nanowires, 14, 16, 17, 19, 20
NAS, 25
Nd, 55, 62, 84, 85, 92
neutral, 7, 9, 11
NH_2, 21
nonequilibrium, 55
numerical analysis, 53, 94

O

OH, 23
optical properties, 129
optimization, 1
optoelectronics, vii, 24, 76, 92
overlap, 125
oxidation, 23
oxygen, 10, 11, 21, 23, 94

P

parallel, 19
parasite, 98
pH, 106
phase diagram, 66
phase transitions, 37
photoconductivity, 39
photodetectors, 12
photoluminescence, 3, 4, 10, 51, 129
photonics, 88
photosensitivity, 93
photovoltaic devices, vii, 12, 97
physical characteristics, 73
physical properties, 73
physics, 37, 93
PL spectrum, 8, 9, 11
point defects, vii, 3, 4
polarity, 71
precipitation, 51
preparation, 12, 23, 57, 58, 59, 84, 87
probability, 75
probe, 25, 121
profilometer, 119
protective coating, 106
purity, 12, 16, 20, 23, 24

Q

quantization, 37

quantum well, 37, 53, 54, 55, 56
quartz, 85

R

radiation, 12, 24, 25, 54, 97
radius, 28
reactions, 107
reagents, 106
recombination, 5, 6, 7, 9, 10, 36, 40, 44, 49, 50, 54, 63, 76
recycling, 108
reflection high-energy electron diffraction, 40
reflectivity, 84
reflexes, 13, 14, 16, 17, 19, 20
reliability, 92
relief, 23, 41, 48, 49, 60, 76, 88, 89, 90, 92, 93
researchers, 23
resistance, 92, 98, 119
resolution, 4, 5, 12, 25
room temperature, 51, 57, 61, 63, 72, 78, 87, 91, 92, 96, 114, 121
Russia, 129, 130

S

salts, 106
saturation, 35, 49, 68, 70, 72, 88, 90
scanning electron microscopy, 12
scattering, 7, 14, 38
science, 23
seed, 15
selectivity, 98, 107
semiconductor(s), vii, 1, 3, 4, 5, 12, 24, 37, 38, 40, 42, 43, 44, 51, 57, 67, 72, 76, 92, 93, 96, 97, 104, 124, 126, 127
sensors, 12
shape, 14
showing, 17, 37
silicon, 97, 98, 99, 100, 101, 102, 103, 105, 106, 109, 113, 127
silver, 97, 98, 99, 100, 101, 102, 103, 106, 107, 109, 110, 111, 112, 113, 114, 115, 116, 122, 123, 124, 126, 127
simulation, 35, 48, 49, 51, 69, 72, 83, 94, 96
single crystals, 15, 19
SiO_2, 106
software, 25, 116
solar cells, vii, 1, 97, 98, 108, 109, 114, 115, 116, 119, 125, 127
solid phase, 107
solid solutions, 1, 66, 67, 72
solution, vii, 23, 28, 31, 44, 50, 56, 76, 91, 97, 98, 106, 107, 108, 109, 114, 126
spectroscopy, 7, 41, 87
stability, 57, 108
stabilization, 4, 5
state(s), 35, 37, 42, 44, 47, 50, 64, 65, 70, 77, 82, 83, 87, 94
storage, 57, 58, 59, 60, 61, 116
structural defects, 8, 10, 11
structure, 1, 3, 4, 5, 10, 12, 14, 17, 19, 20, 23, 26, 31, 40, 41, 43, 53, 54, 68, 72, 73, 75, 78, 81, 88, 90, 91, 98, 101, 102, 105
substitution, 9
subtraction, 14, 20
Sun, 97
superconductivity, 127
superlattice, 40, 86
surface area, 25, 28, 30
surface layer, 109
surface structure, 76, 109, 110
symmetry, 92, 102, 110

T

target, 84, 85, 88, 92
techniques, 41, 51, 84, 97
technology, vii, 16, 26, 36, 44, 51, 57, 67, 70, 73, 78, 84, 92, 96, 97, 98, 107, 130

tellurium, 87
TEM, 24
temperature, 3, 4, 5, 7, 8, 10, 12, 14, 19, 21, 23, 24, 26, 27, 28, 29, 30, 31, 33, 38, 39, 40, 44, 46, 48, 51, 57, 60, 61, 72, 73, 76, 92, 93, 106, 115, 127, 129
temperature dependence, 39
texture, 5, 13, 25, 26, 29, 31
thermal energy, 44
thermodynamic equilibrium, 5
thermodynamics, 131
thin films, vii, 1, 3, 4, 5, 7, 10, 23, 26, 84, 85, 86, 96
thinning, 111
transformation(s), 63, 97
transmission, 14, 20, 41
transmission electron microscopy, 41
transparency, 35, 50, 53, 60, 69, 70, 93, 124, 125
transport, 62, 68, 70, 73, 88, 90, 93
transport processes, 73
tungsten, 99, 121, 122
tunneling, 35, 45, 48, 49, 50, 51, 60, 63, 68, 69, 70, 72, 73, 75, 76, 88, 91, 93, 124, 125

U

Ukraine, 25
uniform, 115, 116

V

vacancies, 6
vacuum, 3, 4, 10, 12, 20, 23, 24, 26, 33, 38, 51, 84, 85, 129
valence, 23, 35, 47, 55, 60, 65, 72, 94
vector, 29
velocity, 35, 60, 68, 72, 75, 88

W

water, 114
wave number, 20, 22
wide band gap, 76

X

XPS, 87, 113
X-ray diffraction (XRD), 11, 13, 14, 16, 19, 23, 24, 25, 26, 28, 86, 87, 102, 103, 110, 111

Z

zinc, 5, 8, 12, 13, 33, 38, 54, 56, 57, 63, 104, 105
ZnO, 21, 97